UNIVERSITAT POLITÈCNICA DE CATALUNYA BARCELONATECH

Spectral phase control of nanoscale nonlinear optical responses

Vikas Remesh

Spectral phase control of nanoscale nonlinear optical responses

Doctoral Thesis

by

Vikas Remesh

Thesis advisor:

Prof. Niek F. van Hulst

ICFO- The Institute of Photonic Sciences

Barcelona Institute of Science and Technology

Universitat Politécnica de Catalunya

April 2020

Thesis advisor:
Prof. Dr. Niek F. van Hulst

Thesis committee:
Dr. Ir. Herman Offerhaus, University of Twente, The Netherlands,
Dr. Frank Güell, University of Barcelona, Spain.
Dr. Nicolas Bonod, Institut Fresnel, Marseille, France,

To my family and all my teachers.
for the life and the light.

"That is why he constantly strives to achieve true insight..And now comes the important part: it troubled him that he knew so little."

Jostein Garder, Sophie's World

Contents

Abstract

The study of light-driven physical processes generated in nanomaterials require shorter (in time, or broader in frequency) laser pulses with techniques to tailor its phase and temporal/spectral characteristics at the nanoscopic interaction volume. Such studies can specifically address the aspect of coherence of excited states in molecular systems or of collective electronic oscillations in plasmonic nanoresonators. Addressing nonlinear coherent phenomena with broadband femtosecond pulses, usually involve achieving constructive or destructive interferences between multiple absorption pathways by spectral phase manipulation.

Despite progress on in ultrafast spatiotemporal control of optical processes, a systematic, true optical coherent control on a fundamental dipole plasmon mode remained challenging due to the very short dephasing time of the plasmon oscillation in the 25 fs range. Unfortunately, luminescence is an incoherent process and therefore generally not explored for nanoscale coherent control of the antenna response. Firstly, we demonstrated that, in resonant gold nanoantennas, the two-photon absorption process can be coherent, provided that the excitation pulse duration is shorter than the dephasing time of plasmon mode oscillation. Exploiting this coherent response, we showed the pure spectral phase control of resonant gold nanoantennas, with effective read-out of the two-photon photoluminescence.

High-index dielectric nanoantennas, for example, gallium phosphide (GaP) nanoantennas have recently emerged as pro-mising alternatives to plasmonic nanoantennas displaying extremely low losses

in the visible range and having high nonlinearities. They also support both multipolar electric and magnetic resonances in both visible and NIR frequency range. Especially, the low losses and large nonlinearities are promising for ultrafast optical switching and truly all-optical control of GaP nanodevices. Here first we used two- and three-photon excitation of GaP nanodisks to probe the size-dependent resonance enhancement of second-harmonic and bandgap emission. Next, we showed, by spectral phase control of broadband pulsed excitation, that GaP nanoantennas outperformed their metal counterparts in supporting nonlinear optical coherences.

Next, our numerical studies on the SHG enhancement in GaP nanoantennas indicated that size-dependent SHG enhancement is the result of resonant electric field confinement in the nanoantenna volume. Study of angular emission pattern, combined with polarimetry of resonant nanoantennas revealed that SHG emission resulting from the excitation with linear polarization is predominantly radially polarized. The multipolar modal analysis at SHG frequency indicated the presence of an electric dipole oscillating along the disk axis, along with weak contributions of quadrupoles and octupoles.

Finally, size-dependent SHG spectral shift confirmed the existence of multiple resonances in these nanodisks. Exploiting this feature, multipolar electromagnetic modes that resonate with relative phases, following a broadband laser illumination, can be made to interfere and the interference can be controlled by means of spectral phase modulation of the excitation field to achieve directionality. With an antisymmetric π step modulation, a switching in polarization state was observed. Our experiments pave way for all-optical control of directional radiation of nanoantennas by the control of multipolar interference in the nonlinear regime.

Resumen

El estudio de los procesos físicos impulsados por la luz generados en nanomateriales requiere pulsos láser más cortos (en el tiempo) con técnicas para adaptar sus características de fase y temporales ó espectrales en el volumen de interacción nanoscópica. Dichos estudios pueden abordar específicamente el aspecto de la coherencia de estados excitados en sistemas moleculares o de oscilaciones electrónicas colectivas en nanoresonadores plasmónicos. Abordar fenómenos coherentes no lineales con pulsos de femtosegundos de banda ancha, generalmente implica lograr interferencias constructivas o destructivas entre múltiples vías de absorción mediante manipulación de fase espectral.

A pesar del progreso en el control espacio-temporal ultrarrápido de los procesos ópticos, un control coherente óptico sistemático y verdadero en un modo de plasmón dipolar fundamental seguía siendo desafiante debido al muy corto tiempo de decoherencia de la oscilación del plasmón en el rango de 25 fs. Desafortunadamente, la luminiscencia es un proceso incoherente y, por lo tanto, generalmente no hacido explorado todavia para el control coherente a nanoescala de la respuesta de la antena. En primer lugar, demostramos que, en las nanoantenas de oro resonantes, el proceso de absorción de dos fotones puede ser coherente, siempre que la duración del pulso de excitación sea más corta que el tiempo de desfase de la oscilación del modo plasmonico. Aprovechando esta respuesta coherente, mostramos el control de la fase espectral pura de nanoantenas de oro resonantes, concolectando eficientemente de la fotoluminiscencia de dos fotones.

Las nanoantenas dieléctricas de alto índice de refracción, por ejemplo, las nanoantenas de fosfuro de galio (GaP), han surgido recientemente como alternativas prometedoras a las nanoantenas plasmónicas que muestran scattering muy bajas extremadamente bajas en el rango visible y tienen altas no linealidades. También admiten resonancias magnéticas y eléctricas multipolares en el rango de frecuencia visible y NIR. Especialmente, las bajas scattering y las grandes no linealidades son prometedoras para una conmutación óptica ultrarrápida y un control puramente todo óptico de los nanodispositivos GaP. Aquí, primero, utilizamos la excitación de dos y tres fotones de los nanodiscos de GaP para probar la mejora de resonancia dependiente del tamaño de los nanodiscos de la emisión de segundo armónico y de la banda prohibida. A continuación, demostramos, mediante el control de fase espectral de la excitación pulsada de banda ancha, que las nanoantenas de GaP superaron a sus contrapartes metálicas en el generación de coherencias ópticas no lineales.

A continuación, nuestros estudios numéricos sobre la mejora de SHG en las nanoantenas GaP indicaron que la mejora de SHG dependiente del tamaño es el resultado del confinamiento de campo eléctrico resonante en el volumen de nanoantena. El estudio del modelo de emisión angular, combinado con la polarimetría de nanoantenas resonantes reveló que la emisión de SHG resultante de la excitación con polarización lineal está predominantemente polarizada radialmente. El análisis modal multipolar a frecuencia SHG indicó la presencia de un dipolo eléctrico que oscila a lo largo del eje del disco, junto con contribuciones débiles de cuadrupolos y octopolos.

Finalmente, el cambio espectral de SHG dependiente del tamaño confirmó la existencia de resonancias múltiples en estos nanodiscos. Aprovec-hando esta característica, los modos electromagnéticos multipolares que resuenan con fases relativas, después de una iluminación láser de banda ancha, pueden interferir y la interferencia puede controlarse mediante la modulación de fase espectral del campo de excitación para lograr la direccionalidad. Con una modulación de paso

pi antisimétrica, se observó un cambio en el estado de polarización. Nuestros experimentos abren el camino para el control totalmente óptico de la radiación direccional de nanoantenas mediante el control de la interferencia multipolar en el régimen no lineal.

1 Prologue

Light, as the visible part (wavelength range from approximately 400 to 700 nanometers) of electromagnetic radiation available for direct human perception, for the same reason has always been a part of human life. Tracing the history of classical optics, it was Democritus who attempted to explain the perception and colour [1], first. Since then, our understanding on the properties of light has grown enormously over several centuries, that goes hand-in-hand with the evolution of Physics over the centuries: the corpuscular theory of Newton, wave optics formalism of Huygens, Maxwell's theory on electromagnetism, Planck's quantum theory of blackbody radiation and so on [2, 3]. It took only four decades since the proposal of Einstein in 1917 [4] on the stimulated emission of light, for the development of the first laser source, marking the beginning of the era of photonics. Ever since, lasers have reached to almost everything we know in our life today: smartphones, televisions, communications, healthcare, food industry, textile industry, space technology, energy industry etc.

Nanophotonics is the study of interaction of light with matter at

the nanoscale [5–8]. In the recent years, it has been drawing attention from the scientific and industrial communities and has found many applications in sensing, biomedical diagnostics, labels for biomedical imaging, household telecommunication devices, high efficiency solar cells, data storage, personalized healthcare technologies etc. The basic underlying principle to induce light-matter interaction at the nanoscale is to confine light to nanoscale dimensions, i.e., to the size much smaller than optical wavelengths.

Considering the analogue to radio wave antennas, a nanoparticle that is capable of interacting with optical wavelengths, can be called an optical antenna. In an excellent review work, Novotny and coworkers define an optical antenna this way: *a device designed to efficiently convert free-propagating optical radiation to localized energy and vice versa* [9]. They are nanometric in size, due to the fact that optical wavelengths are at least 6 to 8 orders smaller than radio wavelengths. Thus, optical antennas, hereafter referred to as *nanoantennas*, are capable of propagating, receiving and transmitting electromagnetic fields at the nanoscale. Fabricating materials at the nanometric scale with reproducible qualities is challenging. Fortunately, the technical advancement in nanofabrication and characterization in the past decade has allowed the nanofabrication of extremely complicated structures. The research on nanoantennas began with metallic systems which recently migrated to dielectric and 2D materials.

In metallic nanoantennas, most of the optical properties originate from collective electron oscillations induced in the particle following optical excitation, called localized plasmon resonances [10, 11]. These plasmon resonances help concentrating the electromagnetic field in a very small volume in its near field (size << wavelength), creating a nanoscopic platform to study many light induced linear and nonlinear processes, thus acting as an efficient reporter of its surroundings. A nanoemitter placed in the near field of a plasmonic nanoantenna benefits from the tight confinement of electromagnetic field and helps increasing the radiation power of the emitter by a few

orders of magnitude. Plasmonics, thus paves way for the generation, detection, control, and use of plasmons for information and energy carrying at the nanoscale. This resulted in several research works that demonstrated huge enhancement in radiative properties of weak emitters like single molecules and quantum dots [12–20], enhancement in nonlinear processes, including second harmonic generation (SHG) and third harmonic generation (THG) etc. [21–27]. However, while metals act like ideal conductor at lower frequencies, they suffer from ohmic losses at higher and optical frequencies, thus degrading the performance of nanoscale resonators. Plasmons are damped by elastic and inelastic scattering of electrons on other electrons, or phonons, or even on lattice defects. This damping severely reduces the performance of a metallic nanoantenna resonator [28].

In dielectric nanoantennas, on the other hand, moving charges are absent and therefore plasmon resonances do not exist. Recently, it has been demonstrated that strong Mie resonances can be induced in such materials when electromagnetic excitation induces a shift in charge distribution, generating a polarization current. In contrast to plasmonic nanoantennas, dielectric nanoantennas support both electric and magnetic resonances, which result in many more interesting applications.

Thus, it is clear that the study of light-matter interactions in nanostructures poses significant challenges. Nanoantennas are typically low quality (Q) factor resonators (on the order of $Q \approx 10$). This implies that their temporal responses are limited to femtosecond time scale. Therefore, to characterize interactions of a nanoantenna with light, the investigation technique should ideally possess both nanometer-scale spatial resolution and ultrafast temporal resolution. To this end, significant progress has been made: methods like time-resolved ultrafast spectroscopy, near field optical microscopy, cathodoluminescence and electron energy loss spectroscopy, photoemission spectroscopy are few of the major techniques in this direction.

Firstly, advances in laser technology allowed the development of ultrafast lasers, with timewidth of femtoseconds and shorter, in the

last decades of the past century. Femtosecond pulses are now broadening their reach in different applications ranging from medical sciences to industry. Technically, such lasers became possible since the advent of mode-locking technology [29, 30]. In a mode-locked laser, the cavity modes oscillate with a definite phase, which interfere destructively except when they are all in-phase. This results in a train of short pulses with a very short temporal width. Major features of these lasers include high peak intensity (typically 10^5 times higher than that of the same average continuous wave laser power), and broad optical spectrum resulting in extremely short temporal width (on the order of a few fs). Technical advancement in the femtosecond laser technology helped replacing liquid gain media with solid-state Ti:sapphire crystals to Yb:doped crystals and fibres, increasing the average power and stability. Furthermore, second- and third-order nonlinear optical effects were exploited to broaden the spectrum further and tune the frequencies, enabling to cover frequency ranges from mid infrared to ultraviolet. These properties make fs pulses an ideal choice for many applications such as observing photoinduced processes in bio-molecules, studying carrier dynamics in the operation of opto-electronic devices, imaging live tissues by limiting the potential damage [31, 32] and industrial applications like laser ablation, micromachining, waveguide writing and so on [33]. The development of fs laser sources with devices capable of tailoring their properties, opened up new doors in nanophotonics research. One of the most notable application, particularly in the context of this thesis, is the possibility of studying chemical dynamics of molecular systems on the timescales otherwise impossible to access [34–36] and for probing the optical nonlinearities of nanoantennas [37–39].

Secondly, in order to focus the interaction down to the nanoscale and single-photoemitter level, high numerical aperture, low-background micros-copy technique is required. Confocal microscopy, along with high sensitive avalanche photodiodes (APD), electron-multiplying charge coupled device camera (emCCD) and high resolution spectrometer [40–44] enables diffraction limited, low background detection and

spectroscopy of weak emitters like single molecules and quantum dots [45–48].

Coherence is one of the most important feature of a light-induced physical process. Coherent states with long lifetime is of fundamental importance in many physical processes like photosynthesis energy transfer, quantum computation, observation of electron dynamics [49, 50, 50–52] etc. The study of excited-state coherence allows for the fundamental understanding on Rabi oscillations, generation of indistinguishable single photons and entangled photon pairs [53–55]. Since the electronic excited state coherence is of the order of few tens of fs, it becomes immediately obvious that broadband, fs lasers are the only light sources that allow to probe the coherence of a quantum state, which recently was demonstrated down to single quantum dots and molecules [56, 57]. Needless to say, fs lasers have broad frequency spectrum, which opens up the possibility of tuning the amplitude and phase of individual frequency components to helps to perform various spectroscopic studies addressing the quantum coherence, in general termed *coherent control*. Following the seminal proposals from Shapiro, Brumer, Rabitz, Tannor and Rice [58–61], based on the idea of steering a quantum system from a given initial state to a target state via an external field, *phase-shaped pulses* were used to achieve results ranging from the controlling reaction pathways and influencing the amount of photodissociation products in molecular systems [62, 63], laser cooling of internal degrees of freedom of atomic systems [64], bioimaging [32] and energy flow in light harvesting systems [51, 65, 66].

1.1 Scope of this thesis

It is clear so far, that the coherent control of light-matter interactions at the nanoscale requires ultrafast temporal resolution and nanometric spatial resolution. Confronting this reality offers new directions in

the nanophotonics research, two of which turns out to be the specific focus of original research described in this thesis work:

- To push the temporal limit of ultrafast single-emitter nonlinear spectroscopy, to be able to coherently address the nonlinear optical response of nanoantennas, paving way for a true all-optical nanoscale light control.
- To control the vectorial angular second harmonic emission of a nanoantenna by manipulating the properties of interacting light.

To this end, original research was carried out by the author in the research group, the results of which form the basis of this thesis. The outline of the thesis is as follows:

Chapter 2 firstly introduces the basics of femtosecond laser pulses and the techniques to characterize and control their properties, to provide the reader with the background to understand the requirements of nanoscale coherent control experiments.It is then followed by a description of nano material systems that are of our interest in studying linear and nonlinear optical interactions that occur in the time and intensity scales accessible only by our laser system.

Chapter 3 describes a truly all-optical coherent control experiment, to coherently manipulate the localized surface plasmon oscillations in a resonant gold nanoantenna by probing its two-photon luminescence emission. This provides the capabilities of the optical setup that can address photophysical processes that are as fast as 30 fs and lower.

Chapter 4 extends this study to the size-dependent multiphoton resonances in a lossless dielectric nanoantenna, specifically in gallium phosphide nanodisks, and explores the differences in nonlinear optical coherences compared to that of metallic nanoantennas.

Chapter 5 investigates the origins of enhanced second harmonic generation in gallium phosphide nanodisks and studies its polarization-resolved radiation pattern. We observe the nonlinear generation of

radially polarized vector beams in the nanoantenna at second harmonic wavelengths with circular polarization components. Results of numerical methods to understand the observations based on multipolar decomposition will be described.

Chapter 6 combines the idea of coherent control with vectorial angular emission and show a proof-of-principle experiment, which aims to control the multipolar spectral interferences in a gallium phosphide nanodisk, thereby manipulating the properties of its radiation pattern.

Lastly, the thesis is summarised by listing the main findings and a future perspective to experimental research that these conclusions can be based up on.

2

Ultrafast nanophotonics

Controlling light at the nanoscale is a vibrant research field of recent years. The progress in ultrafast measurement techniques have improved our knowledge on the fundamental processes following the light-matter interaction. In this chapter, firstly, the fundamentals of femtosecond lasers, pulse characterization and techniques to tailor the properties of the laser pulses are discussed. Based on this knowledge, the experimental set up that is employed in practice for most of the experiments in this thesis will be described, followed by the exemplary results on the the spectral phase-amplitude control of linear and the nonlinear interactions of single photoemitters with femtosecond pulses. Finally, we conclude the chapter by describing the Stokes polarization formalism that supplements the investigation of nonlinear properties of nanoantennas in later Chapters.

2.1 Femtosecond laser pulses and their features

Mathematically, an ultrafast laser pulse is quite straightforward to define: for a given central frequency (ω_0) and for a given complex envelope ($A(t)$), we can define an optical pulse in time domain, with a given temporal phase ($\phi(t)$) as [67–70]:

$$E(t) = A(t)e^{i(\omega_0 t+\phi(t))}. \tag{2.1}$$

The Fourier transformation of Eq. (2.1) yields the spectral domain representation of this laser pulse:

$$E(\omega) = A(\omega)e^{i\phi(\omega)} \tag{2.2}$$

where $A(\omega)$ is the amplitude of the spectral components of the laser and $\phi(\omega)$ is called the spectral phase. Assuming a Gaussian spectral envelope, Eq. (2.2) can be rewritten as,

$$E(\omega) = e^{(\frac{\omega-\omega_0}{\Delta\omega})^2}e^{i\phi(\omega)}. \tag{2.3}$$

Fig. 2.1 summarises the time and frequency domain representations of a fs laser pulse. Starting from a temporal profile of 15 fs duration, we obtain the frequency domain representation by Fourier transformation. The spectral phase is then obtained as the angular part of the Fourier transform. The shortest duration of a laser pulse with a given spectral width is called the Fourier-limit or the transform-limit (τ): if $\Delta\omega$ is the bandwidth of a laser pulse, then, what follows from the uncertainty principle is that, $\Delta\omega \times \tau \geq 2\pi$. This implies that a laser with a large bandwidth will have to be extremely short in time domain.

From the experimental point of view, measurable quantities of a femtosecond laser pulse are its spectral intensity $|A(\omega)|$, spectral phase $\phi(\omega)$ and the average power. $|A(\omega)|$ is measured with a spectrometer and $\phi(\omega)$ is extracted with a procedure described later in

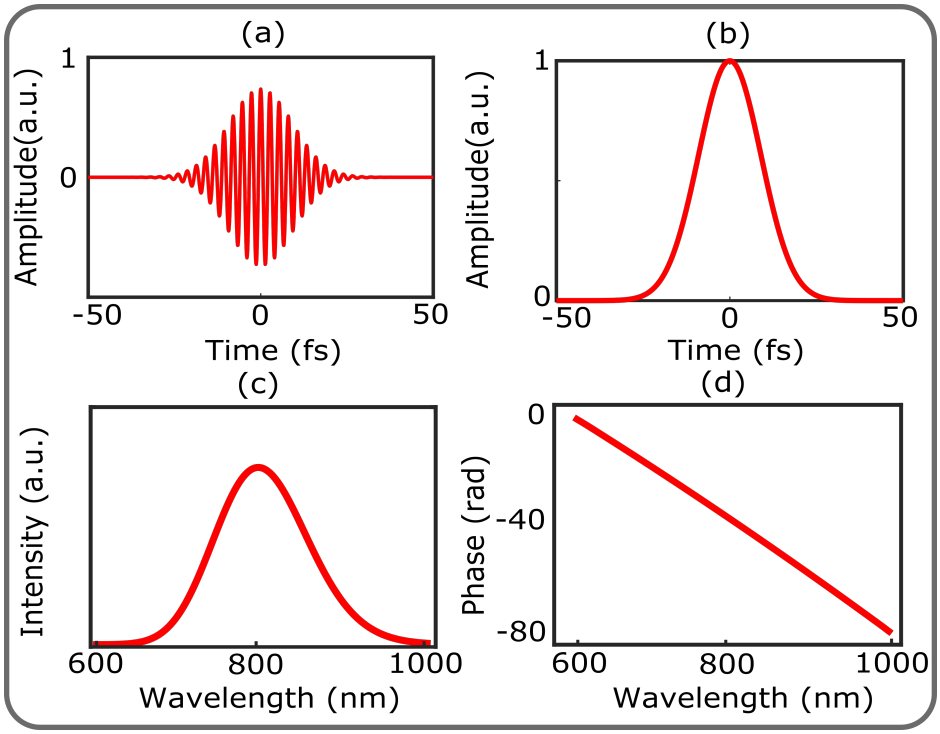

Figure 2.1: **Characteristics of a 15 fs Gaussian laser pulse**. (a) Electric field representation (b) Gaussian temporal envelope, (c) Fourier transform of the time domain representation yields the spectral domain representation, here converted to wavelength scale (d) Spectral phase of this laser pulse.

the section 2.2.1. Average power is usually measured with a power meter.

Mathematically, $\phi(\omega)$ can be defined as a Taylor expansion of many contributions:

$$\phi(\omega) = \phi_0 + \phi_1 \frac{(\omega - \omega_0)}{1!} + \phi_2 \frac{(\omega - \omega_0)^2}{2!} + ... \tag{2.4}$$

The first term in Eq. (2.4), ϕ_0 is called the absolute phase or the carrier envelope phase and defines the phase between the carrier wave of frequency ω_0 and the position of the intensity envelope $|A(\omega)|$. Note that ϕ_0 is equivalent in both time and frequency domain and

becomes relevant only to pulses of single cycle long. Hence, it is insignificant for the experiments described in this thesis. The second term ϕ_1 describes the group delay, which in time domain, defines the delay t between a given ω and ω_0, or time-shifts the pulse envelope from an arbitrary zero-point. The group delay t is defined as $t = -\frac{d\phi}{d\omega}$.

The most important term concerning a major portion of this thesis is the third term ϕ_2, called the group delay dispersion (GDD), or in general, *linear chirp*. Unlike the ϕ_0 and ϕ_1, a change in ϕ_2 will result in a change in pulse duration τ. The *linear chirp* manipulates the laser frequency as a linear function of time with its sign governing the ordering of the frequency components. Similar to the way the group delay was defined before, GDD can be defined as,

$$\phi_2 = -\frac{d^2\phi}{d\omega^2}. \tag{2.5}$$

A positive value of ϕ_2 implies that in the time domain, the frequency increases with time, meaning the *blue* (high frequency) components of the spectrum comes after the *red* (low frequency) components. A negative value of GDD implies vice versa. Also, changing the magnitude of GDD, changes the temporal width of the pulse and from the Fourier relations, for a transform limited laser pulse length τ, with a Gaussian spectral profile, for a given ϕ_2, the resulting pulse duration τ_o can be described as [71],

$$\tau_o^2 = \tau^2 + \left(\frac{4\ln(2)(\phi_2)^2}{\tau}\right)^2. \tag{2.6}$$

Throughout this thesis, we will describe various experiments in which $|A(\omega)|$ and $\phi(\omega)$ are systematically manipulated to address specific physical processes following the interaction of fs pulses with single photoemitters. We also acknowledge that there exists blind optimization experiments which employ what is called a *genetic algorithm* without *a priori* knowing the required spectral phase or amplitude, and instead derives it via a feedback system. In this thesis

work we chose the deterministic approach and recommend the reader to approach [72–74] for more information. In the following section, we will describe our experimental methods for achieving coherent control of nanoscale light-matter interactions.

2.2 Experimental setup

The setup for most of the experiments described in this thesis consists of the following main elements: (a) a broadband Titanium Sapphire laser, (b) a 4f shaper, (c) a confocal microscope with a sensitive photo detector and a spectrometer.

The broadband Ti: Sapphire laser produces 10 fs pulses with a repetition rate of 85 MHz at a central wavelength of 790 nm (Octavius, Menlo Systems/ Thorlabs). It is worth mentioning that the peak power of a fs laser pulse is defined in terms of the pulse energy E_p and τ and as: $P_p = 0.94\frac{E_p}{\tau}$, assuming a Gaussian profile [75, 76]. The pulse energy is simply the ratio of average power P_{avg} and the repetition rate of the laser f_{rep}. In our case, P_{avg} = 300 mW, f_{rep} = 85 MHz, τ = 15 fs, which gives us 3.5 nJ energy per pulse and the peak pulse power of 0.23 MW. The collimated laser beam is directed to the home-built 4f shaper in reflection geometry equipped with a programmable spatial light modulator (SLM, from CRi, 640 pixels, dual mask) adapted from the MIIPS Box (from Biophotonic Solutions Inc.).

In the 4f shaper, the laser beam first is spread over a grating (600 lines/mm) and then disperses, and is focussed on the spatial light modulator (CRi, 640 pixels, dual mask,) setup at the Fourier plane of a gold coated curved mirror of f=76 cm. The laser beam entering the shaper travels a distance that amounts to 4 times the focal length of the focussing element, a condition that is required to maintain the pulses dispersion free (hence the name *4f shaper*). Each narrow spectral region of the dispersed laser beam gets assigned to a single pixel in the SLM, which is made of transparent nematic liquid

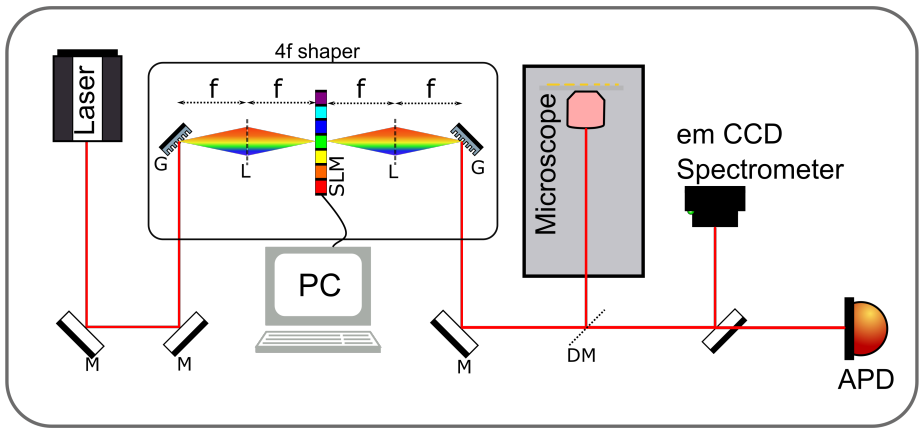

Figure 2.2: **The experimental setup**. 15 fs pulses from a broadband Ti: Sapphire laser enters a 4f shaper through a mirror, gets dispersed by a grating and gets focussed on to the pixels of the SLM by a focussing element with f focal length. The outgoing pulses are then directed onto the focus of a high NA objective in a confocal microscope. For signal collection, we employ single-photon counting APD or emCCD/spectrometer. M- mirror, DM- dichroic mirror, L-lens, G-grating.

crystals which provide an electrically variable refractive index for a given laser wavelength, that is polarised along the the extraordinary axis of the crystal. By applying individual voltage settings to the pixels, one can independently manipulate the properties of the narrow spectral range (depending on the range allowed for a given SLM). The relationship between voltage applied and the resultant phase is determined beforehand by a very careful calibration method, described in detail in Monmayrant et. al. [77]. The dual mask arrangement combines two liquid crystal cells arranged orthogonal to each other in a way that is 45° to the incoming polarisation of the laser. This feature allows to independently control phase and amplitude of the laser pulses. The amplitude modulation that can be achieved is defined as the cosine of differential retardance of the two liquid crystal cells. Assuming E_{in} to be the amplitude of the incoming electric field to the shaper, the amplitude of the output electric field E_{out} leaving

the shaper is defined as [70, 77]:

$$E_{out} = E_{in}.\cos(\frac{\Phi_A - \Phi_B}{2})e^{i\frac{(\Phi_A+\Phi_B)}{2}} \tag{2.7}$$

which clearly shows the modified amplitude along with its phase. The shaped laser beam fills the back aperture of a high numerical aperture oil-objective (NA = 1.46) through an inverted confocal microscope (Zeiss Axiovert 200) enabling us to sharply focus on single nanoscopic photoemitters and to collect their optical response. For signal collection, we use single-photon sensitive avalanche photodiode (MPD/ Perkin Elmer) and a spectrometer equipped with an electron multiplying charge coupled device (emCCD) camera (Andor).

A broadband laser pulse that passes through a high index medium experiences a chromatic dispersion depending on the wavelength. This is due to the wavelength- dependent index of refraction of the dispersive material. This is called the group velocity dispersion and results in the variation in temporal profile of the laser pulse while the spectrum remains unchanged. A normal dispersive material like silica glass will introduce the dispersion in a way such that blue part of the pulse travels slower than the red part, which we call positive chirp, and the opposite is called negative or anomalous dispersion, where blue part travels faster than the red part. Whatever the aim it may be, it becomes important for an experiment that wishes to control spectral phase and temporal width of the pulses, to characterize the dispersion of the excitation pulses at the sample volume.

2.2.1 Pulse compression

It is clear from the discussion above that it is important to determine *a priori* the $\phi(\omega)$ of the laser pulse. Compressing the pulse in time domain to its Fourier limit is the primary requirement before any measurement involving a given spectral phase profile. There are various methods of pulse characterization and compression employed by different groups: (a) prism compression, where a pair of prisms

compensate for the phase distortion depending on the distances and angles between them, (b) frequency resolved optical gating (FROG), a pulse pair made to interfere with each other, generating a FROG trace which is then used to retrieve electric field and the phase [78, 79], (c) spectral phase interferometry for direct electric field reconstruction (SPIDER), which uses a trio of pulses, one of which is chirped and all three are made to interfere for generating sum frequency generation [80], (d) grating eliminated no nonsense observation of ultrafast incident laser light electric fields (GRENOUILLE), a simplified technique derived to reduce the complexity of FROG [81], (e) crossed beam spectral interferometry, also called SEA-TADPOLE, which is a linear and sensitive technique simplifying the alignment problems in FROG and GRENOUILLE [82] and (f) multiphoton intrapulse interference phase scan (MIIPS), the technique that we use for experiments described in this thesis [83–85].

The versatility of MIIPS is that 4f shaper-assisted characterization and compensation happens in a single step. The techniques (a) to (e) involve characterizing the pulse followed by compensating for the distortion, which makes the procedure lengthy and cumbersome. On the other hand, MIIPS is able to determine $\phi(\omega)$ of the pulse and compensate for the distortion by adding -$\phi(\omega)$ in a matter of few minutes, through an automatic iterative algorithm. It works directly in the spectral domain and considers the fact that second harmonic generation (SHG), or in general, any multiphoton process, involves the simultaneous summing of multiple frequencies to generate a new frequency. The phase between multiple frequencies generate a particular SHG depending on the constructive or destructive interference in the absorption pathways. As the GDD is correlated with the SHG intensity, at any given frequency, SHG is maximized if the GDD is minimum. Later in section of this Chapter and in Chapters 3 and 4 we make use of this principle to demonstrate the spectral phase control of SHG response. This means that, a pulse can be made transform limited, by applying suitable phase masks and maximizing SHG for the whole spectrum.

The standard implementation of MIIPS works like this: Consider the spectral phase of the laser pulse to be $\phi(\omega)$. With the shaper, we introduce a sinusoidal reference phase $f(\omega) = \alpha \cos(\gamma(\omega - \omega_0) - \delta)$, where α describes the amplitude of the phase modulation, γ denotes its frequency, and δ describes the offset phase with respect to the central frequency ω_0 on top of $\phi(\omega)$ (shown in Fig. 2.3 (a)). In time domain, this is a pulse train where the pulses are separated by γ fs. During the MIIPS routine, the δ is ran from 0 to 2π and for every value of δ, corresponding SHG spectrum is measured. Subsequently, the δ that maximises the SHG spectrum is found. It is clear that SHG is maximized when the second derivative of the total phase $\phi(\omega) + f(\omega) = 0$. This implies that $\phi''(\omega) = -f''(\omega)$, which means $\phi''(\omega) = \alpha\gamma^2 \cos(\gamma(\omega - \omega_0) - \delta)$. The original $\phi(\omega)$ is then easily obtained. It is then trivial to add $-\phi(\omega)$ to the spectral profile to compensate for the distortions.

A complete MIIPS iteration results in a spectrogram of SHG spectral intensity with respect to δ, shown in Fig. 2.3 (b):

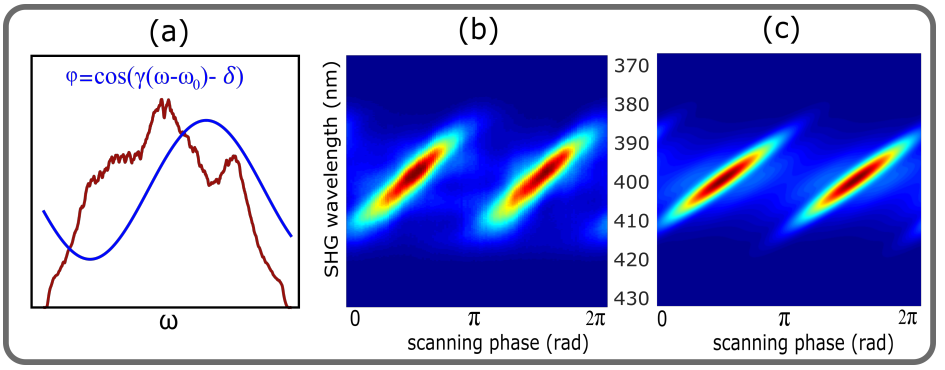

Figure 2.3: **MIIPS spectrogram**. (a) The phase modulation used in MIIPS algorithm. A sinusoidal phase with an offset δ is added on the laser spectrum. Corresponding SHG spectrum is measured for every δ value. (b) The SHG spectrogram obtained after a full MIIPS iteration shows two lines where SHG is maximum, separated in phase offset of π radians, (c) The simulated spectrogram for a 15 fs pulse matches the experimental result.

It is easy to appreciate the pulse characteristics from a MIIPS spectrogram. The lines of maximum intensity in the spectrogram lie π radians apart and are perfectly parallel to each other in the best case. A non-π separation indicates uncorrected second-order distortion and a tilt of the line shows third-order distortion of the pulse. In Fig. 2.3 (c) we show a simulated MIIPS spectrogram based on our experimental parameters, which nicely correlates with the measured one.

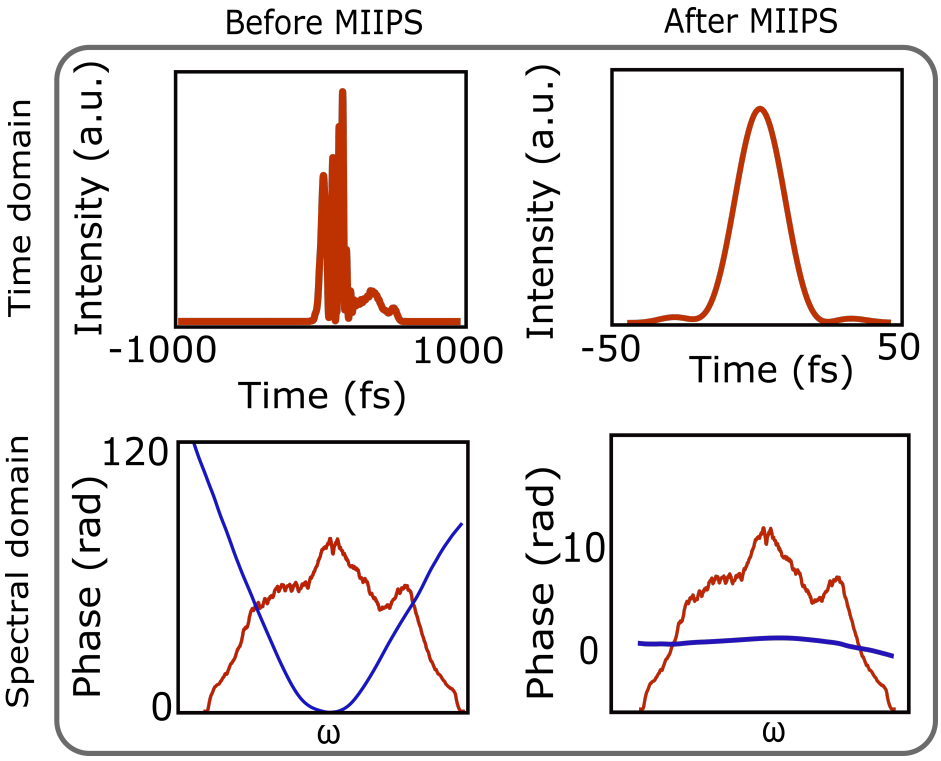

Figure 2.4: **Summary of MIIPS**. (a) Temporal profile of the laser pulse before the MIIPS compression shows the chirped pulse profile (b) After MIIPS, the pulse becomes transform limited and attains a Gaussian profile with FWHM = 15 fs. (c) The spectral profile before MIIPS with the spectral phase showing the second order phase distortion (d) The spectral profile after MIIPS has the same shape, however, the spectral phase flattens to zero radians across the whole spectrum.

Recently, an improvised version of the MIIPS technique was proposed, called the gated MIIPS. The procedure involves an amplitude gate scanned across the laser spectrum that helps estimate the spectral phase more accurately and correct for the higher order phase distortions and shaper artifacts [86]. We do not consider the technique as it strictly only applies for pulses as short as 10 fs.

The Fig. 2.4 we show a summary of the nature of the laser pulse before and after a MIIPS iteration both in temporal and spectral domain. Starting from a chirped laser pulse, which has a quadratic spectral phase due to second order phase distortions, we perform MIIPS iteration to eventually achieve a transform limited Gaussian pulse in time domain, which in frequency domain has a flat, zero phase for the whole frequency range.

To demonstrate that the pulse compression down to the Fourier limit results in accurate characterization of our excitation pulses, we perform a FROG scan detecting SHG and compare the result with the simulation. This makes sure that the excitation pulses are free of phase distortions at the sample volume. It is a critical requirement to have critical phase stability at the focus of a microscope objective to be able to make experiments on single molecules and nanoantennas, free of artifacts.

It is clear that the experimental FROG trace correlates well with the simulated one. Thus, our MIIPS pulse compression scheme followed by the FROG characterization ensures that the laser pulse is Fourier limited at the excitation volume. This provides the right scenario for implementing arbitrary phase-shaping of laser pulses to investigate specific light-matter interactions.

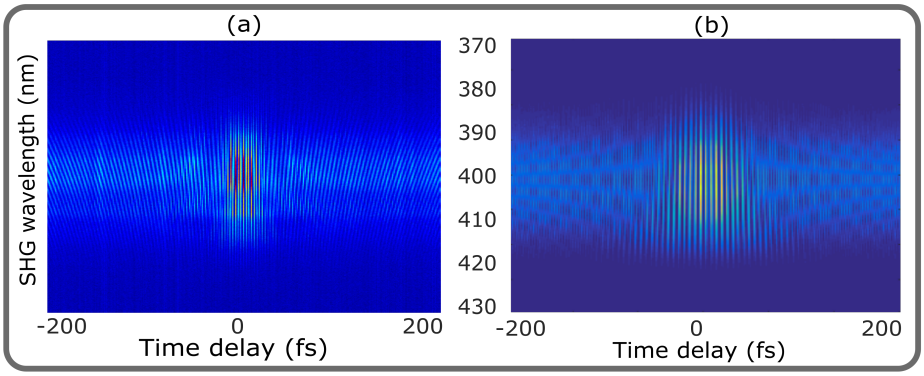

Figure 2.5: **Pulse characteristics at the excitation volume**. (a) The FROG spectrogram of 15 fs pulses after MIIPS compression (b) The simulated FROG spectrogram of a 15 fs pulse matches well with the observed one.

2.3 Nanomaterials

For the experiments described in this thesis we mainly studied the interaction of fs laser pulses with nanomaterials of three different types: metal nanoantennas, dielectric nanoantennas and single molecules. Nanoantennas are subwavelength structures made of metals (in our case gold (Au)) or high-index dielectric materials (gallium phosphide-GaP). In general, these structures are made by electron-beam lithography followed by lift-off or etching procedures. For single molecule experiments, a solution of specific concentration is prepared and spin-coated on to the microscope coverslip.

Metal nanoantennas generate coherent electronic oscillations on interaction with light, called localized surface plasmons, which, depending on the dimensions of the structure, resonate in a particular frequency. These plasmon resonances are accompanied by strong absorption, scattering and local field enhancements, which gave birth to the field of plasmonics with numerous applications [87]. These resonances are size dependent, due to the fact that the dielectric constant ϵ of a material depends on its size. From the Drude model [3], we

know that:

$$\epsilon_D(\omega) = 1 - \frac{\omega_p^2}{\omega^2 + i\gamma\omega}, \tag{2.8}$$

where ω_p is the plasmon frequency of the bulk metal and γ is the damping constant that relates to the width of the plasmon resonance band. γ relates to the lifetime associated with the electron-electron and electron-phonon scattering processes in the metal. On the other hand, in dielectric nanoantennas, surface plasmons are absent. The induced polarisability on interaction with light, creates Mie-like resonances which are tunable by varying the geometry. One of the most important feature that distinguishes plasmon resonances with Mie-type resonances in dielectric materials is the difference in losses. In metals, conduction electrons suffer from radiative damping and results in the dephasing of their coherent response. On the contrary, dielectric materials have extremely low losses and hence, naturally, a dielectric nanoresonator would exhibit a longer “dephasing" time. In Chapters 3 and 4, we address these contrasting dephasing properties with phase control experiments.

We will now proceed to discuss briefly two examples of controlling the interaction between fs pulses and single nanoemitters by tailoring the spectral phase and amplitude of the former.

2.4 One-photon phase control: fluorescence

Considering the interaction of a weak femtosecond pulse with a two-level system, given that $|g>$ and $|f>$ are the two states having energies E_g and E_f, the amplitude of the excited state is given by the first order perturbation theory [88] as,

$$a_f(t) = \frac{\mu_{fg}}{ih} \int_{-\infty}^{t} \epsilon(t_1) exp(i\omega_0 t_1) dt_1 \tag{2.9}$$

with μ_{fg} being the dipole moment matrix and ω_0 the frequency corresponding to the energy difference between the levels. It is clear that in such a case, the transition probability for a one-photon transition

depends only on the energy content of the frequency involved in the excitation spectral range as the expression involves no factor of the spectral phase.

For the experiment, we use single light harvesting complexes (LH2) which are the pigment-protein antenna complexes found in purple bacteria *Rhodopseudomonas acidophilas* involved in the preliminary stages of photosynthesis. These antenna complexes recently got wide attention due to the observation of long-lived coherences that are believed to be the reason for the extremely high energy transfer efficiency in the system, giving rise to two major discussions in the recent research: *quantum biology* and *artificial light harvesting systems* [89–94]. The LH2 has the absorption spectrum as shown in the Fig. 2.6 (c), due to the two closely lying rings of chromophores called B800 and B850 respectively, named respectively after their absorption peaks.

In this experiment, we try to measure the excitation spectrum of a single LH2 molecule [95, 96]. To measure the excitation spectrum of a given fluorophore, we first generate an interfering pulse pair and record the corresponding fluorescence. This Fourier approach has been demonstrated by generating the pulse pair with a mechanical delay line [97, 98] and very recently in single molecules [99]. This approach can also be realised using an SLM in our setup with suitable combination of spectral phase and amplitude shaping. Our method is free of beam-pointing instabilities and artifacts caused by mechanical errors in the driving mechanism of delay lines.

In the experiment, we apply the following combination of amplitude and phase to the SLM: $A = \mid \cos((\omega - \omega_c)\frac{\tau}{2}) \mid$ and $\phi = \frac{\pi}{2} sign(\cos((\omega - \omega_c)\frac{\tau}{2})) + 1)$ where τ is the delay and ω_c is the carrier frequency, as shown in Fig. 2.6 (a). The *sign* function takes values $+1$ when $\omega > \omega_c$ and -1 when $\omega < \omega_c$. By scanning the delay τ with step size < 1 fs, on measuring the fluorescence with an APD, we obtain a fluorescence excitation interferogram (Fig. 2.6 (b)). The oscillations are the result of interference of absorbed optical frequencies. The Fourier transformation of this linear autocorrelation trace

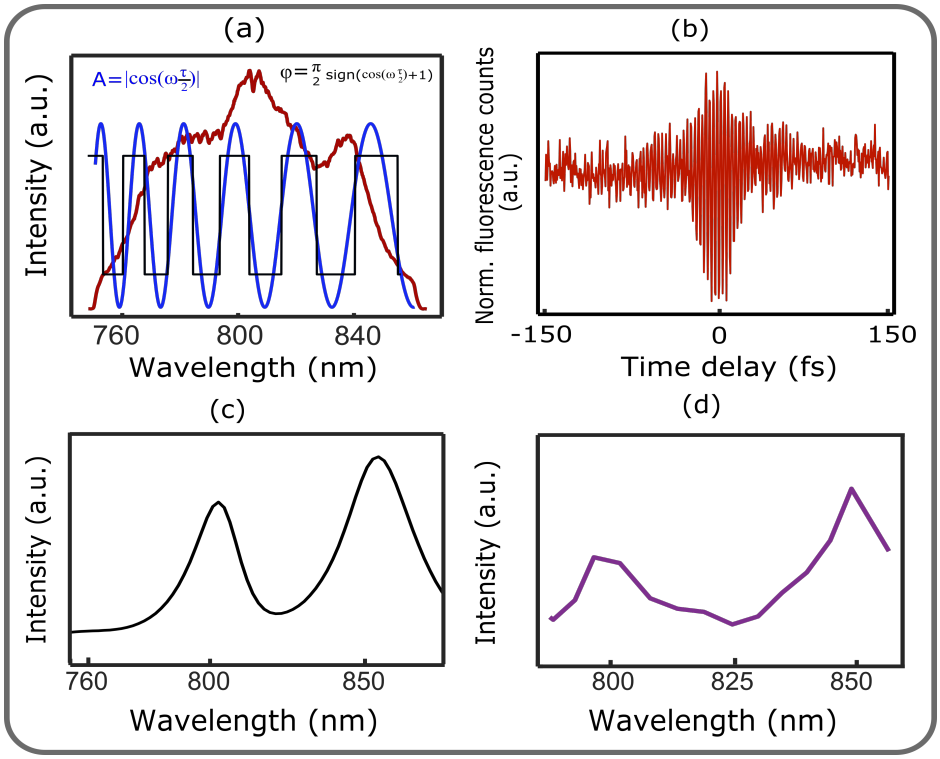

Figure 2.6: **One-photon phase shaping**(a)Excitation laser spectral profile with phase function and amplitude functions required to generate a pulse pair (b) Fluorescence interferogram obtained after a time-delay scan of laser pulses from -150 fs to 150 fs in sub-fs steps (c) ensemble absorption spectrum of LH2 solution (d) excitation spectrum of a single LH2 molecule obtained by Fourier transforming the interferogram.

would yield the excitation spectrum convolved by the laser spectrum, which on division by the latter yields the excitation spectrum of a single LH2 molecule Fig. 2.6 (d). Comparing with Fig 2.6 (c) we can see that the excitation spectrum of a single LH2 molecule matches well with the ensemble absorption spectrum of the system.

Although the excitation spectrum provides some information on the properties of the excited state of a molecular system under study, one can probe a coupled system of energy flow like LH2 through a pump-probe experimental approach. Such studies have been per-

formed at the single molecule limit by [51], however, there is a perpetual debate on the feasibility of weak field coherent control experiments [100]. Recently, in [101] it was shown that fluorescence intensity is independent of the absolute phase of the laser pulses and is only sensitive to phase between the pulses.

2.5 Two-photon phase control: second harmonic generation

The idea of phase control of two-photon transitions starts from the works from Broers et. al., and Meshulach et. al., [88, 102]. At higher excitation powers, where the optical response to the incident light is nonlinear, in a suitable material, a broadband laser can induce multiphoton excitation pathways, and the phase of each frequency within the pulse which results in the absorption process, can enhance or suppress a transition, as demonstrated in a series of works from Dantus et. al.,[84, 103–105]. This is achieved by realising quantum interference between the various pathways leading to the same final state. From the second order perturbation theory, one can write the amplitude of the excitation state as:

$$a_f(t) = \frac{\mu_{fg}}{-h^2}\mu_{fn}\mu_{ng}\int_{-\infty}^{t}\int_{-\infty}^{t_1} E(t_1)E(t_2)e^{(i\omega_{fn}t_1)}e^{(i\omega_{ng}t_2)}dt_2dt_1, \tag{2.10}$$

where $\omega_{ij} = \frac{(E_i - E_j)}{\hbar}$ and the summation is performed over all possible intermediate states of the system. Refraining from detailed derivations, this in the frequency domain representation, for a two photon transition turns into:

$$E^{(2)}(2\omega_0) = D(\omega) * \int_{-\infty}^{\infty} E(\omega-\Omega)E(\omega+\Omega)e^{i(\phi(\Omega)+\phi(-\Omega))}d\Omega. \tag{2.11}$$

Importantly, contrary to one-photon transitions, we can integrate over all the detuning contributions that add up to $2\omega_0$. Here $\Omega = \omega - \omega_0$ is the spectral detuning and $D(\omega)$ acts as a frequency filter that

defines the SHG efficiency for any given frequency in the spectrum, the significance of which will be clear in the following section. In other words, two-photon transitions occur for all pairs ω_i and ω_j which satisfies the condition $\omega_i + \omega_j = \omega_0$ and ω_i and ω_j lie within the excitation pulse spectrum. This means that two photon transition probability can be controlled by tailoring the spectral phase of the pulse. It is obvious that this probability is maximized for a given energy and power spectrum by the transform limited pulse, that is, when $\phi(\Omega) = 0$.

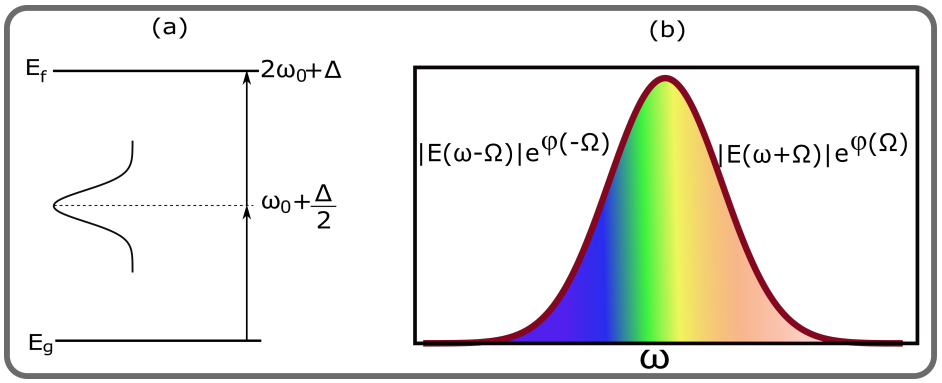

Figure 2.7: **The concept of spectral phase interferences with a broadband excitation**. (a) The energy level diagram that shows the interference of two-photon pathways to achieve a transition from E_g to E_f. (b) A broadband pulse can excite a 2-photon transition with any pair of frequencies that is detuned by Ω.

To demonstrate this control, we choose SHG, the most commonly studied nonlinear optical process. SHG is a parametric process where the frequency of an incident light beam gets doubled on interacting with a suitable nonlinear crystal. In classical nonlinear optics, SHG is defined as a process that results from the induced polarization in a material, following the interaction with an intense optical field. The induced instantaneous polarization response $\mathbf{P}$ of the material following the interaction with the incident optical electric field $\mathbf{E}$(r,t)

is expanded as a Taylor series of the amplitude of the field as:

$$\mathbf{P}(r,t) = \epsilon_0\chi^{(1)}\mathbf{E(r,t)} + \epsilon_0\chi^{(2)}\mathbf{E(r,t)}^2 + \epsilon_0\chi^{(3)}\mathbf{E(r,t)}^3... \quad (2.12)$$

where $\chi^{(n)}$ represents the $n-$th order susceptibility tensor with n being a positive integer that describes the optical properties of the medium and ϵ_0 is the vacuum susceptibility. The second order nonlinear response of any material, is thus governed by the $\chi^{(2)}$ of the material. If we use the contracted notation and symmetry conditions [106, 107], the $3 \times 3 \times 3$ - component $\chi^{(2)}$ tensor is reduced to a 6×3 - component nonlinear coefficient matrix d_{il}. This implies the Eq. (2.12) for SHG process simplifies to:

$$\begin{bmatrix} P_x(2\omega) \\ P_y(2\omega) \\ P_z(2\omega) \end{bmatrix} = 2\epsilon_0 \begin{bmatrix} d_{11} & d_{12} & d_{13} & d_{14} & d_{15} & d_{16} \\ d_{21} & d_{22} & d_{23} & d_{24} & d_{25} & d_{26} \\ d_{31} & d_{32} & d_{33} & d_{34} & d_{35} & d_{36} \end{bmatrix} \begin{bmatrix} E_x(\omega)E_x(\omega) \\ E_y(\omega)E_y(\omega) \\ E_z(\omega)E_z(\omega) \\ 2E_y(\omega)E_z(\omega) \\ 2E_x(\omega)E_z(\omega) \\ 2E_x(\omega)E_y(\omega) \end{bmatrix}. \quad (2.13)$$

It is clear from Eq. (2.12) that SHG is forbidden in a material with inversion symmetry. Thus isotropic crystals like Au, Ag, Si etc. cannot generate SHG from the bulk. However, in these materials at the surface, the symmetry is broken and SHG is permitted. On the other hand, it is also possible to use materials with high value of $\chi^{(2)}$, like III-V semiconductor materials to generate bulk SHG. Eq. (2.12) also implies that by enhancing the electric field intensity in nanomaterials with plasmonic or Mie resonances or by high-peak power fs lasers, we can generate efficient SHG as its intensity varies quadratically with the incident electric field. Strong electric field enhancement produced in the near-field of nanoparticles as a result of plasmonic or Mie resonances results in the enhanced second order or third order nonlinear optical processes as it has $\mid E \mid^2$ or $\mid E \mid^3$

dependence respectively. In Chapter 3 we demonstrate the enhancement of nonlinear optical process like two-photon photoluminescence, by plasmon resonance and the high peak power. In Chapter 4 and Chapter 5 we show the control of SHG and multi-photon photoluminescence by field enhancement due to Mie resonances and the high value of $\chi^{(2)}$. As the size of these nanoparticles are very small compared to the excitation spot size, phase matching conditions of the fundamental and the second harmonic frequencies are automatically fulfilled in our experiments.

The simplest nonlinear phase control experiment is to change the GDD, as illustrated in Fig. 2.8 (a), which results in the change of temporal duration of the pulse from its Fourier limit. Chirped pulses have been used for various different applications in the past [108–110]. From Eq. (2.11) we can obtain the SHG spectrum following chirp phase modulation as:

$$E^{(2)}(2\omega_0) = \int_{-\infty}^{\infty} E(\omega-\Omega)E(\omega+\Omega)e^{i(\phi_2\frac{(\omega-\omega_0)^2}{2!})}d\Omega * D(\omega) \quad (2.14)$$

Following this phase modulation, the temporal duration of the pulse will change according to Eq. (2.6). In our experiment, we excited single $BaTiO_3$ nanoparticles at the focus of the microscope and detected the corresponding SHG spectrum with the spectrometer, corresponding to different values of GDD from -1000 fs^2 to -1000 fs^2. The simulated SHG response, spectrally integrated, is shown in a log-log scale in Fig. 2.8 (b). Since the SHG intensity is $\propto \frac{1}{\tau}$, in a log-log scale we observe SHG intensity variation with respect to excitation pulse duration as a straight line with slope = -1 [111, 112]. As is clear from Fig. 2.8 (c), the SHG spectrum is symmetric around 0 fs^2, in addition to the symmetry around the central wavelength 395 nm. The result fits well with the simulated SHG response in Fig. 2.8 (d), calculated based on the excitation laser profile in our case.

We have concluded that transform-limited pulses are optimal as it excites a given transition from E_g to E_f in the most effective way possible with a given power spectrum. However, Meshulach et. al.

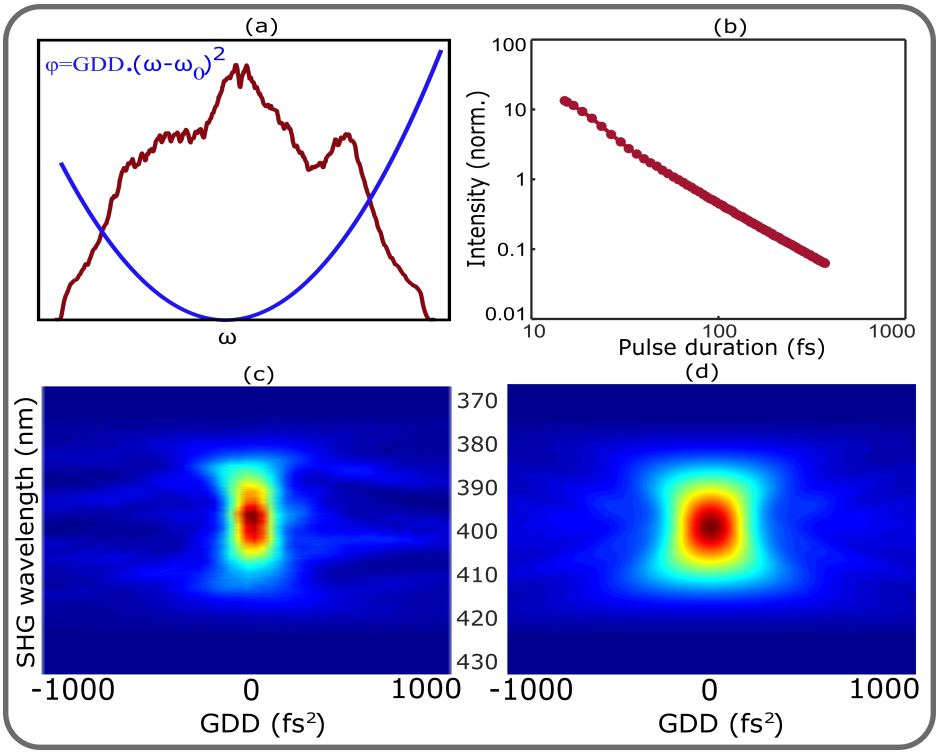

Figure 2.8: **Two-photon phase shaping with SHG** (a) The idea of GDD scan. The value of GDD describes the steepness of the parabolic curve. ω_0 is chosen to be the central frequency of the laser spectrum. (b) Calculated SHG signal as a function of applied GDD with an APD (c) Measured SHG spectrogram as a function of applied GDD phase, from -1000 to $+1000$ fs^2 (d) Simulated SHG spectrogram agrees well with the experimental data.

[88] have shown that pulses modified by a phase function antisymmetric around ω_0 is also optimal. This kind of π phase step is defined as:

$$\phi(\omega - \omega_0) = \frac{\pi}{2} sign(\omega - \omega_0) \tag{2.15}$$

where the *sign* function takes values ± 1 when $\omega > \omega_0$ and $\omega < \omega_0$ respectively. This means that $\phi(\omega)$ has a jump at ω_0 as described in Fig. 2.9 (a). If ω_0 is scanned through the laser spectrum, the integrated SHG intensity gets modulated due to the two-photon spectral

interferences as shown in Fig. 2.9 (b). Similarly, in Fig. 2.9 (c) shows the variation in SHG spectrum with the position of ω_{step}. Initially, when the ω_0 is at the blue part of the laser spectrum, the bluer part of SHG spectrum stays high compared to the red part. As ω_{step} reaches ω_0, the SHG intensity reaches almost zero except at $2\omega_0$. When $\omega_{step} = \omega_0$ the intensity reaches the maximum back again along the diagonal. In fact this can be explained in a simple way: From Eq. (2.12) it can be shown that SHG intensity will be also maximized for any phase antisymmetric around ω_0, in addition to a flat phase. However, we have not yet considered the influence of the filter function $D(\omega)$. For a thin nonlinear crystal, we can approximate $D(\omega)$ by a constant value over the excitation spectrum, because all the input frequencies are converted to the second harmonic frequencies corresponding to the respective spectral amplitude. Hence, the SHG spectrum gets modulated only as a result of the spectral interference. The Fig. 2.9 (d) shows the calculated spectrogram which nicely corresponds to the experimental result.

We now investigate the effect of spectral content and pulse duration of the excitation pulses in this experiment. To control the spectral content, we put Gaussian functions corresponding to different pulse durations as filter functions in Eq. (2.14) and calculate the SHG spectral evolution. This is achieved by replacing $D(\omega)$ with $e^{(-\log(4)*((\omega-\omega_0)./d\omega).^2)}$ where $d\omega$ is the full width at half maximum bandwidth of the Gaussian function. We find that in addition to the narrowing of SHG spectrum, the intensity modulation is also affected. This can be explained from the definition in Eq. (2.14), that when the spectral content that defines the interaction is narrow, the interference term has a constant value before the interference shows its effect in the spectral range available. This shows the direct effect of spectral phase modulation on the spectral content of the excitation laser.

In another approach, we introduced the GDD parameter to change the pulse duration and investigated its effect on the π step phase scan.

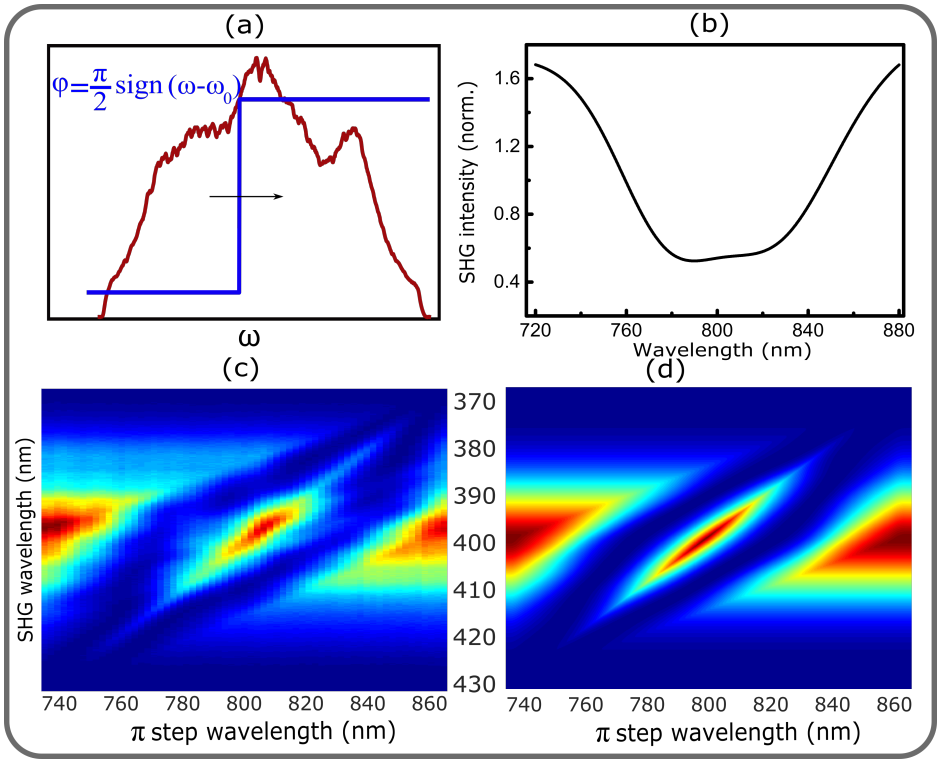

Figure 2.9: **SHG signal dependence on the spectral π step phase scan**.(a) The idea of spectral π scan (b) SHG signal variation measured with APD. (c) Measured SHG spectrogram (d) Calculated SHG spectrogram with the experimental parameters matches well with the observed one.

We found that for the GDD corresponding to the same pulse durations in the previous case, the SHG modulation response is completely different. Once again, this shows the relevance of spectral content of the excitation laser in a phase control experiment. In Fig. 2.10 (a), the SHG response is dominated by the frequency components available to interfere depending on the bandwidth that is varied, while in Fig. 2.10 (b), it is dominated by the interference of GDD phase (which is applied to chirp the laser pulse) and the π phase step corresponding to each frequency component.

So far in this section, we have decided the amplitude of the phase

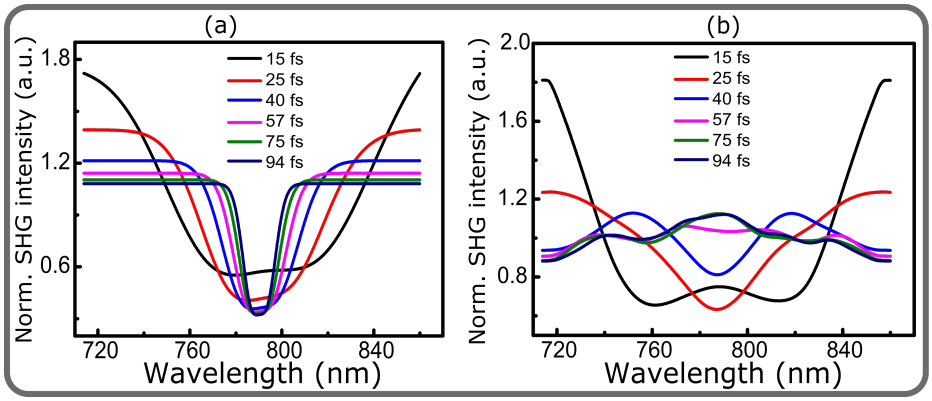

Figure 2.10: Effect of the spectral width and the temporal width on π step scan. (a) The calculated SHG response on π step scan with Gaussian filter functions of different spectral widths. (b) The calculated SHG response on π step scan with different pulse durations achieved by corresponding GDD parameters.

step to be π. To verify that π step phase is indeed the superior phase step to minimise a two-photon response, we measured the SHG response when the amplitude of the phase step applied a_{step} is varied from 0 to 2π (see Fig. 2.11 (a)). It is obvious from the result shown in Fig. 2.11 (b) that the minimum SHG intensity is achieved when the phase step amplitude is π. The calculated SHG response shown in black line nicely correlates with the observed SHG signal variation.

The ability to manipulate spectral phase and amplitude of the excitation pulses at the microscopic excitation volume has thus shown to be a useful tool in controlling nonlinear optical processes like SHG following the interaction of laser pulses with single photoemitters. As mentioned before, since SHG is sensitive to molecular symmetry breaking, it has found many useful applications in biological systems such as imaging collagen distribution, membrane potential etc. [113–120]. Most of these studies involve studying polarization dependence of second harmonic signal, due to the information it provides on the orientation of individual emitters in an ensemble [121–123], on the anisotropies in a material [124, 125], on the chiral properties of

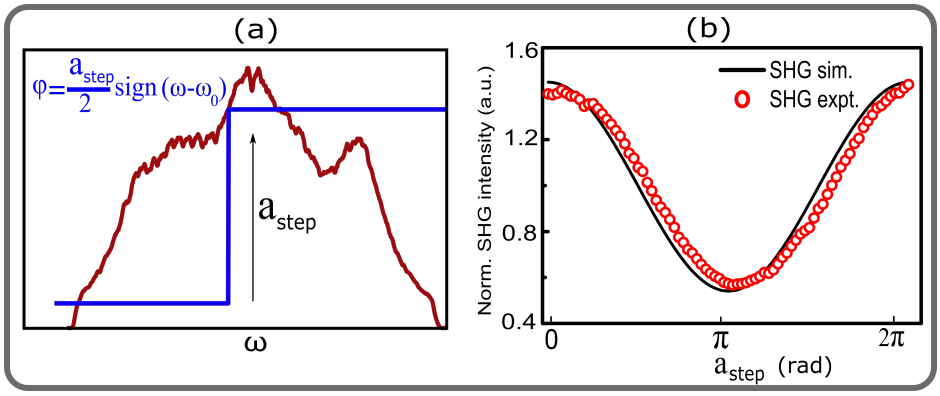

Figure 2.11: **SHG signal dependence on the amplitude of phase step**. As the amplitude is varied from 0 to 2π, the SHG signal drops and reaches minimum for $a_{step} = \pi$.

nanomaterials [126] etc. Therefore, we combine our nonlinear optical investigation with the polarization analysis, specifically described later in Chapters 5 and 6 to obtain insights on the nonlinear optical processes in resonant nanoantennas.

2.6 Polarization control of nonlinear optical processes

Polarization is a vectorial property of light that gives detailed information on the physics of light generation and scattering from a light-emitting source [127]. Mathematically, it is trivial to show that, for a light beam that consists of two independent orthogonal components with amplitudes E_x and E_y with different phases, its polarization can be described by:

$$\frac{E_x^2}{E_{0x}^2} + \frac{E_y^2}{E_{0y}^2} - 2\frac{E_x E_y}{E_{0x} E_{0y}} cos(\delta) = sin(\delta)^2, \tag{2.16}$$

where E_x and E_y are the instantaneous X and Y amplitudes, with E_{0x} and E_{0y} the corresponding maximum amplitudes and δ is the difference between X and Y phases. The Eq. (2.16) represents an ellipse as

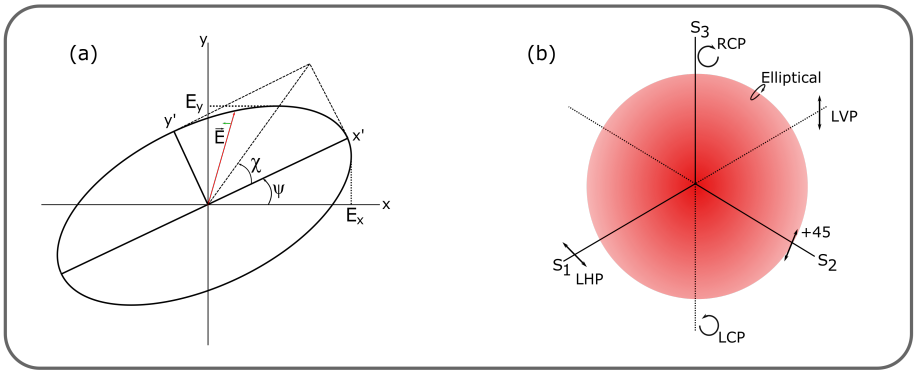

Figure 2.12: **Polarization ellipse and Stokes parameters**. (a) Polarization ellipse showing the orientation angle ψ and ellipticity χ. (b) Different states of polarization represented on the surface of Poincare sphere, whose three axes are the three Stokes parameters.

shown in Fig. 2.12 (a) called the *polarization ellipse* [128–130]. The Stokes formalism [130], is a generalised representation that transforms these parameters to the intensity (observable) domain that can be measured. By definition, the four Stokes parameters are S_0 (total intensity), S_1 (difference in intensities between horizontal and vertical linearly polarized components), S_2 (difference in intensities between linearly polarized components oriented at $+45^o$ and -45^o) and S_3 (difference in intensities of left and right circularly polarized components), in combination with degree of polarization (ρ), polarization orientation angle (ψ) and the ellipticity angle (χ). ρ is related to Stokes parameters via the relation $\rho = \frac{\sqrt{(S_1^2+S_2^2+S_3^2)}}{S_0}$ and shows if the light is polarized or not.

Experimentally, the Stokes parameters are determined by a polarimetry setup by combining a quarter-wave plate (QWP) and a linear polarizer before the emCCD camera, which records the SHG emission in six different polarization states: linear horizontal (LHP), vertical (LVP), two diagonal (Pol +45 and Pol -45) and two circular (RCP and LCP) as described by Eq. (2.17) - Eq. (2.20):

$$S_0 = I(0,0) + I(90,0) \tag{2.17}$$

$$S_1 = I(0,0) - I(90,0) \tag{2.18}$$

$$S_2 = I(45) - I(135) \tag{2.19}$$

$$S_3 = I(RCP) - I(LCP). \tag{2.20}$$

The ψ and χ are related to Stokes parameters as:

$$\psi = \frac{1}{2} tan^{-1}(\frac{S_2}{S_1}) \tag{2.21}$$

$$\chi = \frac{1}{2} sin^{-1}(\frac{S_3}{S_0}) \tag{2.22}$$

The Stokes parameters S_1, S_2 and S_3 are usually normalized by S_0, between the values -1 and +1. When $S_1 = \pm 1$ we have LHP or LVP, for $S_2 = \pm 1$ we have $\pm 45^o$ polarizations and for $S_3 = \pm 1$ we have RCP or LCP respectively. Also, $\chi = 0$ suggests linear polarization, $0 < \chi \leqslant 45^o$ suggests right handed and $-45^o \leqslant \chi < 0$ suggests left handed polarizations and it is perfectly circular at $\chi = \pm 45$. The values of ψ show the orientation of the polarization ellipse with respect to X axis. Thus, the Stokes parameters allow to determine any figure of merit for polarization by determining appropriate ratios between these parameters. Since $S_0^2 = S_1^2 + S_2^2 + S_3^2$, any state of polarization can be represented (detailed mathematical formulations in [3]) on the surface of a sphere, called the Poincare Sphere, as we show in Fig. 2.12 (b).

Polarization state of the emitted SHG from nanoantennas provide valuable insights to distinguish between various resonant antenna modes in those structures, as we will show in Chapter 5. Furthermore, in Chapter 6, we describe the first results of a novel experiment in which we combined the technique of spectral phase shaping with Stokes analysis to control modal interferences in nanoantennas.

2.7 Conclusions

To summarize, in this chapter we have introduced the fundamental mathematical formulation to describe the properties of broadband fs lasers. Following this, the theoretical and experimental schemes to perform spectral phase and amplitude modulation of these pulses at the nanoscopic excitation volume were provided. It was demonstrated that achieving Fourier-limited pulses at the excitation volume is important and the pulse compression routine that is followed to ensure that was described. Based on this background, we showed experimental examples of linear, one-photon and nonlinear, two-photon coherent control experiments on single nanoscopic light emitters. A specific π phase step coherent control scheme was introduced to control nonlinear optical responses that will be used in subsequent chapters to investigate a specific photoemitter system. Finally, the Chapter is concluded by adding the importance of polarization analysis of second harmonic generation studies of nanoscopic resonant systems and the mathematical formalism of Stokes analysis. To summarize, this Chapter provides fundamental background for the reader to identify the broad context of nonlinear optical investigations of different nanoscopic light emitting systems.

3

Phase control of plasmon resonances in Gold nanoantennas

Plasmonic nanoantennas emit two-photon photoluminescence, which is much stronger than their second harmonic generation. Unfortunately, luminescence is an incoherent process and therefore generally not explored for nanoscale coherent control of the antenna response. Here, we demonstrate that, in resonant gold nanoantennas, the two-photon absorption process can be coherent, provided that the excitation pulse duration is shorter than the dephasing time of plasmon mode oscillation. Exploiting this coherent response, we show the pure spectral phase control of resonant gold nanoantennas, with effective read-out of the two-photon photoluminescence.

3.1 Introduction

Surface plasmon resonances in nanoantennas result in the concentration of the electromagnetic field in subwavelength hotspots, which is widely explored to enhance the fluorescence [13, 14] and Raman scattering response of molecules [15, 16]. Beyond an enhanced amplitude, the electromagnetic field of the antenna resonance exhibits an intrinsic phase response, in space and time [131]. The subwavelength amplitude-phase feature allows nanoscale coherent control of the nanoantenna and manipulation of light-matter interaction at the nanoscale, to boost non-linear processes for the development of nanoscale devices. Unfortunately, owing to intrinsic metal losses, it is challenging to observe the coherent response of plasmons, as they are typically short-lived. The typical dephasing times for Au and Ag nanostructures vary from below 10 fs to few tens of femtoseconds [132, 133].

In pioneering theoretical papers Stockman and co-workers [134, 135] proposed the use of tailored phase modulation of excitation femtosecond pulses to control the spatial distribution of optical fields in nanostructures, provided the excitation time is ensured to be shorter than the dephasing time. Aeschliman et al [136] showed the control of the optical near field in the vicinity of silver nanostructures by means of two photon Photo-Emission Electron Microscopy (PEEM) and adaptive modulation of the excitation polarisation of femtosecond pulses.

For the best performance of a nanoscale plasmonic device, an all-optical control scheme is preferred. Control of light with light, exploiting nanostructures as a platform, has been shown by many groups. For example, Novotny and coworkers [137] proposed the control of intensity and direction of scattered light from a nanowire by adjusting the coherent interaction between the polarization currents generated by linear and second harmonic scattering. Sukharev et al [138], showed control of energy transport in a chain- structure of nanoparticles, adjusting polarization and phase between transverse and longitudinal plasmonic modes. While Papoff et al [139] proposed

to use the phase between excitation field and generated multiphoton signal to control absorption and scattering in nanospheres. Following the early proposal by Stockman and co-workers [134, 135] several groups modelled the response of nanoparticles to ultrafast broadband lasers. Gray and coworkers [140] calculated the spatiotemporal control of localised electromagnetic field hotspots on nanowire and nanocone systems with respect to the sign of the chirp of excitation laser pulses. Scherer and coworkers [141] demonstrated the generation, control and focussing of plasmonic wave packets in silver nanowire systems, while Hecht and coworkers [142] calculated deterministic spatiotemporal control of nano-optical fields in two wire plasmonic nanocircuits and asymmetric nanoantennas.

First ultrafast experimental optical coherent control was presented by Kubo et al [143] showing spatiotemporal dynamics of propagating plasmons at sub-femtosecond timescale using PEEM for nanoscale imaging, a technique picked up by several others [144–146]. The Zentgraf group [147] showed an all-optical control of a coupled plasmonic structure, controlling the phase between two competitive channels. Recently, the Lienau group [148] presented broad-band spectral interferometry at different spatial positions of a slit-groove structure to reconstruct the dispersion of the surface plasmon upon propagation. In another notable advancement, the Imura group combined near field microscopy with ultrafast nanoplasmonics and demonstrated the plasmonic wavepacket interference of two simulataneously launched higher-order plasmon modes in a long Gold nanorod, in a similar system to ours yet with a different experimental approach [149] In an earlier work, the same group had shown that on a rough gold film, the linear phase modulation of excitation pulses resulted in local variation of intensities which they attributed to the control of interference of local excitations [150] . Yet despite progress on detection and control of phase on propagation, a systematic, true optical coherent control on a fundamental dipole plasmon mode remains challenging due to the very short dephasing time of the plasmon oscillation in the 25 fs range.

3.2 Resonance enhanced two-photon photoluminescence

We first investigate the two-photon photoluminescence (TPPL) response of Au nanoantennas. Arrays of Au nanoantennas (each 50 nm in width, 50 nm in height and length increasing from 50 nm to 300 nm) were fabricated with electron beam lithography on a glass coverslip with a 10 nm thin indium tin oxide adhesion layer. The individual nanoantennas are excited at the focus of a high NA objective with the exciting laser polarized linearly along the long axis of the individual nanoantennas, at an average power of 6 X 10^4 W/cm^2 in the diffraction-limited spot, collecting the spectrally integrated TPPL signal in epi-fluorescence mode with 670 and 680 nm short-pass in front of the APD. We also used a 450 long-pass filter to make sure we reject the contribution of SHG. Fig. 3.1 (a) shows the TPPL image of the 50 μm x 50 μm nanoantenna array. We find that for 790 nm central wavelength, the resonant Au nanoantenna length is 140 nm, with a length distribution of 70 nm shown in (b). In Fig. 3.1 (c) we show the simulated extinction spectrum of a 120 nm long Au antenna, which shows the SPR peak at 800 nm.

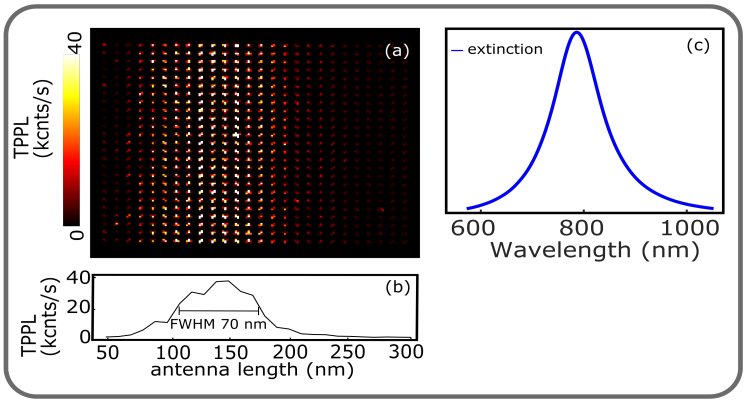

Figure 3.1: **Plasmon enhanced TPPL**. (a) TPPL image of an array of Au nanoantennas with increasing length from 50 nm to 300 nm (from left side to right side). (b) TPPL response shows the dipole resonance at antenna length of 140 nm. (c) Simulated extinction spectrum of a 140 nm Au nanoantenna showing plasmon resonance peak at 800 nm.

3.3 Power dependence of TPPL

Next, to investigate the power dependence of the two-photon signal in Au, we measured the two-photon spectra in the spectral range 370 nm to 650 nm corresponding to a sweep in excitation power, as it was varied from 0 to 60 kW/cm^2 in 51 steps by carefully varying the transmission mask in the SLM from 0 to 1. The Fig. 3.2 (b) shows the full TPPL spectrum of a single resonant Au nanoantenna. One can also identify the weak and narrow SHG spectrum in the range 370 nm to 440 nm.

Subsequently, we build a complete two- photon power spectrogram, average of many measurement cycles, which shows the evolution of the spectral response of the SHG and the TPPL to the variation in excitation power (Fig. 3.2 (c)). To derive the power dependence, we bin the collected spectrogram with a resolution of 6 nm and fit with the power law $I_{out} = \mathrm{a}I_{in}^{b}$ where I_{in} and I_{out} are the input and the output powers respectively. Fig. 3.2 (b) also shows the fit values of the b, the power law exponent, with error bars, plot-

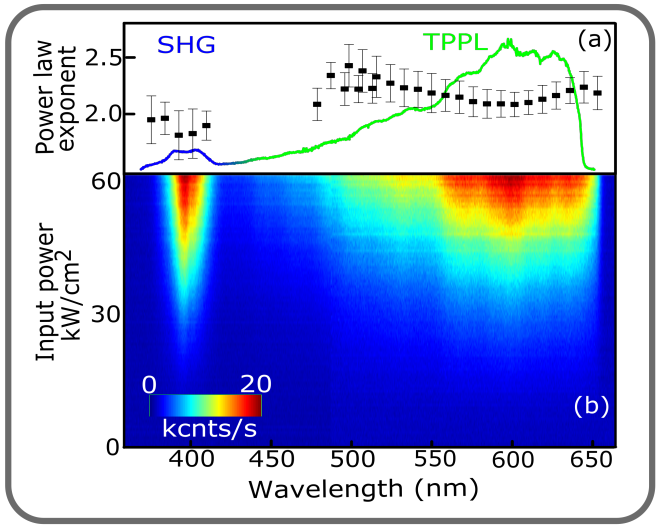

Figure 3.2: **Nonlinear optical response of a resonant Au nanoantenna**. (a) The two- photon spectrum of a nanoantenna showing the spectral range of SHG and TPPL. Spectrally resolved fit values for the power law shows that the SHG follows quadratic power dependence. The TPPL deviates slightly and has an average power dependence of 2.25. The excitation intensity is controlled by carefully varying the transmission mask in the SLM from 0 to 1 and the corresponding spectrum is collected by the spectrometer. (b) Evolution of the full two-photon spectrum for a sweep of input power from 0 to 60 kW/cm^2.

ted against the wavelength. The plot confirms the strict quadratic power dependence of SHG spectral response. The average power dependence of the TPPL is 2.25, which implies that there are possibly contributions from higher order absorption processes.

3.4 Phase response of TPPL

Next, we investigate the phase response of the TPPL. We start with a basic phase control experiment: increasing the second order dispersion of the excitation laser pulse from its shortest possible duration- the transform limit- to a given longer pulse duration, and collecting

the corresponding two-photon signal. As explained in the previous chapter, the 4f pulse shaper exerts the spectral phase control. A MIIPS pulse compression scheme, detecting SHG of $BaTiO_3$ nanoparticles at the microscope focus, (procedure described in Chapter 1) is applied to ensure the laser pulses are free of phase distortion in the excitation confocal volume. It has to be noted that, in our experiment, following the pulse compression, the compensation phase mask applied will result in a nearly zero phase across the full excitation laser spectral range for diffraction-limited laser pulse at the sample volume. Controlled second order dispersion was then sequentially added on top of this compensation spectral phase by sending appropriate voltage masks to the spatial light modulator. In our measurements, we used 301 phase masks with ϕ_2 from 0 to 5000 fs^2 keeping the pulse energy constant. As a control experiment, at first, we detected the SHG response of commercially available non-resonant $BaTiO_3$ nanoparticles (Sigma Aldrich), dissolved in ethanol, and drop- casted on a coverslip to obtain sparsely distributed nanoparticles on an area. We chose the $BaTiO_3$ nanoparticle as it is non-resonant with the laser spectral range and hence will not affect the spectral phase of the excitation laser field as we have shown in our previous works [151].

Fig. 3.3 shows the results. The SHG response with respect to pulse duration is proportional to τ^{-1}. A similar pulse stretch measurement on TPPL of Au nanoantennas shows a peculiar response. We observe that for long pulses the TPPL response decreases proportional to τ^{-1} similar to the SHG. At shorter pulses, the TPPL deviates to a plateau around c.a. 500 fs pulse length. A similar plateau was observed by Biagioni and coworkers [152, 153] for pulse duration τ ps, and was attributed to the lifetime of the intermediate state involved in the sequential 1 + 1 photon absorption mechanism observed in gold nanostructures [150].

Interestingly, in Au nanoantennas, beyond the plateau, we observe a 77 % increase in TPPL intensity as the pulse duration is further shortened from 100 fs down to 15 fs. We attribute the increase in TPPL response at the very short pulse duration regime to

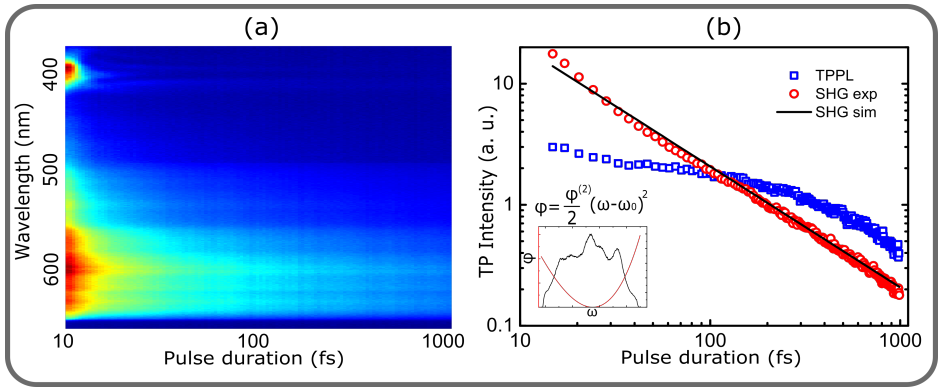

Figure 3.3: **Two-photon response on extending the pulse duration**. (a) Spectral evolution of TPPL and SHG on stretching the excitation pulses from 15 fs to 500 fs shows the differences slower drop in TPPL intensity compared to that of SHG (b) Integrated response in a $\log - \log$ scale shows SHG has slope -1 throughout the whole range of pulse durations. TPPL on the otherhand, exhibits a plateau for short pulses.

the contribution of coherent plasmon oscillations, as the onset of the coherent τ^{-1} response, which becomes relevant on these timescales. Our experiment suggests that TPPL, regarded as an incoherent process, develops a phase response on the timescales faster than the dephasing of the plasmon resonance.

3.5 Phase control of plasmons

A coherent two-photon excitation is readily turned from constructive into destructive interference by a π phase flip in one of the two excitation steps. With this in mind, we added a static π phase step at the central frequency ω_0 in the laser spectrum, in addition to the second order dispersion. In fact, such π phase step has been previously used to effectively control various nonlinear optical processes in various systems [154]. The combination of π step and ϕ_2 means that, in addition to the excitation pulses getting stretched temporally there is a π phase difference between blue and red halves of

the laser spectrum, i.e., between the collective two-photon pairs contributing to the two-photon absorption process. Any phase response that exists depending on the excitation pulse duration would reveal its signature on applying such πspectral step. The spectral π phase step was defined in Eq. (2.14). The sum of Eq. (2.12) and the Eq. (2.14) will then form the effective phase mask for this experiment. In spectral domain, the SHG spectrum can be calculated by Eq. (2.10). The SHG spectrum is then given by:

$$E(2\omega) = \mid \int \mid E(\Omega) \mid\mid E(\Omega) \mid e^{i(\frac{\phi_2}{2}(\Omega)^2 + \frac{\pi}{2} sign(\Omega))} \mid^2 \tag{3.1}$$

From Eq. (3.1), the integrated intensities I for varying ϕ_2 can be deducted. We define the relative difference between I_{ϕ_2} and I_π, the intensities using chirped laser pulses with and without a π step mask, respectively, as the coherent contrast β as:

$$\beta = \frac{I_{\phi_2} - I_\pi}{I_{\phi_2}}\% \tag{3.2}$$

The most interesting observation here, is the difference in β between TPPL and SHG. At the transform limit, $\beta_{TPPL}$is non-zero and about half of . Thus the TPPL does respond to pure phase control, confirming the coherent nature of the short-pulse onset observed in Fig. 3.3. On increasing ϕ_2, β_{TPPL} diminishes rapidly, to reach zero at ,corresponding to pulse length, and maintains at zero for longer pulses. This clearly demonstrates the differences in the coherent response between TPPL and SHG. TPPL shows coherent response on a very short timescale within the decoherence time, until which the plasmon oscillations preserve some phase memory. Beyond 50 fs the temporal length of the excitation laser pulse becomes unable to coherently drive the plasmon oscillations. We modelled this response, introducing a decoherence term into Eq. (3.1) to take into account the dephasing time of the plasmons in the gold. From the fit to the data in Fig. 3.4, we extracted a decoherence time of c.a. 30 fs, which is of the same order of the values reported in the literature in similar

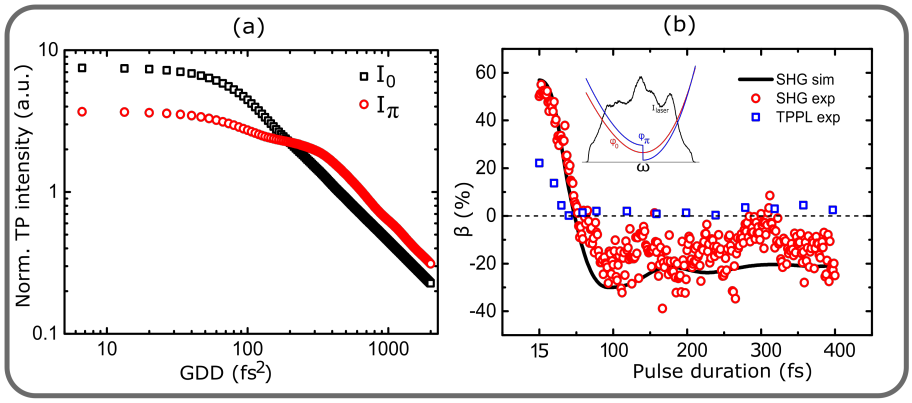

Figure 3.4: **The coherent contrast β of TPPL and SHG on extending the pulse duration**. (a) The SHG response I_π with a π step at ω_0 compared to I_0, that without a π step, plotted in a $\log - \log$ scale shows that I_0 and I_π cross over each other at GDD $= \phi_c$. After ϕ_c, I_π dominates and maintains a constant difference with I_0. (b) The SHG shows strong contrast for any pulse length and cross zero at 250 fs^2. The TPPL contrast decreases and reaches zero at a ϕ_2 value of 200 fs^2 which is around 50 fs pulse duration. The inset shows the spectral phase of a simple quadratic phase (ϕ_2) and with a spectral π step phase on top of it (ϕ_π)

.

systems. Beyond this timescale, the two-photon excitation process in Au nanoantennas becomes dominated by the intermediate state dynamics, which has a lifetime of 600 fs.

We also investigated the trend of β of SHG with the change in ω_{step}. We found that, although the general trend is preserved, there are differences both in ϕ_c and the extend to which β goes below the zero value. The maximum value for β remains almost constant across the whole spectrum. Fig. 3.5 shows the result.

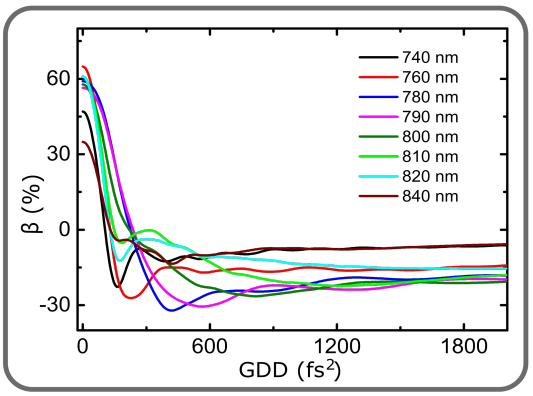

Figure 3.5: **The variation of β with ω_{step}.** The maximum value of β changes from c.a. 50% to c.a. 30% depending on the spectral content before and after ω_{step}. The minimum β is achieved when $\omega_{step} = \omega_0$.

3.6 Conclusions

To summarise, in this chapter, we have presented pure phase control of the nonlinear response of a resonant gold nanoatenna. By combining GDD phase and a π step phase on a 15 fs Fourier limited pulse, it is possible to distinguish and differentiate a true coherent process from a time-dependent coherent process. We show that the broadband TPPL can be coherently controlled by the spectral phase, provided the excitation pulse is short enough compared to the plasmon mode decoherence time of c.a. 30 fs. Our method is effective to determine dephasing times and phase control contrast in nanoplasmonic systems, with application in nanoparticle labelled two-photon imaging.

4

Multiphoton phase control of resonances in GaP disks

High-index dielectric nanoantennas have recently emerged as promising alternatives to plasmonic nanoantennas for concentrating and manipulating light at the nanoscale. For example, gallium phosphide (GaP) nanoantennas display extremely low losses in the visible range and high nonlinearities, support both electric and magnetic resonances, and are nicely compatible with CMOS fabrication technology. Especially, the low losses and large nonlinearities are promising for ultrafast optical switching and truly all-optical control of GaP nanodevices. Here first we use two- and three-photon excitation of GaP nanodisks to probe the size-dependent resonance enhancement of second-harmonic and bandgap emission. Next, it is shown that, by spectral phase control of broadband pulsed excitation, GaP nanoantennas outperform their metal counterparts in supporting nonlinear optical coherences.

4.1 From plasmonic materials to dielectric materials

Most of the exciting features of metallic nanoantennas result from localized surface plasmons (LSPs). However, the ohmic losses due to free-electron scattering in metals limits dephasing times of LSPs. Also, nanoplasmonics suffers from lower mode volume and low laser damage threshold. For this reason, the coherent control of nanoscale nonlinear optical excitations in metal nanoantennas has been limited to ultrashort pulses below 30 fs. In this context, all-dielectric nanoantennas with high refractive indices, like Si, Ge or combinations of III-V materials, such as gallium arsenide (GaAs), aluminum gallium arsenide (AlGaAs), gallium nitride (GaN), aluminium arsenide (AlAs), gallium phosphide (GaP), have attracted great attention as alternative candidates for metal nanoantennas due to their ultra-low losses and high compatibility with semiconductor processing technologies [155–161]. Fabrication techniques including lithography, chemical methods have been developed for realising all-dielectric nanostructures. Due to the lack of free carriers, in dielectric materials, the real part of dielectric function is positive and light can propagate inside the material. Additionally, such structures support optically-induced Mie resonances in the visible and near-infrared range, allowing wide wavelength tunability and field enhancement. In addition, unlike their metallic counterparts, they can support both strong electric and magnetic modes, bringing up unique optical properties. The whole research direction of all-dielectric nanophotonics got triggered by the work that showed localized magnetic dipolar mode excited in silicon particles [162]. Since then, there has been a broad spectrum of research that displayed various resonance-induced effects [163–168].

Apart from the resonant effects, dielectric nanoantennas with high second- and third-order nonlinear susceptibilities are specifically useful in enhancing and manipulating various nonlinear optical processes, like two-photon absorption (TPA), second harmonic

generation (SHG), third harmonic generation (THG), optical Kerr effect (OKE) and nonlinear mixing [165, 169–171]. Their strong intrinsic nonlinear response, aided by field enhancement when excited resonantly, make these materials ideal for nonlinear optical coherent control experiments. Although promising material systems with exciting properties have been introduced, studies on ultrafast spatio-temporal control of nonlinear optical responses have focussed either on active control of scattering in metamaterials [172], optical switching [164, 173], beam steering [174] etc. Despite this advancement, an all-optical spectral phase control of nonlinear optical processes in a dielectric nanomaterial system has not been demonstrated yet.

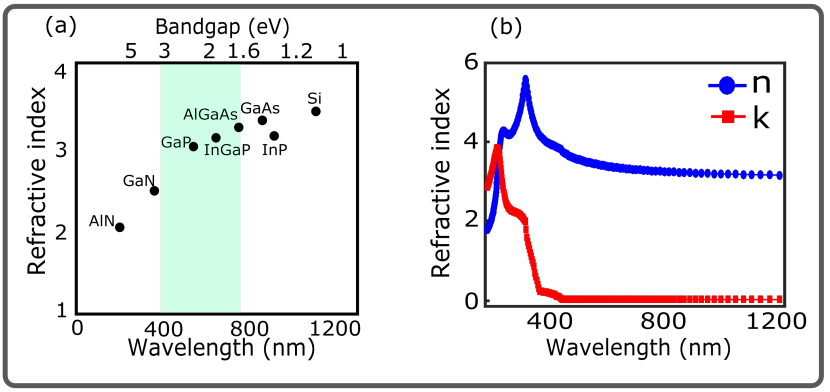

Figure 4.1: **GaP as a dielectric nanoresonator**. A comparison of different high index materials reported in nanophotonics research shows that GaP has the highest refractive index for materials that are transparent both in the NIR and visible range [175]

In our study, we focus on GaP, which is an indirect bandgap semiconductor with a bandgap of 2.24 eV [176]. It has zinc blende crystal structure and belongs to $\bar{4}$3m symmetry group. Due to the broad transparency range and low optical absorption [177], it is widely used in manufacturing red, orange and green light emitting diodes [178, 179]. It has a refractive index of 3.19 and 4.19 at 800 nm and 400 nm wavelengths respectively [180]. On comparison with other

high index dielectric materials described in Fig. 4.1, it is clear that GaP which has the highest refractive index of all the materials which are transparent both in NIR and visible region, is also as a consequence, one of the few available materials with high nonlinearity in that spectral region. This has enabled the use of GaP in frequency doublers in a wide wavelength range, as nanoantennas for enhancing photoluminescence and fluorescence in visible range [170], etc. In this Chapter, we will focus on exploring the performance of GaP nanodisks in supporting nonlinear optical coherences and compare it with our results in Chapter 3.

4.2 Nonlinear resonant response of GaP nanodisks

The sample investigated consists of arrays of GaP nanodisks of 210 nm height and diameters (D) varying from 80 nm to 560 nm was fabricated by patterning a 350 μm thick crystalline GaP (100) wafer via e-beam lithography, followed by an etching procedure as described elsewhere. A 4 μm center-to-center pitch was chosen to prevent optical coupling between adjacent resonators. The nanoantennas were excited with our laser tuned to a central wavelength of 790 nm in the setup as described in Chapter 2. The laser pulses were focused onto individual nanodisks by a 0.85 numerical aperture, 100X air-objective from the air side. The sample was placed on a XYZ piezo stage to enable scanning, and the nonlinear signal from single nanodisks was detected in reflection geometry using APD or the spectrometer coupled to an emCCD camera.

First, to study the nonlinear response of the nanodisks, we evaluated their emission spectrum in the visible range by pumping at different average excitation intensity up to 5 GW/cm^2, with linearly polarized light. Fig. 4.2 (a) shows the emission spectrum of a nanodisk. Two distinct regions can be noticed: SHG emission centered at 395 nm, and a 30 nm-wide luminescence band centered at 550 nm,

which we attribute to excitonic emission as it corresponds to GaP bandgap wavelength. Fig. 4.2 (b) shows the evolution of the nonlinear spectrum with power. The experimental data was fitted with a power law $\propto I^m$, where I the incident power and m the exponent in the power dependence. Fig. 4.2 (a) shows the fitted power exponent m at the different emission wavelengths, revealing that SHG obeys a quadratic power law (m = 2), as expected, while the 550 nm band demonstrates a cubic power dependence (m = 3), indicating that the excitonic emission is dominated by 3-photon absorption.

To confirm the nonlinear nature of the excitonic component of the spectrum, we performed interferometric frequency-resolved optical gating (iFROG) scans at different excitation power levels. In an interferometric intensity autocorrelation measurement, the ratio r, of the intensity at zero delay to the baseline intensity at infinite delay, is related to the order m of the multiphoton process as $r = 2^{2m-1}$. The obtained iFROG spectrograms, integrated over the excitonic emission range, as shown in Figure 1c, indicate that both 2 and 3 photon processes coexist at low excitation powers (3 GW/cm^2, red curve), while a 3-photon process governs (r = 32:1) when the power is increased (5 GW/cm^2, blue curve), i.e. multiphoton photoluminescence (MPPL). Black data in the graph corresponds to SHG, displaying the expected second order response (r = 8:1).

Next, we analyzed the influence of the GaP nanodisk size and corresponding Mie resonances on the SHG and MPPL emissions. To that end, nonlinear raster scan images of 5x5 arrays of GaP nanodisks of increasing diameter (80 to 560 nm) were attained, exciting the sample at average excitation intensity of 1 GW/cm^2 for SHG and 5 GW/cm^2 for MPPL. These power levels enabled the study of 2 (SHG) and 3 (high-power MPPL) photon processes, with sufficient signal-to-noise ratio, while larger excitation powers for either nonlinear process would have saturated the APD. Dichroic filters were used to isolate either the SHG signal or the MPPL contribution. Fig. 4.3 (a) shows, from left to right, a scanning electron microscope (SEM) image of a 5x5 disk array with corresponding registered SHG

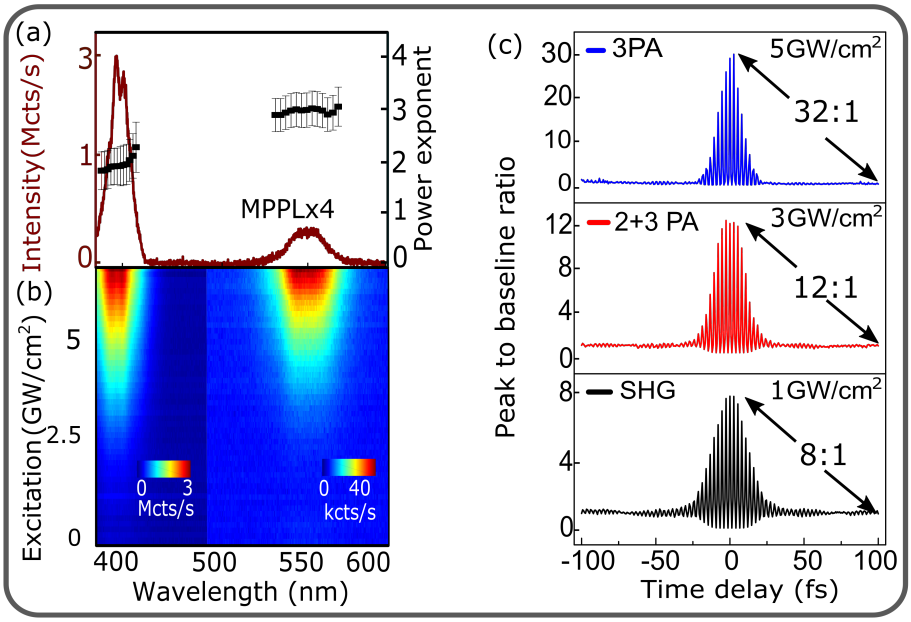

Figure 4.2: **Multiphoton spectral response**. (a) Nonlinear emission spectrum of a 440 nm diameter GaP nanodisk, and exponent of power law fits at different wavelengths. (b) Evolution of GaP nanodisk SHG and bandgap emission spectrum with the excitation power. SHG data was acquired for excitation powers up to 1 GW/cm^2 and normalized to bandgap emission power levels to enable comparison. (c) iFROG scans for the different nonlinear signals. SHG (black curve) demonstrates a second order process. Bandgap emission reveals a 2+3 photon absorption effect at low powers (red curve), that becomes a pure 3-photon absorption process at high powers (blue curve).

and MPPL images in (b) and (c). Both SHG and MPPL response present relative maxima at specific diameter values. To establish the origin of this effect, we performed numerical simulations of the scattering cross section and near-field distribution of the nanoantennas, using the commercial software *Lumerical* (Fig. 4.3 (e)). The complex refractive index of GaP was determined from measured ellipsometry data and used as an input for the numerical calculations.

Given that SHG and 3-photon absorption photoluminescence scale with the fourth and sixth power of the incident electric field ampli-

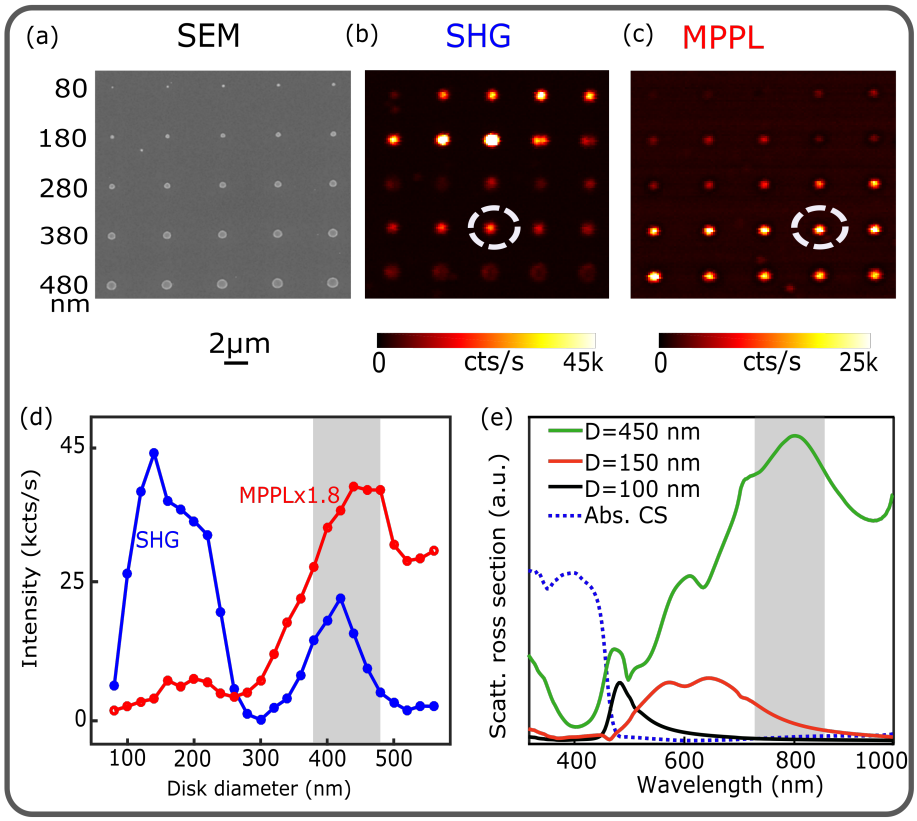

Figure 4.3: **Multiphoton resonant response**. (a) SEM image of the GaP nanodisk array. The disk diameters increase from 80 nm to 560 nm in steps of 20 nm. (b)SHG scan image showing the size dependent resonances (c) The corresponding MPPL scan image. The resonant nanodisks for the experiment are encircled. (d) SHG and MPPL intensities as a function of disk diameter. MPPL intensity is scaled by 1.8 times to fit into the plot. (e) Simulated wavelength dependence of the scattering cross section of GaP nanodisks of different diameters. The dashed blue curve shows the simulated absorption cross section of D=450 nm disk. The grey shaded area represents the wavelength region of the excitation laser, which resonates with disk sizes around 440 nm diameter, matching with the disk sizes encircled in (b) and (c).

tude, respectively, a strong increase in the signals is expected when the fundamental wavelength is at resonance, explaining the observed

peaks at D = 440 nm in Fig. 4.3 (d). The additional measured maxima at around D = 100 nm for SHG and D = 200 nm for MPPL would arise from resonances at the emission wavelengths, as indicated by numerical calculations for disks of smaller sizes. We attribute differences between experimental and simulated resonant wavelengths and diameter values to imperfections in the fabrication process especially for disks of the smallest diameters. Fig. 4.3 (d) also reveals that small resonant diameters outperform large resonant sizes for SHG, while the opposite occurs for MPPL. This can be explained by the broad scattering resonance for D = 440 nm in Fig. 4.3 (e) which also covers the 550 nm band (but not the SHG wavelength), giving rise to a doubly resonant effect that further boosts the MPPL emission, as has been observed in nonlinear nanoantennas with resonances at both the excitation and emission wavelengths. In addition, since the resonance at the fundamental wavelength has a stronger influence on the MPPL process, being of higher order than SHG, a particularly large reduction in the MPPL emission intensity is expected at the smallest diameters, where the resonance at the fundamental wavelength is absent. We also note that the absorption cross section (shown as dashed blue curve in Fig. 4.3 (e)) does not change much with the disk sizes due to substrate effect.

In the next section we will shift our focus to phase control experiment on MPPL and its results. In Chapter 5 we will show our detailed study on the resonant enhancement of SHG.

4.3 Phase control of multiphoton photoluminescence

We turn now our attention toward the phase control experiments, which were performed on the nanodisk of 420-460 nm diameter, as they deliver both efficient SHG and MPPL. Firstly, we measured the temporal response of the nonlinear signals when chirping the excitation beam. In this experiment, we varied ϕ_2 from -1000 fs^2 to 1000

fs^2. In time domain, this corresponds to stretching the pulse from 14 fs to 190 fs. It is important to note that positive and negative values ϕ_2 imply the same result in time domain. The obtained multiphoton phase spectrogram, averaged over 400 scans, is shown in the top and bottom left panels of Fig. 4.4 (a) demonstrating that the SHG spectral intensity falls off slower than the MPPL signal.

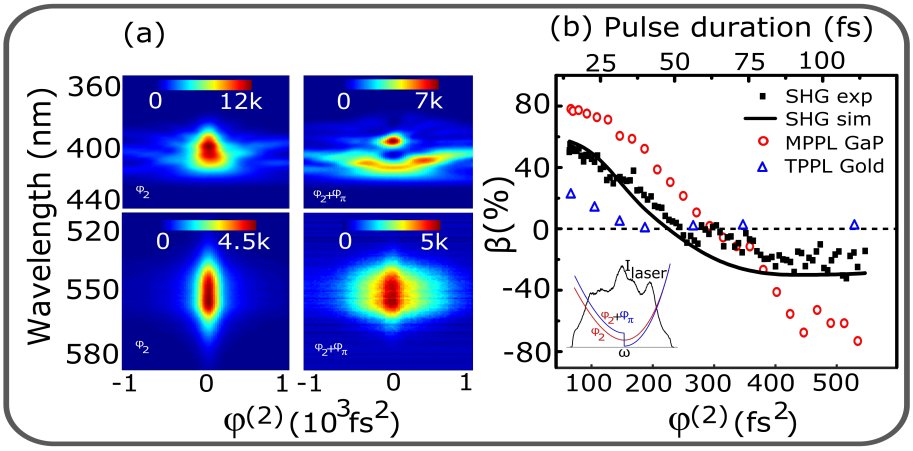

Figure 4.4: **Multiphoton phase response**(a) GDD scans for SHG and MPPL without (left panels) and with (right panels) an additional π step. (b) Integrated spectral intensities fitted with a second order and third order temporal dependence.

Next, in addition to ϕ_2, we added a static π phase step at a frequency ω_{step} in the laser spectrum. We have described the use of this type of phase step in Chapters 2 and 3 as an efficient control for two-photon processes. The top and bottom right panels of Fig. 4.4 (a) show the result of applying $\phi_2 + \phi_\pi$ to the laser pulses at $\omega_{step} = \omega_0$. A wider response in phase is now observed in the SHG and MPPL scans. In Fig. 4.4 (b), we show quantitatively the differences in the phase response of SHG and MPPL with the coherent contrast β. We plot β against ϕ_2. When $\phi_2 = 0$ fs^2, the contrast for MPPL (β_{MPPL}) is c.a. 80 %, which is a factor of 1.4 higher than that for

SHG β_{SHG} which is c.a. 58 %. The theoretical SHG response is shown in black solid line, as calculated from the laser spectrum using standard nonlinear theory described in Chapters 2 and 3. As ϕ_2 is increased, β_{MPPL} drops and crosses the zero level at 330 fs^2, while β_{SHG} is found to fall faster, crossing the zero level at 250 fs^2, flipping sign to remain constant at approximately -20 %. Remarkably, for MPPL, when ϕ_2 is further increased, its corresponding β value grows further in the negative direction reaching -70 % at c.a. 500 fs^2, highly surpassing the performance of SHG.

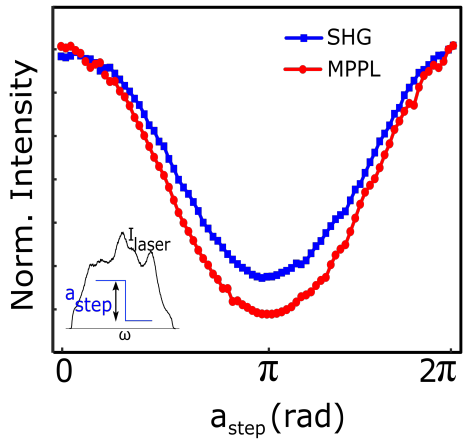

Figure 4.5: **Strength of π phase step**. The dependence of the nonlinear intensities on the phase step height a_{step} applied to the laser pulse a frequency ω_0. For both SHG and the MPPL, the intensity minimum is achieved when the step height is π.

Clearly, the 3-photon absorption is much more sensitive to spectral change than the 2 photon counterpart. For reference, Fig. 4.4 (b) also includes TPPL (two-photon absorption photoluminescence) results obtained from a resonant Au nanoantenna as described in Chapter 3, which exhibits the poorest of contrasts and shortest of coherence times, as limited by the reduced dephasing times of LSPs.

Finally, to evaluate the strength of our phase step in controlling the multiphoton processes, we varied the amplitude of the phase step

(a_{step}) between 0 and 2π at GDD = 0 fs^2 and studied its effect on the nonlinear signals. In all cases, the results showed a single minimum on a full sweep. Fig. 4.5 shows the case of $\omega_{step} = \omega_0$, which reveals that both SHG and MPPL responses drop to a minimum for a step of phase amplitude π, proving the strength of the π step in influencing the nonlinear processes. Again, the MPPL shows the strongest effect, yet for a 3-photon interaction, it is surprising to find the optimum at a phase difference of π.

4.4 Conclusions

In summary, we have studied the spectral phase control of nonlinear optical responses in GaP nanodisks at Mie resonances supporting efficient SHG and MPPL. By combining a dynamic GDD scan and a static π phase step on a 14-fs excitation laser pulse, the differences in the coherent responses between the MPPL and SHG processes was determined. It is observed that the coherent contrast for the MPPL effect is a factor of 1.4 (3.5) higher than that achieved for SHG at GDD = 0 fs2 (GDD > 500 fs^2. Notably, the coherency of the MPPL signal in the GaP nanodisk antenna outlasts that of the TPPL emission from its metal counterpart, demonstrating the potential of dielectric nanocavities for realizing coherent nonlinear nanodevices.

5

Angular SHG emission and multipolar analysis of GaP nanodisks

In Chapter 4 it was shown that high index dielectric nanoantennas with intrinsically high nonlinearity, such as GaP, provide a useful platform for size dependent nonlinear optical resonances and coherent multiphoton phase control experiments with coherences that outperform their metallic counterparts. In this Chapter we focus on an understanding of optical modes behind the SHG enhancement and its properties. Specifically, the generation and enhancement of SHG in GaP nanodisks is studied, also based on numerical simulations. Furthermore, we determine the angular radiation pattern of the nanodisks and present a full Stokes analysis to obtain insights on the multipolar modes in the resonant nanodisk. Finally, our experimental observations are confirmed with multipolar decomposition in the nonlinear spectral domain.

5.1 Introduction

According to recent studies, in dielectric nanoantennas, high nonlinear conversion efficiency for second- and third- harmonic generation were achieved either by exciting electric and magnetic dipole resonances [163, 165, 181], Fano resonance or collective modes [182–184], anapole states [169, 185, 186] etc. It was also shown that the overlap of electric and magnetic resonances can result in a huge SHG enhancement in nanostructures [187].

In our case, GaP nanodisks support both second order (SHG) and third order (MPPL) nonlinear optical resonances in the visible range, as we have demonstrated in Chapter 4. However, MPPL is an incoherent process and requires higher excitation intensities, while SHG is a coherent and instantaneous process. Additionally, resonances can enhance the conversion efficiency and reduce the required excitation intensity. Thus, the study of SHG resonant effects is more interesting at moderate excitation intensities. Although a recent work has shown huge enhancement of SHG from GaP nanodisks [170], a direct analysis of the responsible mechanisms is lacking. Therefore, in this Chapter, we concentrate our investigation on the SHG enhancement in GaP nanodisks.

As described in Chapter 1, electromagnetic field, on interacting with a dielectric material, will create a movement of bound charges in the material and induces a polarization $\mathbf{P}(2\omega)$ in the SH frequency 2ω by the second- order nonlinear interaction. Therefore, SHG occurs only in non-centrosymmetric crystals, provided that phase matching conditions are satisfied. However, we also know that, in nanoparticles, the combination of three effects- (a) symmetry breaking on the surfaces, (b) large surface-to-volume ratio and (c) huge concentration of electromagnetic fields on resonant excitation- help to enhance SHG response [188, 189]. Therefore, a non-centrosymmetric crystalline nanoparticle is an ideal choice for studying the enhancement of second harmonic generation.

From Eq. (2.12), we know that second harmonic electric field $\mathbf{E}(2\omega)$ is given by:

$$\mathbf{E}(2\omega) \propto \mathbf{P}^{(2)}(2\omega) = \chi^{(2)}\mathbf{E}(\omega)\mathbf{E}(\omega) = 2\epsilon_0 d_{eff}\mathbf{E}(\omega)\mathbf{E}(\omega) \qquad (5.1)$$

where, d_{eff}, the nonlinear coefficient matrix, is a material property. Thus, high SHG intensity can be achieved by either choosing a material with high d_{eff}, and increasing electric field intensity $\mid E(\omega) \mid^2$ during the interaction.

GaP has high nonlinear optical coefficient (d_{eff} = 70 pm/V) compared to other conventional SHG materials used in the visible range, such as $LiNbO_3$ (31 pm/V), β-$BaBO_3$ (2.5 pm/V), KDP (0.44 pm/V), KTP (3.4 pm/V) etc. Although AlGaAs has higher nonlinear coefficient (180 pm/V), the efficiency of SHG in the visible range is affected by its relatively large absorption in this region. The damage threshold of GaP following light illumination is quite high, which permits high excitation intensity. Thus, among dielectrics, GaP is an excellent material for SHG generation in the visible spectral range. In the next section, we investigate this resonant SHG enhancement due to field confinement in GaP nanodisks.

5.2 Resonant SHG enhancement in GaP nanodisks

To analyse the strength of SHG in GaP nanodisks, a 2D SHG scan image of the nanodisk array described in Chapter 4 was prepared. Individual nanodisks were excited by Ti: Sapphire laser pulses (pulse width 15 fs, central wavelength 800 nm, 100 nm FWHM, 85 MHz rep. rate) with average excitation intensity set to 3 GW/cm^2. The SHG signal was collected in the reflection configuration by single-photon counting APD, setting 440 nm and 680 nm short-pass filters in addition to a 670 nm short-pass dichroic. At this excitation intensity, we verified that we do not collect any higher order luminescence signal in the APD by power dependence measurements. The SHG intensity

showed a quadratic dependence on excitation intensity. In Fig. 5.1(a) we show the SHG scan image of the array and in (b) we show the average SHG intensity of individual disks. The error bars show the standard deviation of SHG intensity over three identical arrays in the sample. In the array with disk diameters from 80 nm to 560 nm, we

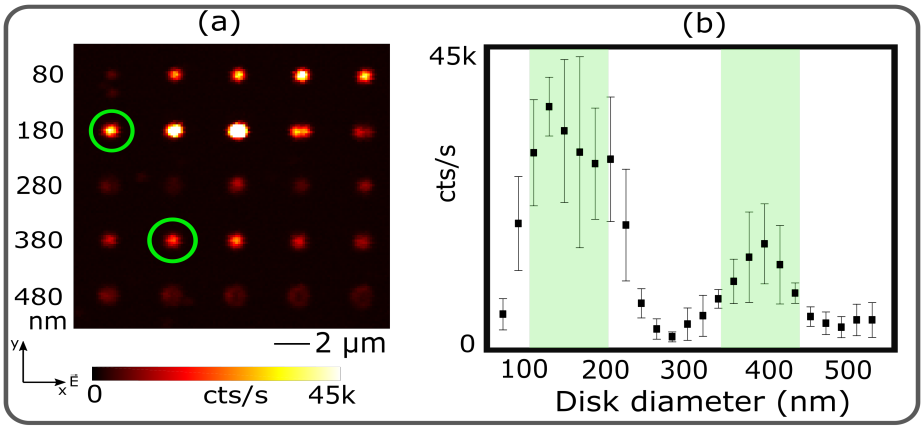

Figure 5.1: **SHG resonances** (a) The xy SHG scan image of the array of GaP nanodisks with diameters from 80 nm to 560 nm in steps of 20 nm. The green circles correspond to the resonant disk sizes. (b) The plot showing average SHG intensity measured in 3 identical arrays. The error bars show standard deviation in SHG intensities. The two shaded regions show the range of resonant disk sizes.

observe two major SHG intensity peaks, shown as shaded regions in Fig. 5.1(b), with the maximum SHG recorded for 175 nm and 400 nm disks.

To understand this size-dependent SHG intensity enhancement, we perform 3D finite-difference time-domain (FDTD) simulations using *Lumerical*. The excitation field was chosen to be a broadband plane wave with wavelengths from 750 to 850 nm. The excitation wave polarized along the x axis was launched from the air side. The 3D field monitors were positioned around the nanodisk to record the local field. The optical constants of GaP were taken from Palik et. al. [180].

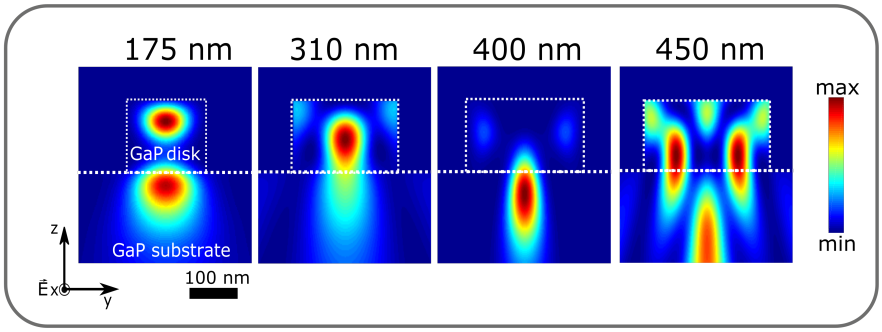

Figure 5.2: **Electric field distribution**. The vertical yz cross cut made along the diameter of disks, showing the spatial distribution of electric field intensity in the disk volume, for 3 disk sizes. The excitation field **E** is x-polarized (coming out of the plane of the paper).

In Fig. 5.2 we show the vertical crosscuts of calculated electric field intensity distribution at fundamental wavelength 800 nm in the disks along the geometrical yz plane. The disk and substrate regions are marked with dashed lines. It is clear that, a significant fraction of the electric field intensity distribution extends into the substrate. For some disk sizes, the intensity maximum is observed to be in a region deep in the substrate. The presence of the same material extends the nanodisk cavity. Since for the resonant disks the electric field distribution is negligibly low beyond 260 nm from the surface of the substrate, we only show the the results in this region.

From the simulated electric field intensity distribution, we can derive the electric energy density U_E, normalized to volume, defined as $U_E = \frac{\epsilon_r \epsilon_0}{2V} \int\int\int \mid \mathbf{E} \mid^2 dr^3$, where V is the volume of the nanodisk. In Fig. 5.3(a) we show the size dependent variation of U_E (red dashed line). We observe that the diameters corresponding to the maxima in energy density coincide with SHG intensity peaks from the experimental results shown in Fig.5.1. This shows that an efficient confinement of electric energy in the nanodisk volume is responsible for the enhancement of SHG in the nanodisks [169]. To identify the

effect of extended field in resonant enhancement, we also calculated U_E considering the extended volume into the substrate (upto 260 nm from the surface of the substrate) and find a similar trend (blue dashed line).

We now turn our attention to the effect of particle size on the scattering. To this end, we calculated the linear scattering cross sections at 800 nm of the nanodisks in the array. The result displayed in Fig. 5.3(b) shows that the total scattering cross section increases with the disk size. From the theory of Mie scattering, for particles of diameters similar to optical wavelengths, the scattering signal is proportional to the square of particle diameter. We confront our results with a calculated D^2 response (where D is the nanodisk diameter) which verifies the trend. The deviation from D^2 response clearly corresponds to the resonant disk sizes in the array.

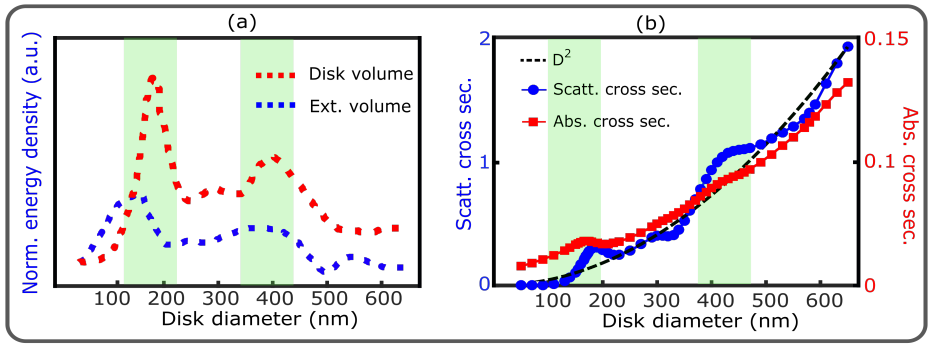

Figure 5.3: **Effective electric field enhancement** (a) The plot of electric energy density confined in the nanodisks (red dashed line) normalized to the corresponding volumes showing two peaks corresponding to the resonant disk sizes, denoted by the shaded region. Energy density confined in the extended volume (blue circles) shows a similar trend. (b) The linear scattering cross section (shown in blue circles) of the disks follows a D^2 trend (black dashed line). The disk sizes that deviate from D^2 correspond to the resonant disk sizes (green shaded region). Absorption cross section is shown in red squares.

Based on the observed SHG size-dependent enhancement and the

results from calculations, we conclude that, the concentration of electric energy density in the nanodisk volume of a high d_{eff} material, in combination with enhanced scattering cross section at fundamental frequencies result in the generation of SHG frequencies that resonate in the structure. To investigate the properties of SHG resonances, next we investigate the far-field radiation pattern of resonant nanodisks at SHG frequencies.

5.3 SHG angular emission pattern

To understand the role of various modes acting at the SHG frequencies, we analyse the far-field angular radiation pattern and its polarization state. Specific multipolar modes excited in a nanodisk antenna can be distinguished by their distinct radiation patterns, measured usually in the backfocal plane (BFP). In this type of imaging scheme, emitted radiation from a subwavelength light-emitting source before the lens is mapped onto its reciprocal k-space, in angular coordinates, on the BFP. This imaging method has helped to identify different radiation channels of nanoemitters [9, 190], to determine the orientation of single emitters [191], to analyse the emission characteristics due to coupling effects and to measure the directionality of emission of a nanostructure [192] and to quantify the contribution of multipoles in linear and nonlinear scattering [165, 193, 194].

First, we recorded the SHG BFP images of GaP nanodisks in reflection geometry, i.e., backward direction, and studied the dependence on disk size. For this, we modified the setup described in Chapter 1 such that the APD in the detection end is replaced by an emCCD camera and an additional lens to image the BFP. We know that the maximum detectable angle in measuring the radiation pattern of a nanoantenna is limited by the numerical aperture of the objective, described as $\theta_{max} = \sin^{-1}(\frac{NA}{n_2})$, where $n_2 = 1$ since we collect in the reflection geometry with an air objective of NA = 0.85. This

translates to an angular space with $\theta_{max} = 58.7^{o}$. Effectively, we collect all the emission wave vectors in the range $-0.85\frac{\omega}{c} \leqslant k \leqslant 0.85\frac{\omega}{c}$. The results are shown in Fig. 5.4. The images were acquired by setting an integration time of 400 ms and an electron-multiplying gain 200. The input polarization was set along the x axis and no polarization selection was made at the output. Each individual image corresponding to a specific disk in Fig.5.4 is the average of 100 such images accumulated. All the images are scaled to a maximum of 1.5 M counts. We also show below each individual pattern the angular emission in polar coordinates, through the x and y axis-cuts along the centre of each BFP pattern. In the polar plots, the angle θ denotes the angular spread in the xz-plane for x-cut intensity (red curve) and in the yz-plane for the y-cut intensity (blue curve). At the first glance, we note that, the overall intensity variation in the BFP images correlate strongly with that in the 2D scan image in Fig.5.1.

For the disk sizes 100 to 200 nm, the radiation pattern resemble a doughnut-like shape, with the SHG emission cut at the limit of NA, i.e., at 58.7^{o}. Thus the angular SHG emission maximum is beyond the collection limit of the NA of the objective used. Additionally, no SHG emission is observed in the normal backward direction, i.e., at the centre of all the patterns, there is zero intensity. This feature has been reported in the literature [195, 196] and was attributed to the symmetry properties of $\chi^{(2)}$ tensor and from the illumination axis being perpendicular to the substrate. As the diameter of the disk increases, apart from the intensity variation, for the disks 340 nm to 420 nm, the angular emission peaks at half (30^{o}) that for smaller disks, with the SHG intensity lobes now predominantly oriented along the y axis, i.e., $\perp$ the excitation polarization direction.

As described mathematically in [197], the angular distribution of light emitted by a dipole located on the interface of two homogeneous isotropic loss-free dielectric media depends on the refractive indices of both media. Since the density of available photonic modes is larger in a high index material, the dipole emitter couples light into the higher index medium with the higher probability of emission than into the

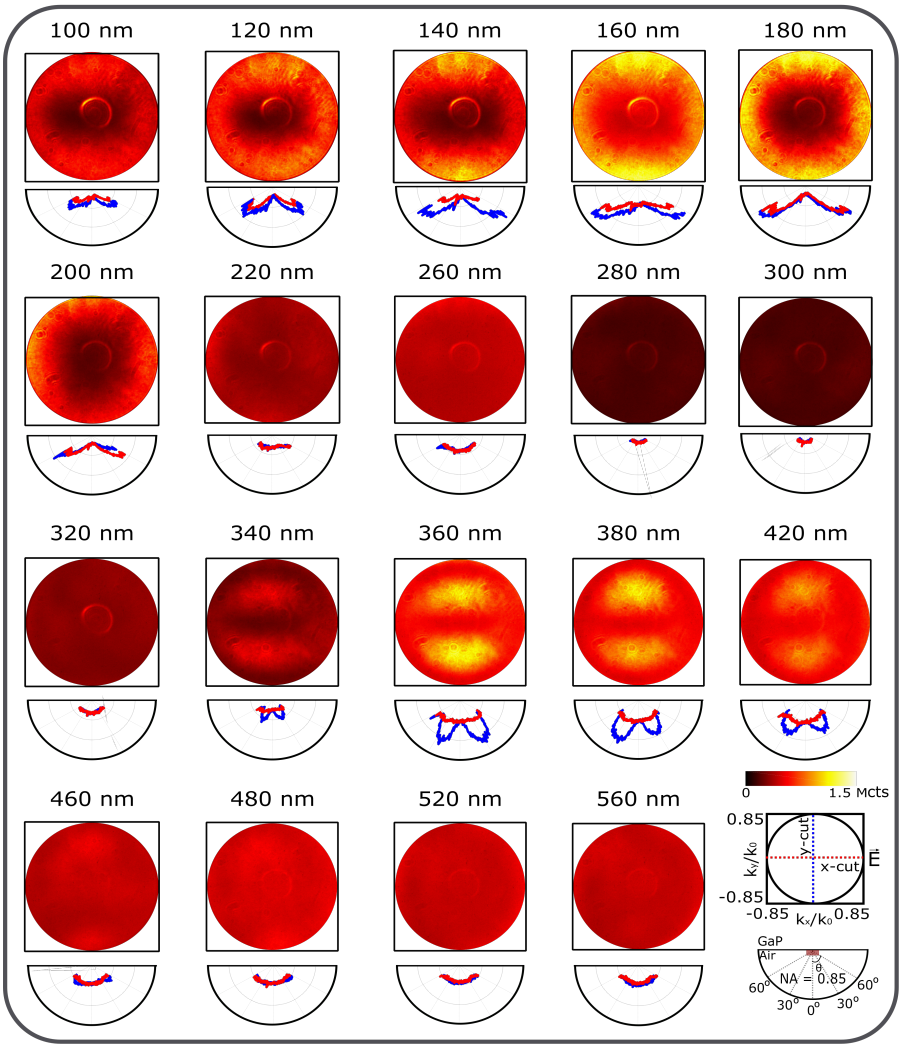

Figure 5.4: **SHG angular radiation pattern**. Backfocal plane SHG angular patterns of GaP nano disks as a function of diameter (indicated above each image), scaled to 1.5 M counts. The polar plots of x- and the y- cut intensities are also shown below each image. For small disks, the emission maximum occurs beyond the maximum collection angle of the NA. For big disks, emission maximum occurs at half the angle that of the small disks. The excitation laser is x-polarized.

medium with lower index. In an exemplary case, the radiated power of a z-oriented electric dipole lying on the surface of a medium with $n = 4$, as in our case, is mostly emitted (99%) in the denser medium at the critical angle and only 0.45% of the radiation is emitted to the air side. This means that, in our case, only a small fraction of the scattered SHG light is experimentally collected.

For a dipole oriented along the z- axis in an xyz coordinate system, the radiation pattern viewed from xy plane looks like a doughtnut-like shape. The intensity pattern measured for small disks, therefore suggests this either an electric or magnetic z-dipole. For bigger disks, the SHG intensity distribution that is oriented mostly along the direction $\perp$ input polarization, suggests higher order modes [198]. However, given that just a linear polarized NIR (or IR) laser excitation can generate both electric and magnetic multipole resonances in visible or UV spectral range in dielectric nanoparticles [199–201], a simple identification of the multipolar modes is not possible. Consequently, to determine precisely the types of the multipolar modes in the nanodisks and to obtain more insights on the SHG generation, we proceed with measuring polarization dependence of the angular emission pattern.

5.4 Polarization resolved radiation pattern

In this section, angular emission pattern imaging at the BFP is extended by polarization-sensitive detection. This technique, called Fourier polarimetry, based on Stokes analysis described in Chapter 1 for every angle in the radiation space of a nanoantenna [202–206], provides direct insight on the nanodisk response based on induced multipolar modes. In our experiments, we determine the angular Stokes parameters for SHG emission from the resonant GaP nanodisks. Combining Stokes analysis with SHG BFP imaging allows us to characterize the angular variation of polarization state of SHG emitted by a resonant GaP nanodisk.

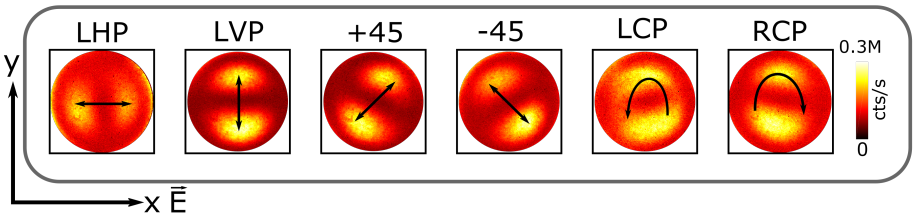

Figure 5.5: **Angular Stokes analysis**. The set of six BFP images of 420 nm disk measured with x-polarized excitation to determine angular Stokes parameters. The respective output polarizations are described with black arrows and on top of each image. The images are scaled to 1.3 M counts.

The Fig. 5.5 shows the set of six SHG BFP images measured for the 420 nm disk with excitation polarization set along the x axis with respective output polarization filters. The Stokes parameters can then be calculated using Eq. (2.17) - Eq. (2.20).

The retrieved angular Stokes parameters, normalized to S_0 for 120 nm (top panel) and 420 nm disks (bottom panel) are described in Fig. 5.6. In the top rows we show S_1, S_2 and S_3 and in the bottom rows ψ and χ. $-1 \leqslant S_1 \leqslant 1$ indicates the variation of polarization state from LVP to LHP, $-1 \leqslant S_2 \leqslant 1$ indicates the variation from -45° to +45° and $-1 \leqslant S_3 \leqslant 1$ indicates the variation from RCP to LCP respectively. For both disks, we see from S_1 and S_2 parameters that the orientation of polarization is mostly along the radial direction from the optical axis. For 120 nm disk, we find a superimposition of circular (as evident from the S_3 parameter) and radial polarized components. Looking at the S_3 component of 120 nm disk, we see that as we move from a fixed point and make a full 2π rotation, the handedness switches from RCP to LCP from one quarter to the other, however keeping the inclination along the radial direction. The difference between 120 nm and 420 nm disks in the S_3 component is clear: for 120 nm disk, at +45° angle we encounter RCP while for 420 nm disk we observe LCP. Although the magnitude of χ is similar for both disks, the handedness of circular polarization is the opposite. This is summarized in the S_0 map for both disks.

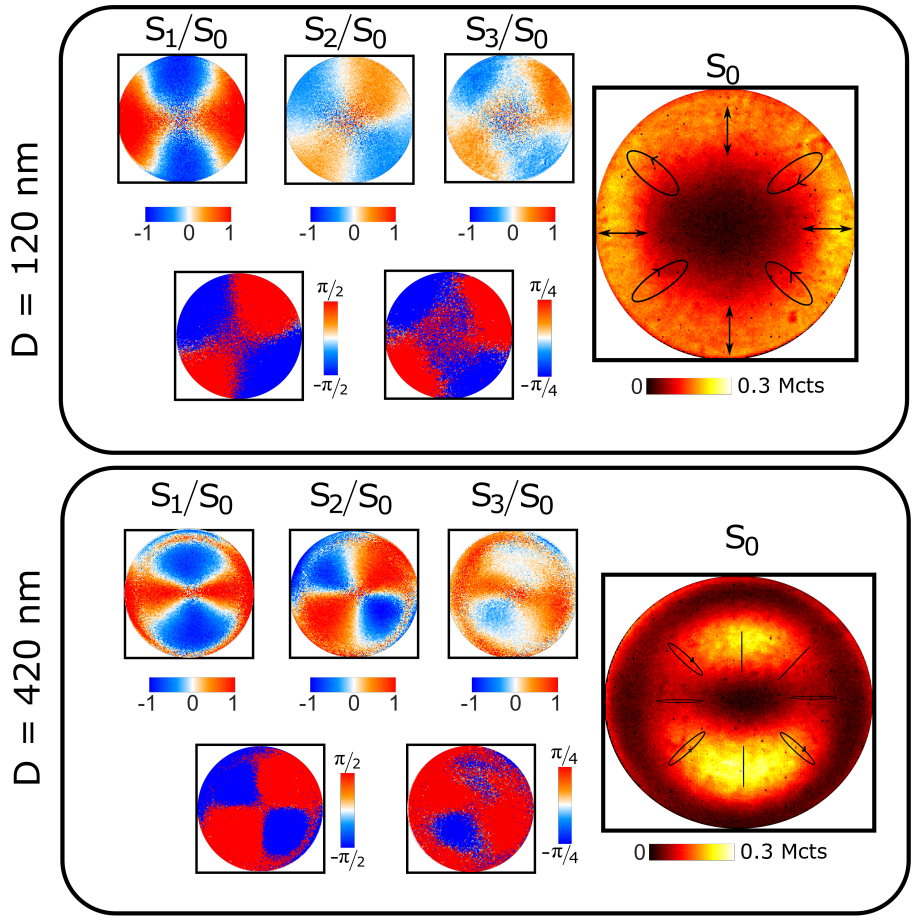

Figure 5.6: **Angular Stokes parameters of resonant GaP nanodisks**. Angular Stokes parameters S_1, S_2 and S_3 normalized to S_0 for 120 nm and 420 nm GaP nanodisks. For both disks, we observe dominant radial polarization components (S_1 and S_2) superimposed with circular polarization components (S_3) at 45° angles. Also shown are the ellipticity (ψ) and the inclination angle (χ) maps for both disks, in the bottom rows of respective panels.

Based on our observations so far, we conclude that a linearly polarized input beam generates a radially polarized vector beam with small circular components at the SH frequency (visible range) by interacting with a resonant, highly nonlinear GaP nanodisk. The

radially polarized SHG emission of 120 and 420 nm disk affirms the contribution of a dipole oriented $\perp$ xy plane. The small circular polarization components observed points toward the contribution of higher order multipolar modes. This is, to the best of our knowledge, first report of angular Stokes analysis of resonant SHG in the visible region. We attribute the slight nonuniformities in the circular and 45° polarization components in the polarization maps, to the errors in fixing the input polarization with respect to the crystalline axis in the experiments and in the nanofabrication. We note that our observations are similar to the recent studies that reported the polarization properties SHG from nanodisks of AlGaAs and GaAs [198, 207, 208], however in the IR and far-IR spectral ranges.

5.5 Multipolar decomposition

To understand the observations so far, we performed numerical calculations based on multipolar spectral decomposition. From the calculated electric field distribution $\mathbf{E}(\omega)$ at the fundamental frequency ω, we can determine the $\mathbf{P}(2\omega)$ using Eq. (5.1) by considering the specific components of $\chi^{(2)}$ interacting with that of the electric field. This depends on the orientation of crystal axis with respect to the excitation polarization as sketched in Fig. 5.7.

GaP has zincblende (normal cubic) crystal structure, which falls in the $\bar{4}$3m symmetry group. For such crystals, only 3 out of the 18 elements in the d_{il} matrix are non zero and $d_{14} = d_{25} = d_{36} = 70$ pm/V [209]. This means Eq. (2.13) reduces to:

$$\begin{bmatrix} P_{x'}(2\omega) \\ P_{y'}(2\omega) \\ P_{z'}(2\omega) \end{bmatrix} = \begin{bmatrix} 0 & 0 & 0 & d_{14} & 0 & 0 \\ 0 & 0 & 0 & 0 & d_{14} & 0 \\ 0 & 0 & 0 & 0 & 0 & d_{14} \end{bmatrix} \begin{bmatrix} E_{x'}(\omega)E_{x'}(\omega) \\ E_{y'}(\omega)E_{y'}(\omega) \\ E_{z'}(\omega)E_{z'}(\omega) \\ 2E_{y'}(\omega)E_{z'}(\omega) \\ 2E_{x'}(\omega)E_{z'}(\omega) \\ 2E_{x'}(\omega)E_{y'}(\omega) \end{bmatrix}. \quad (5.2)$$

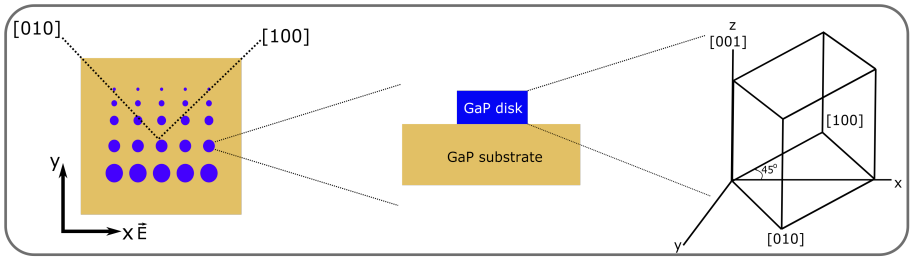

Figure 5.7: **Sample orientation**: The [100] grown GaP crystal sample was oriented in xy plane 45° rotated with respect to the x axis. The excitation polarization was set along X axis, with the beam propagating along the z axis (‖ [001] axis of the crystal).

where x', y' and z' form the principal-axis system of the crystal ([100], [010], [001]) and x, y and z form the global coordinate system. If the latter is rotated with respect to the former by an angle ϕ, we need to perform appropriate coordinate transformations, such that $\mathbf{E}(x', y', z') = T \times \mathbf{E}(x, y, z)$ to obtain the exact relations for $\mathbf{P}(2\omega)$:

$$P_x(2\omega) = 2\epsilon_0 d_{14}(E_y(\omega)E_z(\omega)\cos(2\phi) - E_x(\omega)E_z(\omega)\sin(2\phi)) \quad (5.3)$$

$$P_y(2\omega) = 2\epsilon_0 d_{14}(E_x(\omega)E_z(\omega)\cos(2\phi) + E_y(\omega)E_z(\omega)\sin(2\phi)) \quad (5.4)$$

$$P_z(2\omega) = 2\epsilon_0 d_{14}(E_x(\omega)\cos(\phi)+E_y(\omega)\sin(\phi))(E_y(\omega)\cos(\phi)-E_x(\omega)\sin(\phi)). \quad (5.5)$$

In our case, the crystal was cut along the [100] axis and the excitation field $\mathbf{E}(\omega)$ was propagating along the [001] axis (parallel to the out-of-plane z axis). The disk was rotated in xy plane by 45°, i.e., the [100] axis is along a line 45° inclined to the x axis of the global coordinate system ($\phi = 45°$) as shown in a schematic diagram in Fig. 5.7.

Next we determine the multipolar content of this generated SHG polarization $\mathbf{P}(2\omega)$. To this end, we calculate the contributions of various multipole moments upto the third order: dipoles $\mathbf{p}$ (electric) and $\mathbf{m}$ (magnetic), quadrupoles $\hat{Q}^e$ (electric) and $\hat{Q}^m$ (magnetic),

Octupole $\hat{O}^e$ (electric) in $\mathbf{P}(2\omega)$ based on the formalism described in Evlyukhin et. al. [210, 211]:

$$\mathbf{p} = \int \mathbf{P}(\mathbf{r}) d\mathbf{r} \tag{5.6}$$

$$\mathbf{m} = -\frac{i\omega}{2} \int [\mathbf{r} \times \mathbf{P}(\mathbf{r})] d\mathbf{r} \tag{5.7}$$

$$\hat{Q}^e = 3 \int [\mathbf{r}\mathbf{P}(\mathbf{r}) + \mathbf{P}(\mathbf{r})\mathbf{r} - \frac{2}{3}[\mathbf{r}.\mathbf{P}(\mathbf{r})]U] d\mathbf{r} \tag{5.8}$$

$$\hat{Q}^m = \frac{\omega}{3i} \int ([\mathbf{r} \times \mathbf{P}(\mathbf{r})]r + r[\mathbf{r} \times \mathbf{P}(\mathbf{r})]) d\mathbf{r}. \tag{5.9}$$

$$\hat{O}^e = \int \mathbf{P}(\mathbf{r})\mathbf{r}\mathbf{r} + \mathbf{r}\mathbf{P}(\mathbf{r})\mathbf{r} + \mathbf{r}\mathbf{r}\mathbf{P}(\mathbf{r}) d\mathbf{r}. \tag{5.10}$$

These induced multipole moments drive multipolar modes at SH frequencies that radiate to free space in their characteristic pattern. We then calculate the far-field scattered power emitted by individual multipole moments [210]:

$$P_{sca} = \frac{k_0^4}{12\pi\epsilon_0^2 v_d \mu_0} \mid \mathbf{p} \mid^2 + \frac{k_0^4}{12\pi\epsilon_0 v_d} \mid \mathbf{m} \mid^2 + \frac{k_0^6}{1440\pi\epsilon_0^2 v_d \mu_0} \sum_{\alpha,\beta} \mid \hat{Q}^e_{\alpha\beta} \mid^2 + \frac{k_0^6 \epsilon_d}{160\pi\epsilon_0^2 v_d} \sum_{\alpha,\beta} \mid \hat{Q}^m_{\alpha\beta} \mid^2 + \frac{k_0^8 \epsilon_d^2}{3780\pi\epsilon_0^2 v_d \mu_0} \sum_{\alpha,\beta,\gamma} \mid \hat{O}^e_{\alpha\beta\gamma} \mid^2 \tag{5.11}$$

where $k_0 = \frac{2\pi}{\lambda}$ is the wave vector in vacuum, ϵ_0 is the vacuum permittivity, v_d is the velocity of light in the medium (here taken as air) and μ_0 is the vacuum permeability. In Fig. 5.8 we describe the results of multipolar decomposition upto octupolar terms for nanodisk diameters from 50 nm to 650 nm.

Analysing the dipolar contribution, we find from Fig. 5.8 that for the resonant 180 nm and 400 nm disks, SHG is dominated by the z-oriented electric dipole p_z. The radiated power of y-oriented magnetic dipole m_y is negligible compared to that of p_z, hence we neglect its contribution.

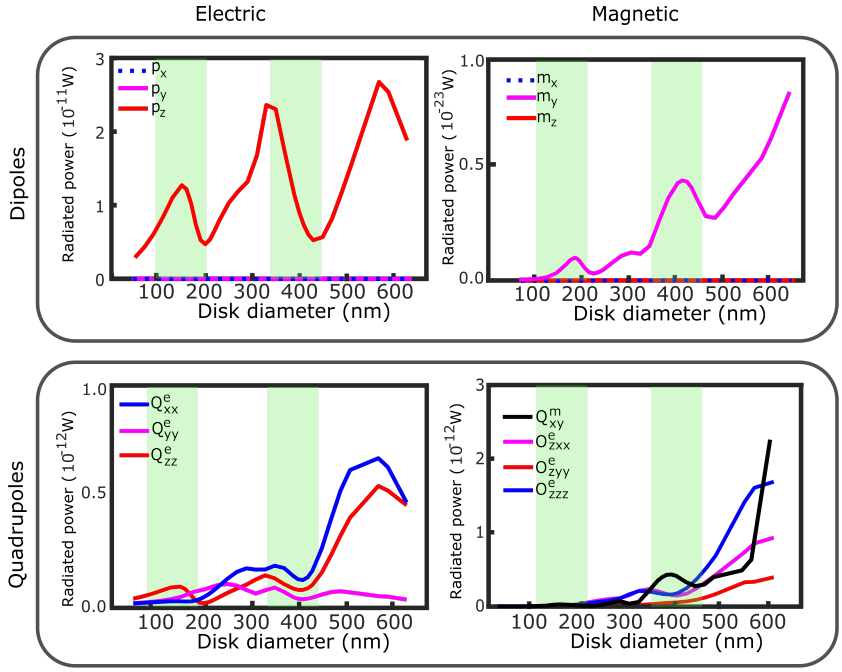

Figure 5.8: **Dominant multipolar modes radiating at SH frequencies**: Multipolar modal analysis for GaP nanodisks at 400 nm show that for smaller disks, z-electric dipole is the prominant radiating mode. For bigger disks, there are additional contributions from magnetic and electric quadrupoles along with electric octupoles.

Regarding quadrupoles, we observe the contribution of Q^e_{xx}, Q^e_{yy} and Q^e_{zz}, in addition to that of magnetic quadrupole Q^m_{xy}. For 180 nm disk, Q^e_{zz} is dominant over Q^m_{xy}, however, for 400 nm disk, Q^m_{xy} is dominant. The magnitude of electric quadrupoles are weaker compared to that of p_z for smaller disks, while for bigger ones, dipolar and quadrupolar components compete in strengths.

Additionally, we also notice weak contribution from octupolar modes, as shown in the bottom right panel of Fig. 5.8, where we only show O^e_{zxx}, O^e_{zyy} and O^e_{zzz}. We note that Q^e_{zz} and O^e_{zzz} contribute to the radial polarization.

Next, we look to the calculated radiation patterns of these dominant multipolar modes. Based on the method described by Grahn

Multipolar mode	Reflected intensity (%)
p_z	0.45
Q_{zz}	0.052
Q_{xx}	0.006
Q_{xy}	0.025
O_{zzz}	0.002
O_{zxx}	0.003
O_{zyy}	0.2

Table 5.1: The calculated percentage of radiated intensity in reflection direction for different multipolar modes.

et. al. [211], we use the recorded scattered fields to derive the multipole coefficients upto electric octupoles. The radiation patterns of multipoles near a dielectric interface can then be calculated using the angular spectrum representation based on vector spherical harmonics discussed in Inoue at. al. [212]. Propagating and evanescent fields are reflected and refracted using the Fresnel coefficients of GaP-air interface.

In Fig. 5.9 we show backfocal plane radiation patterns towards the reflected, low index side (identical to the experimental conditions) of the multipolar modes along with the polar plots of x-cut, both in the low index (blue curve) and in the high index (red curve) directions. We notice that most of the radiation is emitted to the high index side. Also, the effect of high index substrate is clearly visible in the extreme-narrowing of the intensity lobes for p_z and Q^m_{xy}. By integrating the images we obtain the calculated intensity ratio between the transmitted (high index) and the reflected (low index) directions. In Table 5.1 we show the result.

On comparison, we see that the calculated radiation pattern of p_z correlates well with the observed radiation pattern for the 180 nm disk. For 380 nm disk, we note that the contribution of Q^e_{zz} and O_{zzz} results in the bending of the intensity lobes to smaller angle.

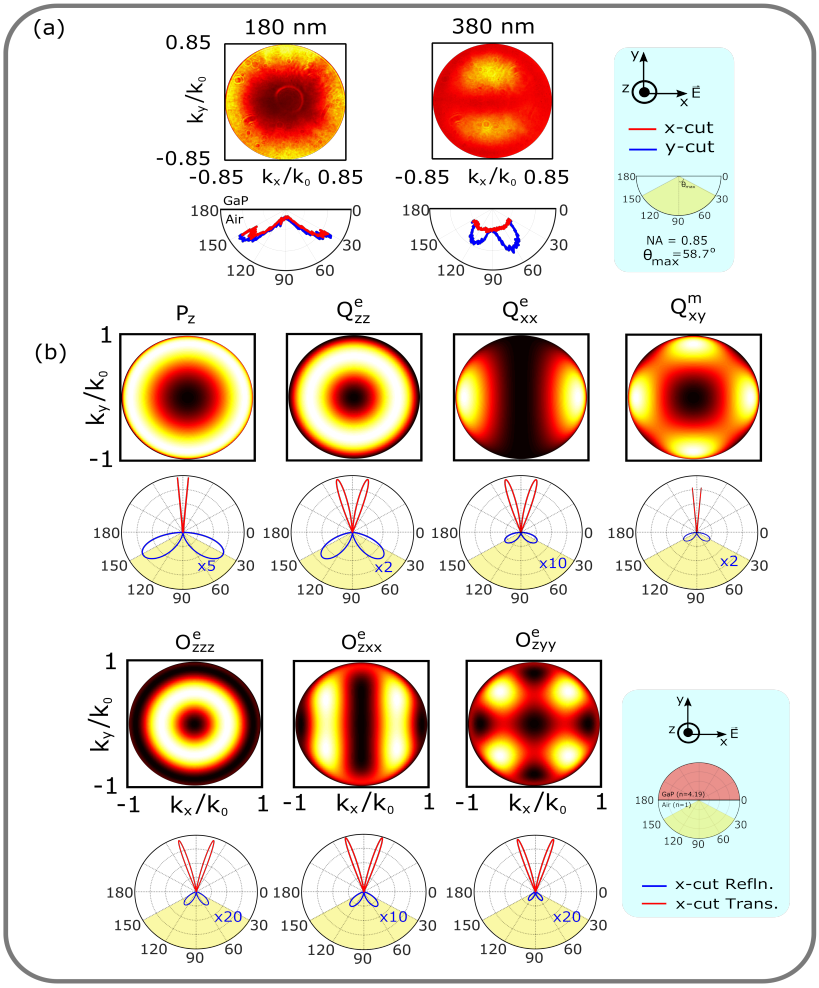

Figure 5.9: **Multipolar radiation pattern**: (a) Measured angular SHG radiation patterns and the polar plots of x-cut (red curve) and y-cut (blue curve) intensities. (b) Calculated radiation patterns at 400 nm in reflection with corresponding polar plots. Polar plots show the intensities in both the reflection (blue curve) and the transmission (red curve) directions. Yellow shaded region shows the experimentally accessible angular range. In panel (b), intensities in reflection are scaled (blue curve) by numbers shown alongside. The inset in panel (b) shows the schematic representation of the dominant multipolar modes.

5.6 Discussion

By confronting the experimental observations from backfocal plane imaging in Section 2 and Stokes analyis in Section 3 with the calculated multipolar decomposition and far-field radiation patterns, we arrive at following impressions:

- Doughnut-like far-field radiation pattern of all the disks with radially polarized components can be explained as the contribution of p_z, Q^e_{zz} and O_{zzz}. The radially polarized components also rule out the effect of m_y.

- The reduction in angular spread of intensity in the radiation pattern of bigger disks is the contribution of higher order multipoles Q_{xx} and O_{zxx}. Of particular interest is to note the contribution of O_{zyy} mode, which has intensity in 45° directions. Circularly polarized components in the SHG radiation pattern of similar materials have been attributed to octupolar modes in previous works [198, 207, 208].

- For bigger disks, predominant intensity distribution along the Y-direction is a consequence of Q_{xy} contribution.

- From the multipolar decomposition, the radiated power of higher order multipoles significantly weak compared to that of p_z, however, their effect is non-negligible, as proven by Stokes analysis.

- The slight mismatch between experiments and calculations in our case could be attributed to several factors: multipolar decomposition considers a point-like source at the interface of the particle. However, we note that, the effective optical wavelength is much smaller than the disk diameters in our array, especially for bigger disks. Also, the nanodisk cavity resonator in our case extends indefinitely into the substrate which imposes computational limitations for multipolar decomposition analysis. Additionally, our numerical simulations also considers GaP

to be isotropic, which, in reality is not. Fabrication anomalies of the nanodisks on which we performed the experiments, can also contribute to this.

5.7 Conclusions

In summary,the mechanisms of SHG emission in resonant GaP nanodisks was studied in detail, attributing the size-dependent enhancement in SHG intensity to the concentration of electric field energy density in the disk volume. To further analyse the radiating properties of enhanced SHG scattering in the far field, polarization-resolved BFP imaging with Stokes formalism was performed, and we identified the generation of radially polarized vector beams with small circular components at SH frequencies in the visible range. Following the multipolar decomposition at 400 nm, this observation was attributerd to the strong contribution from z-oriented electric dipole and weak contribution from electric and magnetic quadrupoles and electric octupoles. We compared the experimentally observed radiation pattern to the calculated ones and observe a good agreement between both.

6

Phase control of multipolar interferences

In Chapter 5 it was shown that, the concentration of electromagnetic energy in GaP nanodisks results in the enhancement of SHG. The multipolar modes in the resonant nanodisks were determined through a systematic Stokes polarimetry in the angular space and the observations were explained with multipolar decomposition. Spectrally separated multipolar electromagnetic modes that resonate with relative phases in a nanodisk volume, following a broadband laser illumination result in multipolar interferences. Such interferences can be manipulated by means of spectral phase modulation of the broadband excitation field to achieve a radiation pattern withon coherent control of the radiation pattern of a nanoantenna with polarization readout. Based on the multipolar decomposition at fundamental frequency range, we discuss our results.

6.1 Introduction

The SHG spectrum of a nanoparticle depends on the resonance of the nanoparticle with the excitation laser spectrum. A nanoparticle that is non-resonant (e.g.: $BaTiO_3$) with the excitation laser field has a spectrally flat phase response and hence cannot be influenced the phase of laser field. In the work of Accanto et. al., [151] it was shown that the intrinsic phase response of a Ag nanoantenna can chirp the spectral phase. Such a plasmonic nanoantenna can be considered as a pure Lorentzian harmonic oscillator with a well known phase response. Based on this assumption, the intrinsic phase response can be quite accurately derived from an experimental SHG MIIPS spectrogram of this antenna. On the other hand, in a dielectric nanoresonator, as shown in Chapters 4 and 5, several overlapping elecromagnetic multipolar modes, in both fundamental and second harmonic spectral domains, that interfere with each other based on their respective phase responses, create a non-trivial phase profile that is not easy to assume beforehand. In this Chapter, we present our first results of the investigation of phase response of a resonant GaP nanodisk, controlling the multipolar interferences in such a system.

6.2 Spectral phase response of a GaP nanodisk

Let us consider the spectral SHG response of GaP nanodisk as a function of size. The SHG scan image of the nanodisk array discussed in Chapters 4 and 5 is reproduced in Fig. 6.1 (a). In (b) we show the measured SHG spectra of 14 disks from the array, compared to the one of the bulk (measured on the substrate). We notice that firstly, for small disks, the SHG spectrum shows a gradual red shift as the diameter increases. As the disk size further increases, at the onset

of the second resonance, the spectrum peaks again at shorter wavelength and gradually shifts to longer wavelengths. This demonstrates different multipolar modes responsible for SHG enhancement in the disks as expected [213]. Secondly, the width of the SHG spectra of smaller disks are narrower than that of bigger disks, when compared to the non-resonant bulk. This is due to the fact that there are multiple modes responsible for SHG enhancement for bigger disk sizes.

To appreciate the antenna phase response in SHG, MIIPS scans were performed, on the two resonant disk sizes 120 and 420 nm, and were compared to that of bulk GaP substrate. Results shown in Fig. 6.2 correspond to (a) bulk compared to (b) 120 nm disk and (c) 420 nm disk. It is clear that in (b) and (c) a reduced spread of SHG intensity maxima in the wavelength axis is observed, which corresponds to the spectral narrowing due to the resonance. Additionally, the regions of maximum SHG intensity shifts in the wavelength axis, correlating with the shift in the line spectra in Fig. 6.2 (b). It can also be noticed that the lines corresponding to the SHG intensity maxima show more spread in the δ axis, which directly relates to the chirping of the spectral phase [151]. To make this more obvious, in (d) a contour plot of intensities are shown. It is important to note that the intensity of 120 nm disk points downwards, to the short wavelength side, and that of 420 nm disk the other way (see the arrows with respective colours). In the bluer side of SHG spectrum, there is a considerable overlap between the bulk and the 420 nm spectra. Similar to the observations in Ag nanoantennas reported by Accanto et. al., [151], the lines of maximum SHG intensity for both 120 and 420 nm disks show slightly asymmetric tilt: for 120 nm disk (in (b)), the line of maximum intensity in the first half of 0 to π radians is broader and slightly tilted in clockwise direction, while that in the second half of π to 2π is tilted in the anticlockwise direction and for 420 nm disk, in (c), it can be noted that the intensity line points toward the long wavelength direction, with the tilt in the first and second halves slightly asymmetric with respect to each other, which

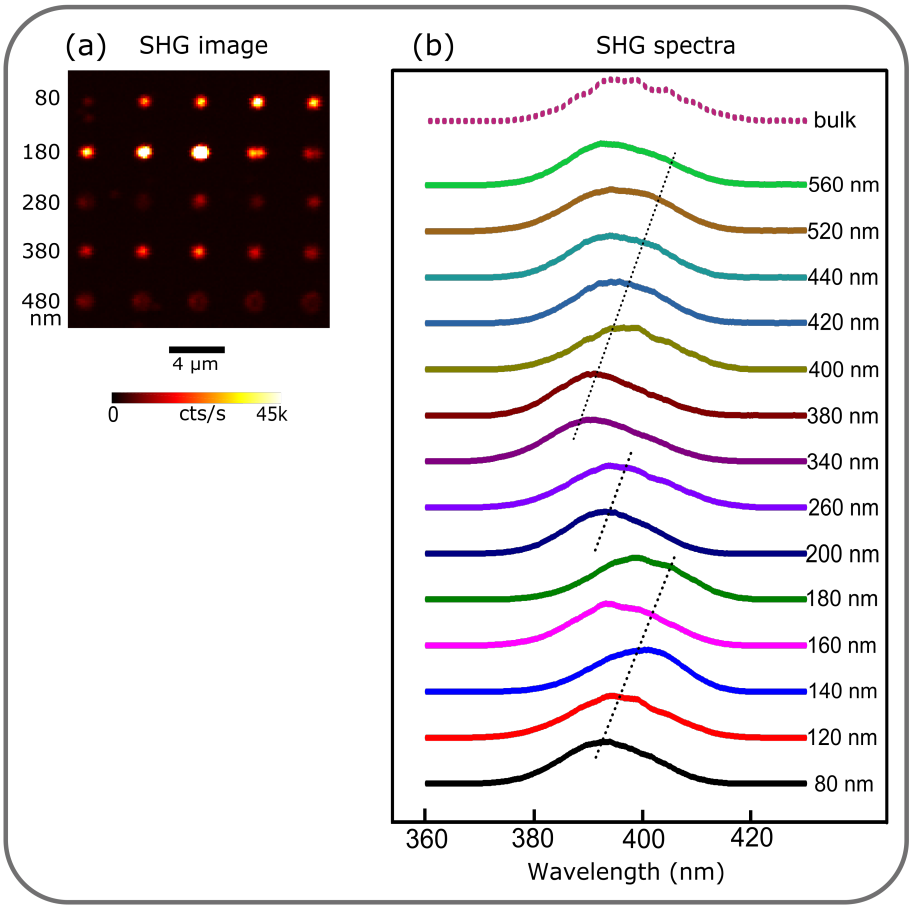

Figure 6.1: **Evolution of SHG spectra with the disk diameter**: (a) The SHG scan image of the GaP nanodisk array showing size-dependent SHG resonances. (b) SHG spectra measured for selected disk sizes compared to that of bulk GaP shows evidence for multiple resonances, as the spectra shift to longer wavelengths with increasing size. When a higher order resonance kicks in, the spectrum peaks at shorter wavelengths and gradually shifts to longer wavelengths.

is the evidence of phase response. In (d) we show this trend with arrows and the tilt angle marked for respective disks.

To model a response for this effect is not straightforward due to the lack of sufficient knowledge on the resonant multipolar modes at the fundamental frequencies and their phases. Instead, a simple, tested phase control method is employed to control their interferences: the π phase step. In doing so, the polarization state in the SHG BFP is chosen as the output readout, since the latter has been demonstrated in Chapter 5 to be a sensitive technique to carry the signature responses of specific multipolar modes. In other words, we look to manipulate the SHG vectorial angular emission pattern of resonant nanodisks following spectral phase modulation, such as the π phase and its variants.

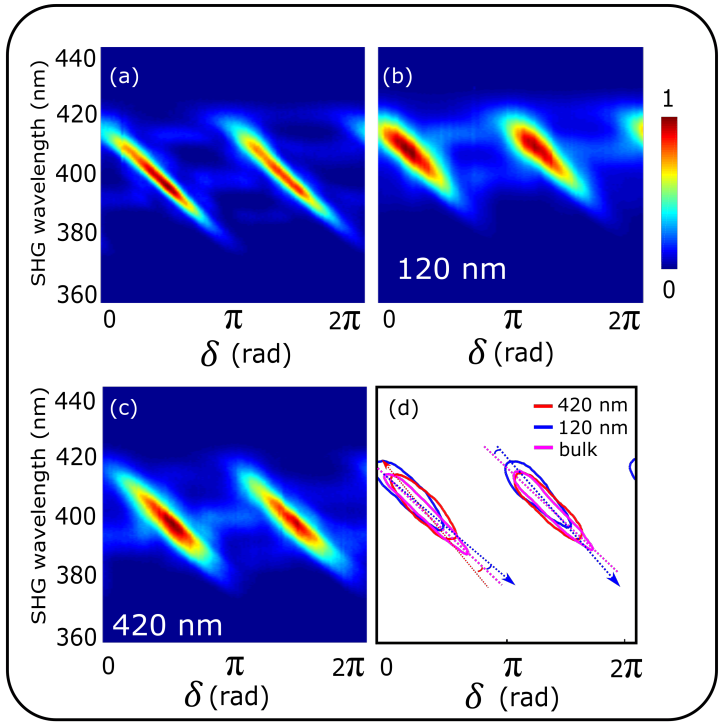

Figure 6.2: **Resonance phase effect**: The SHG MIIPS spectrogram measured on (a) bulk GaP (b) 120 nm disk (c) 420 nm disk (d) contour plot of (a), (b) and (c) overlaid on top of each other. From (b) and (c) it is clear that the spectrogram lines point towards shorter and longer wavelengths respectively, for 120 nm and 420 nm disks, indicating their resonance shifts. The magenta dotted line shows the intensity maximum for the bulk GaP, set as a reference. The blue dotted line shows the tilted intensity maximum for 120 nm disk while its arrow points intensity towards the shorter wavelengths, indicating a resonance shift towards longer wavelengths. Note that the line tilts in both halves of the spectrogram are in opposite directions. For 420 nm disk, the red dotted line shows the tilt with respect to the bulk intensity maximum. The red line is seen tilted in the opposite direction to that of the blue line. Also, the spread of the intensity maxima in the δ axis suggests of the chirped spectral phase. The narrowing in the wavelength axis is a resonance-effect.

6.3 Controlling the vectorial radiation pattern

In section 3 of Chapter 5 it was asserted that the radiation pattern is one of the most important characteristic of a nanoantenna. Dielectric nanoantennas are known to demonstrate excellent directionality [214, 215]. Controlling the angular spread of an antenna radiation is fundamental for chemical and biosensing applications [216]. The idea of shaping the radiation pattern of nanoantennas started with the proposal of Kerker in his seminal paper [217], which identified for the first time that, a dipolar nanoantenna with equal strengths of electric and magnetic modes, both in amplitude and phase, exhibits zero backward scattering due to interferences, which then followed few experimental demonstrations of the concept [158, 193, 218–223]. This condition can be extended and generalised for any multipolar interferences [193, 224].

From a microscopic point of view, the interference of dipole and quadrupole sources within a nanoantenna can influence the SHG efficiency [225]. Recently, Olivier Martin and coworkers showed a possibility to tune the SHG radiation pattern of a nanorod antenna by tuning the excitation wavelength simply because the linear phase of a nanoantenna change with respect to wavelength. By doing so, the directionality of SHG emission can be flipped [226], due to the interference of dipolar and quadrupolar modes. For a wavelength shorter than the resonant wavelength, both of these modes are in-phase and for longer wavelength beyond the resonance, they are out of phase. Consequently, the radiation pattern gets modified. However, metallic nanoantennas have broad resonances and offer limited scope for interferences within the laser spectral range. Recently, in dielectric nanoantennas, controlling the radiation pattern has also been realised by changing the angle of incidence, the state of polarization of the incident light [194], or even tuning the antenna geometry [158] etc. In the work of De Angelis et al [194], it was shown that the control of

radiation pattern can be achieved by manipulating the modal interference in an AlGaAs nanodisk, by controlling the angle of incidence, excitation polarization and the geometry. However, in our case, contrary to these works, the excitation pulses are broadband, meaning that multiple resonant modes can be simultaneously excited by different parts of the laser spectrum, and corresponding sum-frequency interferences can be controlled in the second-harmonic frequency domain, thus achieving a true all-optical spectral interference, freeing us from experimental modifications.

To this end, the proposed approach is straightforward, combining multi-layers of excitation and detection schemes: to control the multipolar interferences by spectral phase manipulation of the excitation laser pulses and achieve directionality of the radiation. Since the spectral phase control requires no additional modification of the setup described in Chapter 2, the experiment is quite straightforward. It was shown in section 5.4 that polarization resolved angular SHG radiation pattern provides rich information on the multipolar modes resonating in the GaP nanodisk. Therefore, the SHG angular Stokes parameters are measured to analyse the effect of spectral phase control of excitation pulses. In Fig. 6.3 a sketch explaining the concept of the proposed experiment is described.

To illustrate the idea, let us consider a GaP sphere in free space, with 260 nm diameter. The calculated antenna scattering spectra upto dipolar modes show electric and magnetic dipolar modes spectrally separated, but having a considerable overlap in the wavelength range around 800 nm (Fig. 6.3, top left). The respective phases are also shown alongside (top right). Initially, this nanoparticle is excited with laser pulses having a flat (i.e., relative phase between all the frequency pairs is zero) spectral phase. This is ensured by pulse compression described in Chapter 2. Next, the angular Stokes parameters are determined to identify the polarization state of the emitted SHG, using the method described in Chapter 5. To control the multipolar modal interference, the antisymmetric π step spectral phase is added on the laser spectrum such that the two resonant modes are

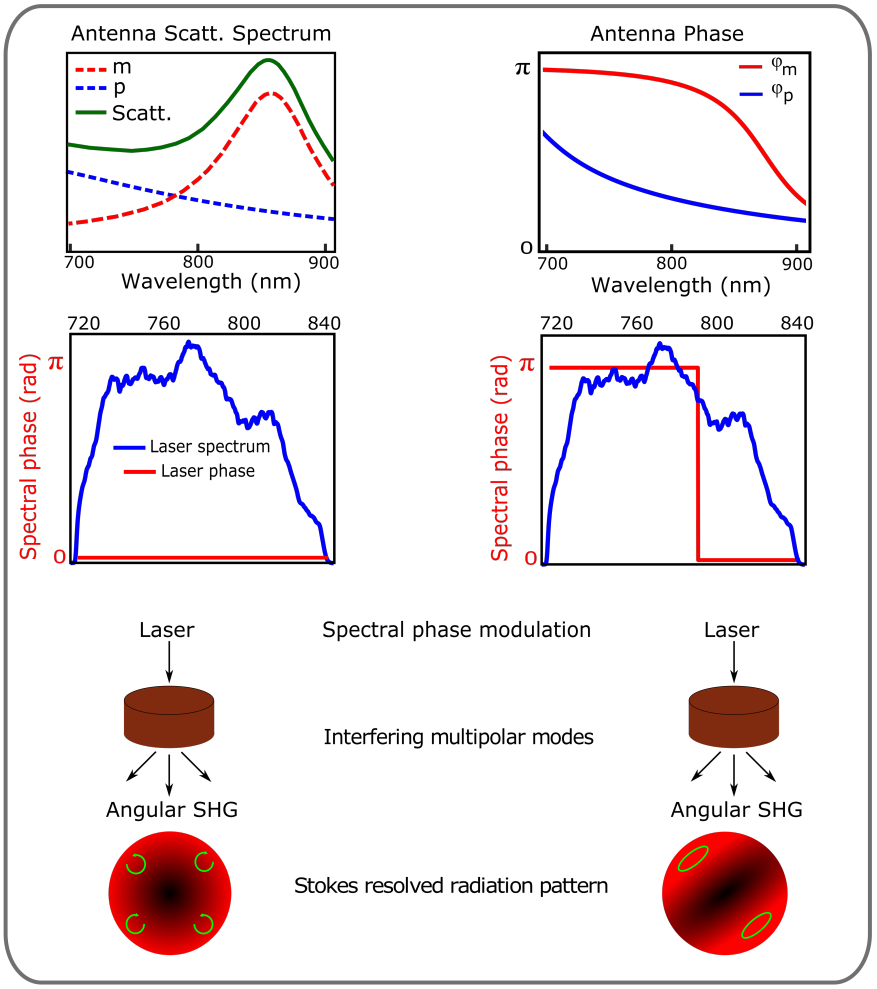

Figure 6.3: **Concept of spectral phase control of angular polarization state**. Considering a GaP sphere in free space having two resonant modes (red and blue dashed lines, respectively denoting magnetic and electric dipolar modes, total scattering cross section shown in green line) in the laser spectral range. Antenna spectral phases (red line shows the phase of magnetic dipole and blue line shows the phase of electric dipole). Next, Stokes-resolved SHG angular radiation pattern is measured at the BFP. Then, a π step spectral phase is added on the laser spectrum such that resonant modes are driven π out of phase and the measurement is repeated. Interference of the resonant multipolar modes will result in a change of polarization state of the radiation pattern.

π out of phase. Since they are driven out of phase with each other, they destructively interfere, meaning that the sum-frequency pairs around 800 nm (where the modal overlap occurs) that generate SHG will interfere destructively, resulting in SHG with a different polarization state. Thus, by tailoring the spectral phase of the excitation laser spectrum, the control of the multipolar modal interferences is achieved, having the angular Stokes parameters as the readout.

6.4 Spectral phase control of angular polarization state

For the phase control experiment, four different phases were employed. In Fig. 6.4, the four panels (a), (b), (c) and (d) correspond to four different spectral phases applied on the excitation laser pulses. In each of those panels we show the measured angular Stokes parameters S_1, S_2 and S_3, normalized to S_0, for both resonant disks 120 nm and 420 nm. Since S_0 can be determined by adding either the images measured for LHP and LVP, the +45° and the -45° polarizations or for LCP and RCP. We have noted that angular intensity varied with respect to polarization state and therefore for the normalization, the average S_0 calculated from the three cases were used. The panel (a) corresponds to the flat spectral phase, the panel (b) the antisymmetric π step phase, (c) the 5-segment π step phase and (d) shows the notch-type π step phase. The top row in each panel shows the laser spectrum (blue curve) together with the applied spectral phase (red curve). Alongside the laser spectrum, the calculated SHG spectra resulting from each applied spectral phase is also shown. The 5-segment π step phase is designed such that 640 pixels of the SLM is divided into 5 identical segments (i.e., 128 pixels for each segment) with the phases in successive segments having π phase difference. A higher order, asymmetric (i.e., more segments of 0-π phase switching, with segments not identical in width of pixels) version of this phase step was employed for generating several narrow SHG spectra

from a broad spectrum in the work of Dantus and coworkers [227]. The notch-type π step phase also generates a narrow SHG spectrum, but unlike the 5-segment π step phase, the amplitude is lower, with less number of peak (in this case, since it is applied at the central frequency of the laser spectrum, there is only one peak). As can be seen, SHG spectrum gets modified with an applied phase (see Chapter 2), with the peak intensity changing to specific SHG wavelengths depending on the wavelength where the phase step is applied on the laser spectrum, which allows to address specific multipolar mode in a given frequency range.

The experiment is performed by measuring the angular BFP images for each applied spectral phase, with the respective combination of polarizing elements in front of emCCD camera (see)Chapter 5. The measured SHG signal varies with respect to the detected polarization state, and also with the different spectral phases applied. For instance, since the spectral phases applied here are the different variations of the π step phase, interferences between various sum-frequency pathways result in a reduction in SHG signal (see Chapter 2 and Chapter 3)). Theoretically, with the antisymmetric π step phase, the SHG intensity drops to the level of 40% from that when the spectral phase is flat. For 5-segment π step phase, SHG signal drops to 33% and for notch type π step phase, it drops to 27%. This drop in overall SHG signal intensity can be appreciated from the measured S_0 images shown in the bottom-most row in Fig. 6.4. The integrated amplitude of S_0 from the measured images in (a) to (d) is found to drop in the same manner. Each image for a particular spectral phase at the excitation and the output polarization was measured by an acquisition time of 800 ms, with 200 EM gain and was averaged for 100 accumulations. This long exposure of the emCCD pixel array creates a background noise level that is higher than the maximum SHG signal measured. For instance, for 120 nm disk, the background noise level for LHP and LVP polarization states were 3.2×10^5 and 2.8×10^5 cts respectively, while the maximum signal measured were 2.5×10^5 and 1.5×10^5 cts on top of the background noise level.

Thus, to avoid errors, it was ensured that a 2D plane of background noise (which varied depending on the detected polarization state and the applied spectral phase) was subtracted from each of the 24 images measured (6 images for Stokes analysis for one spectral phase, 4 spectral phases require 24 BFP images to be measured).

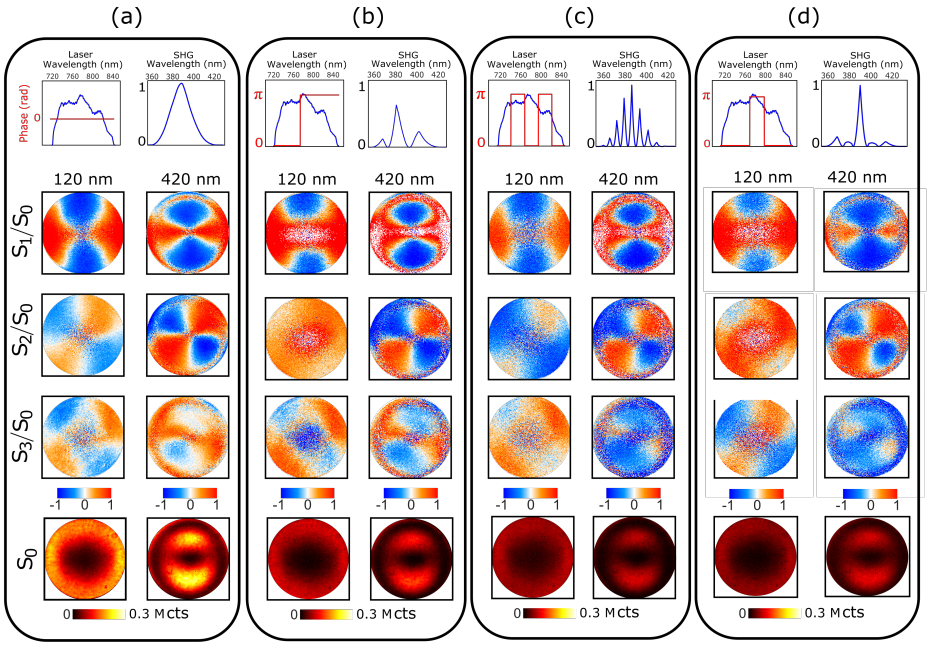

Figure 6.4: **Spectral phase control of angular polarization states**: (a) Measured angular Stokes parameters S_1, S_2 and S_3, normalized to S_0, for flat spectral phase (b) for antisymmetric π step phase and (c) for 5-segment π step phase for 120 and 420 nm disks. Top row shows the laser spectra (blue curve) with the applied spectral phase (red curve) and the corresponding SHG spectra to its right side, normalized unity. SHG intensity maps (S_0) are shown in the bottom row.

The angular Stokes parameters measured for different applied spectral phases, in general show features that are consistent. Firstly, the S_1 parameter shows the angular distribution of x-y polarization components, which for 120 nm disk is slightly more x-component

than the y component. On the contrary, for 420 nm disk, in general, y-component dominates the angular space than the x-component. The S_2 parameter is nearly symmetrically distributed in the angular space for 420 nm disk, and more amplitude is observed for +45° polarization components compared to that for 120 nm disk, which has slightly asymmetric distribution of +45° and -45° components in the angular space. The S_3 parameter shows a slightly more symmetric distribution for 120 nm disk while for 420 nm disk it appears to be mixed and random in the angular space. It is interesting to note that, except for S_1, S_2 and S_3 parameters measured for flat spectral phase, due to low-light level, following the normalization with S_0 (which is also low), some points in the angular space show amplitudes >1 or <1, which is forced to be 0 during the analysis. This is the reason of white points mostly in the middle of the images, and around the circumference.

Following the application of different applied spectral phases, for 120 nm disk, the S_1 parameter shows almost no variation with respect to the applied spectral phases, while the S_2 component shows switching in polarization state while going from a flat spectral phase through different π phase steps (see the corresponding columns of 120 nm in panels (a), (b) and (c)). While going from flat spectral phase (a) to the antisymmetric π step phase in (b), it is clear from the S_2 image, that the -45° polarization components has become weaker. Effectively, for this spectral phase, the SHG polarization state is mostly of +45° polarization state. When going from (a) to (c), it is observed that the polarization state is mainly -45°, for the same disk. As to the notch π step phase, it resulted in slightly diminishing the linear diagonal polarization state, with a slight bias towards +45°. On the other hand, the S_3 component, when going from (a) to (b) to (c) to (d), only a minor change is observed. i.e., the antisymmetric π step phase, the 5-segment π step phase, nor the notch π phase did not result in a notable switching in the circular polarization state.

For 420 nm disk, the S_1 and S_2 parameters exhibit negligible change for all the applied phases, while S_3 component shows that

measured SHG has a little bias towards RCP state. Therefore, from first impressions, it is clear that we are only able to influence the polarization state of the SHG far-field emission of 45° components for 120 nm resonant nanodisk.

To quantify the effect of phase control, in Fig 6.5, the change in Stokes parameters S_0, S_1, S_2 and S_3, in the BFP with respect to the azimuth angle ϕ is plotted for 120 nm and 420 nm disks respectively for all three phases: the flat (zero) phase, the antisymmetric π-step phase and the 5-segment π-step phase. The line plots were generated by calculating the average of respective angular parameters in an annular region of 6 pixels selected near the polar angle of maximum contrast obtained in the angular Stokes images.

From Fig. 6.5, red curves show the angular variation of S_0, S_1, S_2 and S_3 for flat spectral phase, green curves show the variation for antisymmetric π step phase, blue curves show that for 5-segment π step phase and magenta curves for the notch-type π step phase. The 4 panels on the first column show the results for 120 nm disk and the ones on the second column show the results for 420 nm disk. The first row shows the variation in S_0, the second one S_1, third one S_2 and finally the fourth one that of S_3. The 0 levels are marked with grey dotted line in each panel.

Looking at the first row, all the curves nicely overlap with each other, for both 120 and 420 nm disks, meaning that the normalized S_0 that measured for different applied spectral phases overlap with each other, ensuring that the experiment and the analysis bsaed on normalization and background subtraction is healthy. The angular variation in the intensity corresponds to the variation of intensity shown in S_0 image shown in Fig. 6.4. Therefore, since for 120 nm disk, the S_0 image shows nearly a doughnut-like pattern, for a fixed polar angle, the variation in S_0 with respect to the azimuth angle is expected to be nearly constant. On the other hand, for 420 nm disk, since the intensity slightly dominates in the y-direction, we expect to see oscillatory trend in the azimuthal angular distribution of its S_0 parameter.

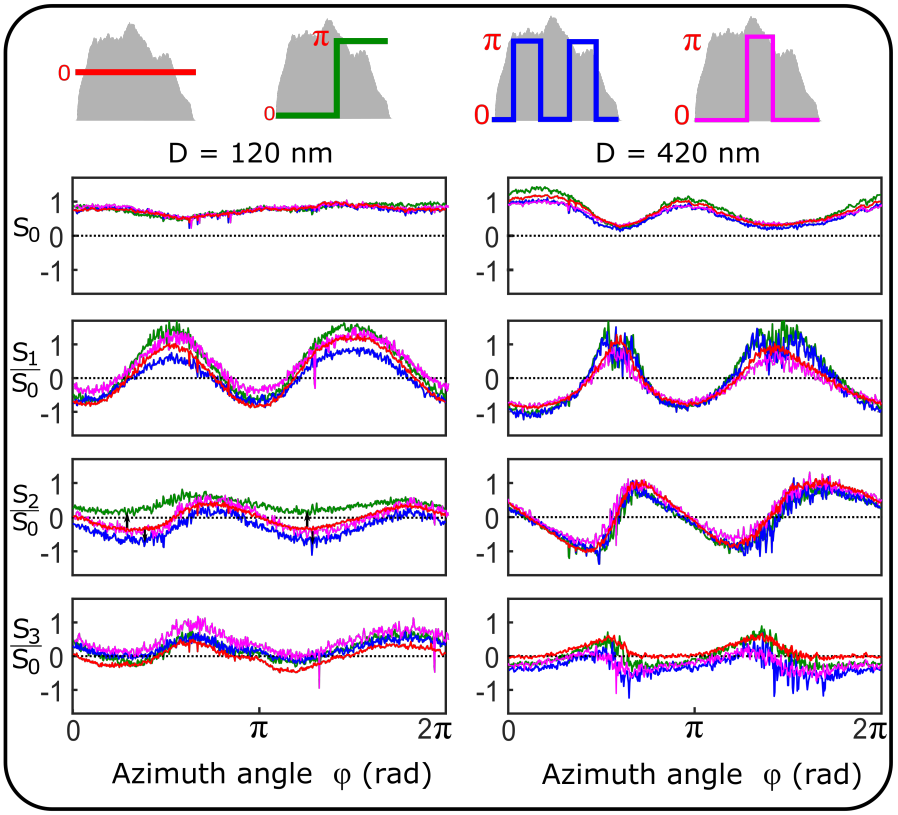

Figure 6.5: **The angular effect of spectral phase on the Stokes parameters**: The variation of S_0, S_1, S_2 and S_3 for 120 and 420 nm disks with respect to the azimuth angle ϕ, integrated over an annular ring of width 6 pixels near the maximum in the angular Stokes maps shown in 6.4. The π-step phases shift to more +45° and -45° polarization components for 120 nm disk while for 420 nm disk no shifting was observed with any of the applied spectral phase. The notch-π-step phase produced no shifting and only a reduction in polarization state.

In the second row, we show the variation in the S_1 parameter for both disks: the curves oscillate around the zero-line as the the ϕ changes from 0 to π, which correspond to the switching between linear horizontal and vertical polarization components in the clockwise direction, distributed nearly symmetrically into 4 quadrants for both disks. As the ϕ is varied, we see that, the polarization state is along x-axis when the $\phi = 0$ and along y-axis when the ϕ=$\frac{\pi}{2}$, reiterating that the SHG is always polarized along the radial direction. For 120 nm disk, only an amplitude change at $\phi = 0.6\pi$ radians and $\phi = 1.6\pi$ radians (π radians apart from each other), that varies beyond the maximum value of 1, which comes from the fact that the normalization with respect to S_0 results in values slightly above 1 for points of lower amplitudes in the angular Stokes images. At all other ϕ values, the S_1 curves nearly overlap with each other, for different applied spectral phases. For 420 nm disk, red, blue and the green curves overlap and the magenta curve shows slight amplitude changes at ϕ = 0.6π and 1.6π radians.

A notable change is observed in the third row, where firstly for 120 nm disk, for the flat phase the S_2 is found to nearly symmetrically vary around 0, meaning the polarization state in k-space changes from $+45^{o}$ -45^{o}, in a given interval of 0 to π of the azimuth angle. We note that the peak-to-peak variation of this oscillation is from -0.75 to 0.75, showing that at any point in k-space, we have no pure $+45^{o}$ or -45^{o} polarization state. By applying the antisymmetric π-step phase, the S_2 is found to shift above 0, such that $0 \geqslant S_2 \leqslant 0.5$. In this case, at any point in the azimuth-angular space, the polarization state oscillates around 0.25. For instance, at $\phi = 0.31\pi$radian, S_2 went from -0.4 to 0.2, implying that the polarization flipped from 40% of -45^{o} state to the 20% $+45^{o}$ state. Also, when $\phi = 0.73\pi$ radians, S_2 went from 0.2 to 0.6, showing a 40% enhancement in $+45^{o}$ polarization state. It has to be noted that, the peak-to-peak height of the oscillation went from 0.8 to less than 0.4. Thus, along with the switching in polarization, we also observe the reduction in the diagonal linear polarization state. On the other hand, with the 5-segment

π-step phase, the S_2 shifted to negative side, such that -0.8 $\leqslant S_2 \leqslant$ 0.2 meaning that the polarization state is biased towards -45^o (i.e., in the opposite direction as achieved by the antisymmetric phase). However, the amplitude of the variation appears to have not changed much. Thus, by means of two different combinations of π step phases on the laser spectrum, it was possible to achieve a controlled, systematic switching between the linear $\pm 45^o$ polarization states of the SHG emission in the angular space. However, with the notch π step phase, not much variation was found in the S_2 parameter, except that the amplitude of the oscillation went down, i.e., a slight reduction in the linear diagonal polarization state. We identify that this could be a result of extremely low SHG signal generated in this case. For 420 nm disk, on the contrary, all the curves overlap with each other.

In the fourth panel, that shows the variation in S_3 parameter, for 120 nm, minor shift towards RCP is observed when going from red to magenta curves, meaning from the flat spectral phase to the notch-type π step phase. For 420 nm disk, there is a slight shift towards LCP, for the identical change of applied spectral phases.

Since identical spectral phase control measurements for both disks with identical background correction and normalizations performed, the variation observed in S_2 for 120 nm disk must be an effect of phase control of interferences achieved for 120 nm disk, since there is a systematic shift observed for different spectral phases applied. The parameters S_1, S_2 show nearly no variation for 420 nm disk, indicating that multipolar spectral interference has not been controlled effectively for this disk size. It has to be stressed here that, all the required BFP images with respective polarization controls were systematically measured under identical alignment conditions, sequentially. We reiterate that, all BFP images were self-referenced with the corresponding S_0 parameter (for each applied spectral phase), which also rule out the possibilities of errors. One has to note here that, the experiment is complex in nature: the spectral phase modulation applied on the laser pulse results in SHG intensity dropping to 40%

and considering that SHG signal (see Fig (5.1) is collected in an em-CCD camera, to a region spread over 200 × 200 pixels. This requires high exposure and long accumulation times. The polarization control at the detection end, further reduces the collected SHG signal.

In summary, the antisymmetric spectral πstep phase and the 5-segment π-step phase succeeded in producing a combined switching and reduction of the linear diagonal polarization states of the 120 nm disk and almost no switching for 420 nm disk. On the other hand, for both disk sizes, for the circular polarization states, no switching and only reduction in the polarization state was observed. With the notch-π step phase, no switching could be achieved, and only minor shifts towards RCP for 120 nm disk and towards LCP for 420 nm disk are observed. Given that the spectral phase control addresses fundamental frequency range, it is important to identify the resonant multipolar modes that are excited and to identify their phase difference. To this end, multipole decomposition at the fundamental spectral range for the two disk sizes was performed.

In Fig. 6.6 we show the results of multipole decomposition. The top panel shows the amplitude of multipolar spectral components upto quadrupoles, for 120 nm disk, in the wavelength range of 750-850 nm, which matches with the excitation laser spectral range (see Fig (6.4), top row) and their corresponding phases. The bottom panel shows the corresponding results for 420 nm disk. For 120 nm disk, in the laser spectral range, the tail of the magnetic dipole m_y can be identified, (see the calculated scattering cross section shown in Fig. 4.3 for different disk sizes) while the amplitude of magnetic quadrupole Q^m_{yz} is constant. The strength of p_x is 10x and that of Q^m_{xz} is 1000x weaker than that of magnetic dipole, hence their contributions are neglected. The spectral phases of all of these multipolar components are nearly similar, with a smooth, linear variation observed across the spectrum. The π-step phase on top of the spectral phase of m_y results in the blue- and the red-driving frequencies of the fundamental electric field oscillate in a different phase, compared to when the phase is flat. This is also the case for Q^m_{yz}. The interference

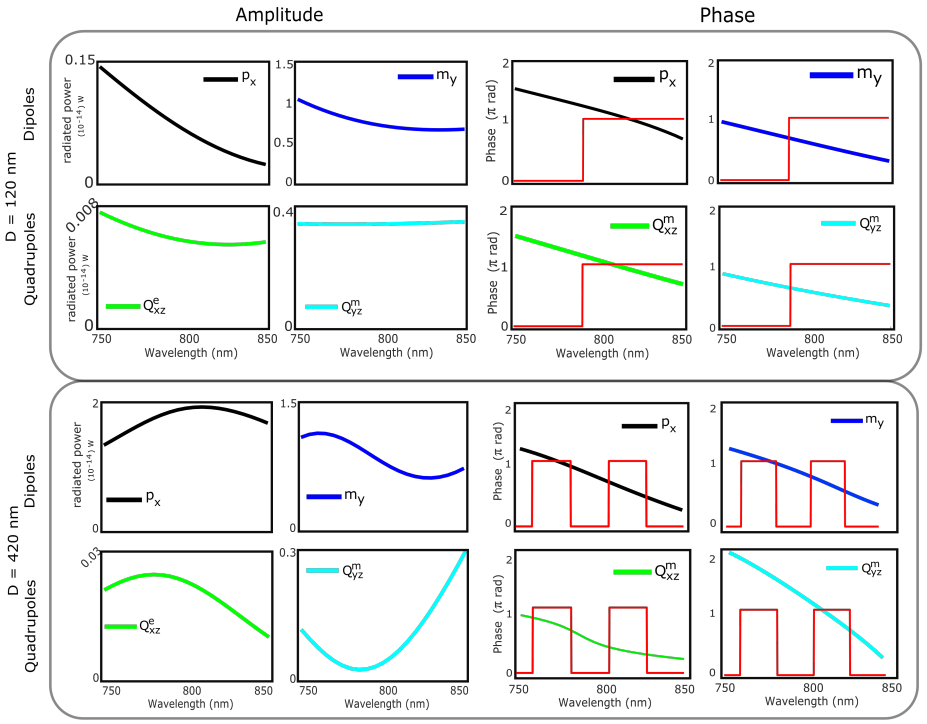

Figure 6.6: **Multipolar spectral decomposition**: Multipole decomposition in the frequency range of 750 to 850 nm spectral range (fundamental) for 120 and 420 nm disks shows that p_x, m_y and Q^m_{yz} are the dominant components. Corresponding phases are shown alongside. Red curves overlaid on top of the phases of the multipolar components, show the applied spectral phase on the excitation laser pulse that produced a notable change in the polarization state.

of these magnetic multipoles in the fundamental frequencies result in a nonlinear mixing that generates SHG with a polarization state different from that when the driving frequencies are unaffected by the flat phase.

As to the 420 nm disk, on the contrary, p_x appears to have a peak around 820 nm with a comparable strength to that of m_y which peaks around 770 nm. However, contrary to the 120 nm disk, the interference appears to not be controlled effectively, neither with the antisymmetric nor with the 5-segment π-step phase.

It has to be noted that, different from the calculated response of a GaP sphere in free space shown in the conceptual schematic in 6.3, in reality, for the GaP nanodisks employed in the experiment lie on the high index GaP substrate resulting in the dipolar and quadrupolar resonances are much broader and the spectral phases only vary smoothly across the excitation spectral range. Thus, the phase difference between the interfering modes are uniform, offering little options of phase control. Needless to say, the spectral phase control is based on the calculated multipolar resonant modes at the fundamental spectral range. Also what has to be noted is that, for bigger disks, multiple modes occur at fundamental spectral range. Additionally, it was observed in Chapter 5 (see Fig (5.9)) that, at SHG frequencies, higher order multipolar modes are responsible for the intensity enhancement, and the polarization character of the SHG emission is non-trivial to explain at the first glance. At any frequency, the polarization state of the SHG is affected by the mixing of modes at fundamental and SHG frequencies. Therefore, it is challenging to arrive to precise conclusions at this stage. It is expected that, performing this experiment on a GaP nanodisk on a low index substrate would yield a much noticeable response, due to the possible sharper resonances and stronger phase differences, and the additional possibility of observing forward-to-backward scattered intensity changes with the change in phase.

Nevertheless, these results give critical insights on the proposed novel approach of tailoring the multipolar spectral interferences, by tuning the spectral phase of the excitation frequencies to achieve directional radiation at SHG frequencies with specific polarization features. In the near future, it is expected that the first demonstration of Kerker effect based on SHG scattering by excitation spectral phase manipulation can be realised through this approach.

6.5 Conclusions

To summarize, in this Chapter, we described the first results of a novel experiment towards controlling the nonlinear multipolar interferences by spectral phase modulation. To this end, we combined spectral phase control of excitation pulses and Stokes polarimetry of the SHG back focal plane imaging. Through this technique, we demonstrated that multipolar interferences can be manipulated by spectral phase modulation, and as a result, polarization state of the SHG radiation pattern of a given resonant nanoantenna can be switched and controlled. However, due to the broad multipolar resonances that interfere non-trivially with a complex phase feature, it is challenging to arrive at precise conclusions at this stage. Nevertheless, our experiment provides useful insights towards achieving the first demonstration of Kerker effect based on SHG in resonant nanoscopic emitters through an all-optical coherent control method.

7

Conclusions and future perspectives

7.1 Conclusion

To summarise, this thesis demonstrated the spectral phase control of second- and third-order nonlinear optical responses in resonant metallic and dielectric nanoantennas.

- In the second chapter, the context of ultrafast spectral phase control of linear and nonlinear responses in nanoemitters was motivated by demonstrating experiments on fluorescence emission of single molecules and second harmonic generation of nanoparticles. It was concluded that in the linear domain, excitation spectral phase has no effect and a nonlinear optical process like second harmonic generation can be quite efficiently controlled by π step phase, based on the interferences between various sum-frequency pathways that occur as the result of interaction of light with a nonlinear nanomaterial.

- In the third chapter, it was shown that in metallic nanoantennas, taking gold as an example, the phase memory of surface plasmon oscillations can be coherently controlled, provided the excitation pulses are made sufficiently shorter, to the scale of the dephasing time in such systems. To show this, we measured the intensity contrast with and without π step phase and observed that the contrast falls off to zero when excitation pulse duration reaches beyond the plasmon dephasing time.

- In the fourth chapter, we investigated a dielectric nanoantenna system, taking a highly nonlinear material like gallium phosphide, and showed that, higher order nonlinear processes can be enhanced by Mie-like resonances and that such low-loss resonances in can sustain longer coherences. With the phase contrast achieved more than that in gold nanorods, we proved that a dielectric nanoresonator can outperform plasmonic resonators in nanoscale coherent control.

- In the fifth chapter, the mechanism of enhancement of second harmonic generation in gallium phosphide nanodisks was investigated and was attributed to the highly concentrated electric energy density in the volume of the disks which generate higher order multipolar modes in the nanodisk through the nonlinear $\chi^{(2)}$ interaction. We performed polarization resolved back focal plane imaging, based on Stokes formalism, of the emitted second harmonic radiation to observe the nonlinear generation of vector beams that are radially polarized, also having small circular components. By a systematic multipole decomposition in the second harmonic spectral range, the dominant multipolar modes responsible for the generation of radially polarized vector beams in the second harmonic radiation pattern were identified.

- In the sixth chapter, we proposed and demonstrated the results of a systematic spectral phase control experiment in which multipolar interferences in dielectric nanoresonators can be tailored by π step phase modulation. We observed for the first time, a switching and reduction in linear diagonal polarization state of SHG angular radiation for a resonant GaP nanodisk. Based on our preliminary numerical analysis, we discussed the observations. Further investigations are ongoing and have not been included in this thesis.

We conclude this thesis by proposing future perspectives on the experimental studies described so far.

7.2 Future perspectives

- In the context of coherent control of surface plasmon resonances, it will be straightforward to extend the experiment in a system with larger dephasing times, for example Ag. However, such an experiment needs a detailed study on the excitation to intermediate state, which, in case of Au, is resonant with our excitation laser spectral range. Furthermore, coupled plasmonic systems, like nano-gap antennas and Fano resonant structures are known to have sharper resonance features, which translates to extended dephasing times. Having said that, one has to be aware of the coupled modes resonant in the system with complicated phase features. We are extending our studies in that direction. In high index dielectric nanostructures, a study on the two-photon photoluminescence and its phase contrast is still in progress, in order to make a fairer comparison with that in Au nanoantennas.

- Although we have been able to understand the resonance enhancement of SHG in GaP nanodisks, we were not free from ambiguities in the multipolar decomposition analysis due to the

extended presence of electric field in the substrate. To resolve this and to have a definite field confinement in the structure of interest, the nanodisks have to be fabricated on a low index substrate. Additionally, the polarization resolved analysis of radiation pattern of GaP nanodisks provided us with the scope of extensive studies towards tailoring nonlinear optical emission properties. We can decompose the dominant multipolar modes in the structure and can tailor the ratio of their intensities by polarization control. This effectively generate vector beams of different properties at the SH frequencies. Needless to say, the crystal orientation in this context plays the most important role in all of this.

- Finally, results of our preliminary investigations showed that, by tailoring the interfering multipolar modes in a high index dielectric nanoantenna, polarization switching can be observed. A structure with sharper resonances, that has considerable overlap with the excitation frequencies, also with a significant phase difference will be required for such an experiment. Alternatively, different from the sample employed for our experiments discussed in Chapter 6, if the GaP nanodisks are fabricated on a transparent, low index substrate, this experiment can be extended in a way to control the forward-to-backward scattering intensity ratio following the spectral phase modulation. Furthermore, on metastructures made of nonlinear materials, we can expect fascinating effects like beam steering and nanoscale pulse shaper for active dispersion control, offering more possibilities of tailoring the directionality of nonlinear emission.

Publications

The work described in this thesis has resulted in following publications:

1. **Vikas Remesh**, Michael Stührenberg, Lisa Saemisch, Nicolò Accanto, and Niek F. van Hulst, *Phase control of plasmon enhanced twophoton photoluminescence in resonant gold nanoantennas*, Appl. Phys. Lett. 113, 211101 (2018).

2. **Vikas Remesh**, Gustavo Grinblat, Yi Li, Stefan Maier and Niek F. van Hulst, *Coherent Multiphoton Control of Gallium Phosphide Nanodisk Resonances*, ACS Photonics 2019, 6, 10, 2487-2491.

3. **Vikas Remesh** and Niek F. van Hulst, Spectral phase control of broadband second harmonic generation of nanoparticles, *in preparation*

4. Pawel Wozniak, **Vikas Remesh**, Monserrat Alvarez Ortiz, Gustavo Grinblat, Yi Li, Stefan Maier and Niek F. van Hulst, Spectral phase control of multipolar interferences in resonant GaP nanodisks by polarization readout, *in preparation*

Acknowledgements

"Perhaps the story you finish is never the one you begin."

Salman Rushdie, Midnights Children

Let me be honest, it was tough. I could learn a lot during this PhD life and I am thankful to many in this occassion. Looking back, I was pretty fortunate to join this group, after answering the email from Prof. Niek van Hulst in February 2014. It was with a lot of ambiguities and anxieties but also with a fair share of personal excitement that I made the choice then. From the very first day, right from setting up a comfort space, to occasional enquiries on life, to the enormous fun in the post-lunch-coffee-room-talks, Niek had set up a wonderful atmosphere of freedom and self confidence in his group that once you land in, you would only love it and never would like to leave it. I have to thank Niek really a lot, for making me grow different and for breaking the shell I was comfortable in, for good reasons, and for accepting me the way I am. Thank you Niek, for your trust in me, for heaven-knows-what reason and all I can tell you is that, I promise I would take these values wherever I go in future.

Thank you Nicolo, who spent a lot of time training me in the lab during my first years, despite my slowest learning curve. Thank you Richard, for all the initial support and help. Cheers to Alex Block, for those shared dreams of starting-PhDs in Lab2. Thanks to Anshu for a lot of motivation and inspiration. To James, Ion, Pablo, Unai, Lukasz, Gaëtan, Michael, Esther, Nicola, Guilia, Saurabh and Lisa-

for all those wonderful, half-nerdy-half-sarcastic time in the group. Thanks Pawel, for joining the group at the RIGHT moment and guiding me a lot to redirect the whole course of PhD in the last year! I owe you big time. Cheers Matz for the *scientific* attitude you carry and for answers to everything. Jana, Nick, AlexD, *valar morghulis*! Dear molnano family, thanks, really, for a fabulous time.

ICFO has given me a lot of friends and people to remember forever in my life. Rinu, for being my ever-approachable friend here. KKG, Hari chettan, Nitinettan: for all the *mallu-gang* fun! Pamina, Sandra, Alvaro, Julio, Ugaitz, Vindhiya, Anuja, Rafael, Laurent, Susmita- for the *compaña de cosas chulas* and nice trips !! I thank the HR, Logistics, Maintenance, Purchasing, Workshop, IT sections and Cafeteria at ICFO for providing a comfortable workspace.

I thank everyone who got involved in my limited social life in Barcelona: Monse, Zoraze, Aamir, Christina: thank you guys for the fun-filled time. To the Poetry, Chess, Bridge, Comedy, Movie and Book clubs in Barcelona for making my life in Barcelona a memorable one. To my very special Kerala gang: Thomas, Adara, Diya, Chithran, Jery, Jewel, Stefy, Sebin: for the enormous laughing times! To Vrinda, thank you for being the greatest listener and the critic :)

To the Indian community at ICFO: a big shout out !!! To the memorable people in my life: Thajri, Prafulla, Kripri, Nikhilsanth, Nikhil P, Rachana, Nidhi, Aswin, Sruthi, Reenu, Nijil, Jishna, Nimisha, Susmith..thanks for being my FRIENDS :)

I would not have written this thesis had I not had the support of my family. Acha, for the fire you ignited in me. You deserve the me I am today. Forever you are my hero. Amma, for the emotion you gave me. I will be yours forever. Ashi, for understanding this weirdest brother you have. I wish I could give you more of me. For everyone else in the family network: for being supportive, although not knowing what I am actually doing! You all are in my heart.

Bibliography

[1] Brian Vohnsen. A short history of optics. *Physica Scripta*, 2004(T109):75, 2004.

[2] Isaac Asimov. *The history of physics*. Walker, 1983.

[3] Max Born and Emil Wolf. *Principles of optics: electromagnetic theory of propagation, interference and diffraction of light*. Elsevier, 2013.

[4] A. Einstein. The quantum theory of radiation. *Physikalische Zeitschrift*, 18:121, 1917.

[5] Lukas Novotny and Bert Hecht. *Principles of nano-optics*. Cambridge university press, 2012.

[6] Sergey V Gaponenko. *Introduction to nanophotonics*. Cambridge University Press, 2010.

[7] Paras N Prasad. *Nanophotonics*. John Wiley & Sons, 2004.

[8] Mark I Stockman. Nanoplasmonics: past, present, and glimpse into future. *Optics express*, 19(22):22029–22106, 2011.

[9] Palash Bharadwaj, Bradley Deutsch, and Lukas Novotny. Optical antennas. *Advances in Optics and Photonics*, 1(3):438–483, 2009.

[10] RH Ritchie and HB Eldridge. Optical emission from irradiated foils. i. *Physical Review*, 126(6):1935, 1962.

[11] RH Ritchie. Surface plasmons in solids. *Surface Science*, 34(1):1–19, 1973.

[12] V Giannini and José A Sánchez-Gil. Excitation and emission enhancement of single molecule fluorescence through multiple surface-plasmon resonances on metal trimer nanoantennas. *optics letters*, 33(9):899–901, 2008.

[13] Anika Kinkhabwala, Zongfu Yu, Shanhui Fan, Yuri Avlasevich, Klaus Müllen, and W. E. Moerner. Large single-molecule fluorescence enhancements produced by a bowtie nanoantenna. *Nature Photonics*, 3(11):654–657, 2009.

[14] P Anger, P Bharadwaj, and Lukas Novotny. Enhancement and quenching of single-molecule fluorescence. *Physical Review Letters*, 96(11):113002, 2006.

[15] Katrin Kneipp, Yang Wang, Harald Kneipp, Lev T. Perelman, Irving Itzkan, Ramachandra R. Dasari, and Michael S. Feld. Single molecule detection using surface-enhanced raman scattering (SERS). *Physical Review Letters*, 78(9):1667–1670, 1997.

[16] Shuming Nie and Steven R. Emory. Probing single molecules and single nanoparticles by surface-enhanced Raman scattering. *Science*, 275(5303):1102–1106, 1997.

[17] Sergei Kühn, Ulf Håkanson, Lavinia Rogobete, and Vahid Sandoghdar. Enhancement of single-molecule fluorescence using a gold nanoparticle as an optical nanoantenna. *Physical review letters*, 97(1):017402, 2006.

[18] Markus Pfeiffer, Klas Lindfors, Christian Wolpert, Paola Atkinson, Mohamed Benyoucef, Armando Rastelli, Oliver G Schmidt, Harald Giessen, and Markus Lippitz. Enhancing the optical excitation efficiency of a single self-assembled quantum dot with a plasmonic nanoantenna. *Nano letters*, 10(11):4555–4558, 2010.

[19] Gleb M Akselrod, Christos Argyropoulos, Thang B Hoang, Cristian Ciracì, Chao Fang, Jiani Huang, David R Smith, and Maiken H Mikkelsen. Probing the mechanisms of large purcell enhancement in plasmonic nanoantennas. *Nature Photonics*, 8(11):835, 2014.

[20] OL Muskens, V Giannini, José A Sánchez-Gil, and J Gómez Rivas. Strong enhancement of the radiative decay rate of emitters by single plasmonic nanoantennas. *Nano letters*, 7(9):2871–2875, 2007.

[21] Krishnan Thyagarajan, Simon Rivier, Andrea Lovera, and Olivier JF Martin. Enhanced second-harmonic generation from double resonant plasmonic antennae. *Optics express*, 20(12):12860–12865, 2012.

[22] Bernd Metzger, Mario Hentschel, Thorsten Schumacher, Markus Lippitz, Xingchen Ye, Christopher B Murray, Bastian Knabe, Karsten Buse, and Harald Giessen. Doubling the efficiency of third harmonic generation by positioning ito nanocrystals into the hot-spot of plasmonic gap-antennas. *Nano letters*, 14(5):2867–2872, 2014.

[23] Pai-Yen Chen, Christos Argyropoulos, and Andrea Alù. Enhanced nonlinearities using plasmonic nanoantennas. *Nanophotonics*, 1(3-4):221–233, 2012.

[24] Miguel Navarro-Cia and Stefan A Maier. Broad-band near-infrared plasmonic nanoantennas for higher harmonic generation. *ACS nano*, 6(4):3537–3544, 2012.

[25] Markus Lippitz, Meindert A van Dijk, and Michel Orrit. Third-harmonic generation from single gold nanoparticles. *Nano letters*, 5(4):799–802, 2005.

[26] Martti Kauranen and Anatoly V Zayats. Nonlinear plasmonics. *Nature photonics*, 6(11):737, 2012.

[27] Jeremy Butet, Pierre-Francois Brevet, and Olivier JF Martin. Optical second harmonic generation in plasmonic nanostructures: from fundamental principles to advanced applications. *ACS nano*, 9(11):10545–10562, 2015.

[28] Svetlana V Boriskina, Thomas Alan Cooper, Lingping Zeng, George Ni, Jonathan K Tong, Yoichiro Tsurimaki, Yi Huang, Laureen Meroueh, Gerald Mahan, and Gang Chen. Losses in plasmonics: from mitigating energy dissipation to embracing loss-enabled functionalities. *Advances in Optics and Photonics*, 9(4):775–827, 2017.

[29] Ursula Keller. Recent developments in compact ultrafast lasers. *Nature*, 424(6950):831, 2003.

[30] Thomas Brabec, Ch Spielmann, PF Curley, and Ferenc Krausz. Kerr lens mode locking. *Optics letters*, 17(18):1292–1294, 1992.

[31] Michael D Cahalan, Ian Parker, Sindy H Wei, and Mark J Miller. Two-photon tissue imaging: seeing the immune system in a fresh light. *Nature Reviews Immunology*, 2(11):872, 2002.

[32] Peng Xi, Yair Andegeko, Dmitry Pestov, Vadim V Lozovoy, and Marcos M Dantus. Two-photon imaging using adaptive phase compensated ultrashort laser pulses. *Journal of biomedical optics*, 14(1):014002, 2009.

[33] Friedrich Dausinger and Friedemann Lichtner. *Femtosecond technology for technical and medical applications*, volume 96. Springer Science & Business Media, 2004.

[34] ED Potter, JL Herek, S Pedersen, Q Liu, and AH Zewail. Femtosecond laser control of a chemical reaction. *Nature*, 355(6355):66, 1992.

[35] NF Scherer, AJ Ruggiero, M Du, and GR Fleming. Time resolved dynamics of isolated molecular systems studied with phase-locked femtosecond pulse pairs. *The Journal of Chemical Physics*, 93(1):856–857, 1990.

[36] Shaul Mukamel. Femtosecond optical spectroscopy: a direct look at elementary chemical events. *Annual Review of Physical Chemistry*, 41(1):647–681, 1990.

[37] Nicolò Accanto, Jana B Nieder, Lukasz Piatkowski, Marta Castro-Lopez, Francesco Pastorelli, Daan Brinks, and Niek F Van Hulst. Phase control of femtosecond pulses on the nanoscale using second harmonic nanoparticles. *Light: Science & Applications*, 3(1):e143, 2014.

[38] Lukasz Piatkowski, Nicol"ø" Accanto, and Niek F van Hulst. Ultrafast meets ultrasmall: controlling nanoantennas and molecules. *ACS Photonics*, 3(8):1401–1414, 2016.

[39] Erik M""rsell, Arthur Losquin, Robin Svard, Miguel Miranda, Chen Guo, Anne Harth, Eleonora Lorek, Johan Mauritsson, Cord L Arnold, Hongxing Xu, et al. Nanoscale imaging of local few-femtosecond near-field dynamics within a single plasmonic nanoantenna. *Nano letters*, 15(10):6601–6608, 2015.

[40] Minsky Marvin. Microscopy apparatus, December 19 1961. US Patent 3,013,467.

[41] Alberto Diaspro et al. *Confocal and two-photon microscopy: foundations, applications, and advances*, volume 1. Wiley-Liss New York, 2002.

[42] James Pawley. *Handbook of biological confocal microscopy*. Springer Science & Business Media, 2010.

[43] Peter Seitz and Albert JP Theuwissen. *Single-photon imaging*, volume 160. Springer Science & Business Media, 2011.

[44] Lijian Zhang, Leonardo Neves, Jeff S Lundeen, and Ian A Walmsley. A characterization of the single-photon sensitivity of an electron multiplying charge-coupled device. *Journal of Physics B: Atomic, Molecular and Optical Physics*, 42(11):114011, 2009.

[45] Shuming Nie, Daniel T Chiu, and Richard N Zare. Probing individual molecules with confocal fluorescence microscopy. *Science*, 266(5187):1018–1021, 1994.

[46] Ph Tamarat, A Maali, B Lounis, and M Orrit. Ten years of single-molecule spectroscopy. *The Journal of Physical Chemistry A*, 104(1):1–16, 2000.

[47] A Kiraz, S Fälth, C Becher, B Gayral, WV Schoenfeld, PM Petroff, Lidong Zhang, E Hu, and A Imamoğlu. Photon correlation spectroscopy of a single quantum dot. *Physical Review B*, 65(16):161303, 2002.

[48] Matz Liebel, Costanza Toninelli, and Niek F van Hulst. Room-temperature ultrafast nonlinear spectroscopy of a single molecule. *Nature Photonics*, 12(1):45–49, 2018.

[49] Gregory S Engel, Tessa R Calhoun, Elizabeth L Read, Tae-Kyu Ahn, Tomáš Mančal, Yuan-Chung Cheng, Robert E Blankenship, and Graham R Fleming. Evidence for wavelike energy transfer through quantum coherence in photosynthetic systems. *Nature*, 446(7137):782–786, 2007.

[50] Thaddeus D Ladd, Fedor Jelezko, Raymond Laflamme, Yasunobu Nakamura, Christopher Monroe, and Jeremy Lloyd O'Brien. Quantum computers. *Nature*, 464(7285):45–53, 2010.

[51] Richard Hildner, Daan Brinks, Jana B Nieder, Richard J Cogdell, and Niek F van Hulst. Quantum coherent energy transfer over varying pathways in single light-harvesting complexes. *Science*, 340(6139):1448–1451, 2013.

[52] Eleftherios Goulielmakis, Zhi-Heng Loh, Adrian Wirth, Robin Santra, Nina Rohringer, Vladislav S Yakovlev, Sergey Zherebtsov, Thomas Pfeifer, Abdallah M Azzeer, Matthias F Kling, et al. Real-time observation of valence electron motion. *Nature*, 466(7307):739–743, 2010.

[53] TH Stievater, Xiaoqin Li, D Gammon Steel, D Gammon, DS Katzer, D Park, C Piermarocchi, and LJ Sham. Rabi oscillations of excitons in single quantum dots. *Physical Review Letters*, 87(13):133603, 2001.

[54] Charles Santori, David Fattal, Jelena Vučković, Glenn S Solomon, and Yoshihisa Yamamoto. Indistinguishable photons from a single-photon device. *nature*, 419(6907):594–597, 2002.

[55] R Mark Stevenson, Robert J Young, Paola Atkinson, Ken Cooper, David A Ritchie, and Andrew J Shields. A semiconductor source of triggered entangled photon pairs. *Nature*, 439(7073):179–182, 2006.

[56] Richard Hildner, Daan Brinks, and Niek F Van Hulst. Femtosecond coherence and quantum control of single molecules at room temperature. *Nature Physics*, 7(2):172, 2011.

[57] H Kamada, H Gotoh, J Temmyo, Toshihide Takagahara, and H Ando. Exciton rabi oscillation in a single quantum dot. *Physical Review Letters*, 87(24):246401, 2001.

[58] Moshe Shapiro and Paul Brumer. Principles of the quantum control of molecular processes. *Principles of the Quantum Control of Molecular Processes, by Moshe Shapiro, Paul Brumer, pp. 250. ISBN 0-471-24184-9. Wiley-VCH, February 2003.*, page 250, 2003.

[59] Warren S Warren, Herschel Rabitz, and Mohammed Dahleh. Coherent control of quantum dynamics: the dream is alive. *Science*, 259(5101):1581–1589, 1993.

[60] David J Tannor and Stuart A Rice. Coherent pulse sequence control of product formation in chemical reactions. *Advances in Chemical Physics: Evolution of Size Effects in Chemical Dynamics Part 1*, 70:441–523, 1988.

[61] Herschel Rabitz. Focus on quantum control. *New Journal of Physics*, 11(10):105030, 2009.

[62] Izak Levy, Moshe Shapiro, and Paul Brumer. Two-pulse coherent control of electronic states in the photodissociation of ibr: Theory and proposed experiment. *The Journal of Chemical Physics*, 93(4):2493–2498, 1990.

[63] CK Chan, P Brumer, and M Shapiro. Coherent radiative control of ibr photodissociation via simultaneous ($\omega 1$, $\omega 3$) excitation. *The Journal of chemical physics*, 94(4):2688–2696, 1991.

[64] Allon Bartana, Ronnie Kosloff, and David J Tannor. Laser cooling of internal degrees of freedom. ii. *The Journal of chemical physics*, 106(4):1435–1448, 1997.

[65] Jennifer L Herek, Wendel Wohlleben, Richard J Cogdell, Dirk Zeidler, and Marcus Motzkus. Quantum control of energy flow in light harvesting. *Nature*, 417(6888):533, 2002.

[66] Akihito Ishizaki and Graham R Fleming. Quantum coherence in photosynthetic light harvesting. *Annu. Rev. Condens. Matter Phys.*, 3(1):333–361, 2012.

[67] R. Trebino. *Frequency-Resolved Optical Gating: The Measurement of Ultrashort Laser Pulses: The Measurement of Ultrashort Laser Pulses*. Springer US, 2000.

[68] Rick Trebino, Kenneth W DeLong, David N Fittinghoff, John N Sweetser, Marco A Krumbgel, Bruce A Richman, and Daniel J Kane. Measuring ultrashort laser pulses in the time-frequency

domain using frequency-resolved optical gating. *Review of Scientific Instruments*, 68(9):3277–3295, 1997.

[69] Jean-Claude Diels and Wolfgang Rudolph. *Ultrashort laser pulse phenomena*. Elsevier, 2006.

[70] Andrew M Weiner. Ultrafast optical pulse shaping: A tutorial review. *Optics Communications*, 284(15):3669–3692, 2011.

[71] Jeffrey B Guild, Chris Xu, and Watt W Webb. Measurement of group delay dispersion of high numerical aperture objective lenses using two-photon excited fluorescence. *Applied Optics*, 36(1):397–401, 1997.

[72] T Baumert, T Brixner, V Seyfried, M Strehle, and G Gerber. Femtosecond pulse shaping by an evolutionary algorithm with feedback. *Applied Physics B: Lasers and Optics*, 65(6):779–782, 1997.

[73] Dirk Zeidler, S Frey, K-L Kompa, and M Motzkus. Evolutionary algorithms and their application to optimal control studies. *Physical Review A*, 64(2):023420, 2001.

[74] T Brixner, M Strehle, and G Gerber. Feedback-controlled optimization of amplified femtosecond laser pulses. *Applied Physics B: Lasers and Optics*, 68(2):281–284, 1999.

[75] . https://spie.org/publications/fg14_p01-04_optical_pulses?SSO=1.

[76] . https://www.rp-photonics.com/gaussian_pulses.html.

[77] Antoine Monmayrant, Sébastien Weber, and Béatrice Chatel. A newcomer's guide to ultrashort pulse shaping and characterization. *Journal of Physics B: Atomic, Molecular and Optical Physics*, 43(10):103001, 2010.

[78] Daniel J Kane and Rick Trebino. Single-shot measurement of the intensity and phase of an arbitrary ultrashort pulse by using frequency-resolved optical gating. *Optics letters*, 18(10):823–825, 1993.

[79] Gero Stibenz and Günter Steinmeyer. Interferometric frequency-resolved optical gating. *Optics express*, 13(7):2617–2626, 2005.

[80] Chris Iaconis and Ian A Walmsley. Spectral phase interferometry for direct electric-field reconstruction of ultrashort optical pulses. *Optics letters*, 23(10):792–794, 1998.

[81] Selcuk Akturk, Mark Kimmel, Patrick O'Shea, and Rick Trebino. Measuring pulse-front tilt in ultrashort pulses using grenouille. *Optics Express*, 11(5):491–501, 2003.

[82] Pamela Bowlan, Pablo Gabolde, Aparna Shreenath, Kristan McGresham, Rick Trebino, and Selcuk Akturk. Crossed-beam spectral interferometry: a simple, high-spectral-resolution method for completely characterizing complex ultrashort pulses in real time. *Optics Express*, 14(24):11892–11900, 2006.

[83] Dmitry Pestov, Vadim V Lozovoy, and Marcos Dantus. Single-beam shaper-based pulse characterization and compression using miips sonogram. *Optics letters*, 35(9):1422–1424, 2010.

[84] Vadim V Lozovoy, Igor Pastirk, and Marcos Dantus. Multiphoton intrapulse interference. iv. ultrashort laser pulse spectral phase characterization and compensation. *Optics letters*, 29(7):775–777, 2004.

[85] Igor Pastirk, Bojan Resan, Alan Fry, John MacKay, and M Dantus. No loss spectral phase correction and arbitrary phase shaping of regeneratively amplified femtosecond pulses using miips. *Optics Express*, 14(20):9537–9543, 2006.

[86] Alberto Comin, Richard Ciesielski, Giovanni Piredda, Kevin Donkers, and Achim Hartschuh. Compression of ultrashort laser pulses via gated multiphoton intrapulse interference phase scans. *JOSA B*, 31(5):1118–1125, 2014.

[87] Stefan Alexander Maier. *Plasmonics: fundamentals and applications*. Springer Science & Business Media, 2007.

[88] Doron Meshulach and Yaron Silberberg. Coherent quantum control of multiphoton transitions by shaped ultrashort optical pulses. *Physical Review A*, 60(2):1287, 1999.

[89] Gitt Panitchayangkoon, Dmitri V Voronine, Darius Abramavicius, Justin R Caram, Nicholas HC Lewis, Shaul Mukamel, and Gregory S Engel. Direct evidence of quantum transport in photosynthetic light-harvesting complexes. *Proceedings of the National Academy of Sciences*, 108(52):20908–20912, 2011.

[90] Elad Harel and Gregory S Engel. Quantum coherence spectroscopy reveals complex dynamics in bacterial light-harvesting complex 2 (lh2). *Proceedings of the National Academy of Sciences*, 109(3):706–711, 2012.

[91] Gregory D Scholes. Quantum biology: coherence in photosynthesis. *Nature Physics*, 7(6):448, 2011.

[92] Carlo Andrea Rozzi, Sarah Maria Falke, Nicola Spallanzani, Angel Rubio, Elisa Molinari, Daniele Brida, Margherita Maiuri, Giulio Cerullo, Heiko Schramm, Jens Christoffers, et al. Quantum coherence controls the charge separation in a prototypical artificial light-harvesting system. *Nature communications*, 4:1602, 2013.

[93] Janne Savolainen, Riccardo Fanciulli, Niels Dijkhuizen, Ana L Moore, Jürgen Hauer, Tiago Buckup, Marcus Motzkus, and

Jennifer L Herek. Controlling the efficiency of an artificial light-harvesting complex. *Proceedings of the National Academy of Sciences*, 105(22):7641–7646, 2008.

[94] Hideki Hashimoto, Yuko Sugai, Chiasa Uragami, Alastair T Gardiner, and Richard J Cogdell. Natural and artificial light-harvesting systems utilizing the functions of carotenoids. *Journal of Photochemistry and Photobiology C: Photochemistry Reviews*, 25:46–70, 2015.

[95] Norbert F Scherer, Roger J Carlson, Alexander Matro, Mei Du, Anthony J Ruggiero, Victor Romero-Rochin, Jeffrey A Cina, Graham R Fleming, and Stuart A Rice. Fluorescence-detected wave packet interferometry: Time resolved molecular spectroscopy with sequences of femtosecond phase-locked pulses. *The Journal of chemical physics*, 95(3):1487–1511, 1991.

[96] Joseph G Hirschberg, György Vereb, Christoph K Meyer, Achim K Kirsch, Eli Kohen, and Thomas M Jovin. Interferometric measurement of fluorescence excitation spectra. *Applied optics*, 37(10):1953–1957, 1998.

[97] Jennifer P Ogilvie, Kevin J Kubarych, Antigoni Alexandrou, and Manuel Joffre. Fourier transform measurement of two-photon excitation spectra: applications to microscopy and optimal control. *Optics letters*, 30(8):911–913, 2005.

[98] Eriko Tokunaga, Akira Terasaki, and Takayoshi Kobayashi. Frequency-domain interferometer for femtosecond time-resolved phase spectroscopy. *Optics letters*, 17(16):1131–1133, 1992.

[99] Lukasz Piatkowski, Esther Gellings, and Niek F Van Hulst. Broadband single-molecule excitation spectroscopy. *Nature communications*, 7:10411, 2016.

[100] M Liebel and P Kukura. Lack of evidence for phase-only control of retinal photoisomerization in the strict one-photon limit. *Nature chemistry*, 9(1):45, 2017.

[101] Alexander Weigel, Aleksandar Sebesta, and Philipp Kukura. Shaped and feedback-controlled excitation of single molecules in the weak-field limit. *The journal of physical chemistry letters*, 6(20):4032–4037, 2015.

[102] B Broers, HB van Linden van den Heuvell, and LD Noordam. Large interference effects of small chirp observed in two-photon absorption. *Optics communications*, 91(1-2):57–61, 1992.

[103] Marcos Dantus and Vadim V Lozovoy. Experimental coherent laser control of physicochemical processes. *Chemical reviews*, 104(4):1813–1860, 2004.

[104] Marcos Dantus. Coherent nonlinear spectroscopy: from femtosecond dynamics to control. *Annual Review of Physical Chemistry*, 52(1):639–679, 2001.

[105] Johanna M Dela Cruz, Igor Pastirk, Vadim V Lozovoy, Katherine A Walowicz, and Marcos Dantus. Multiphoton intrapulse interference 3: Probing microscopic chemical environments. *The Journal of Physical Chemistry A*, 108(1):53–58, 2004.

[106] Robert W. Boyd. *Nonlinear Optics, Third Edition*. Academic Press, Inc., Orlando, FL, USA, 3rd edition, 2008.

[107] Paul N Butcher and David Cotter. *The elements of nonlinear optics*, volume 9. Cambridge university press, 1990.

[108] CJ Bardeen, Q Wang, and CV Shank. Selective excitation of vibrational wave packet motion using chirped pulses. *Physical review letters*, 75(19):3410, 1995.

[109] H Petek, AP Heberle, W Nessler, H Nagano, S Kubota, S Matsunami, N Moriya, and S Ogawa. Optical phase control of coherent electron dynamics in metals. *Physical review letters*, 79(23):4649, 1997.

[110] Debabrata Goswami. Optical pulse shaping approaches to coherent control. *Physics Reports*, 374(6):385–481, 2003.

[111] Chris Xu and Watt W. Webb. Measurement of two-photon excitation cross sections of molecular fluorophores with data from 690 to 1050 nm. *Journal of the Optical Society of America B*, 13(3):481, 1996.

[112] Shuo Tang, Tatiana B. Krasieva, Zhongping Chen, Gabriel Tempea, and Bruce J. Tromberg. Effect of pulse duration on two-photon excited fluorescence and second harmonic generation in nonlinear optical microscopy. *Journal of Biomedical Optics*, 11(2):020501, 2006.

[113] Andrew C Millard, Paul J Campagnola, William Mohler, Aaron Lewis, and Leslie M Loew. [3] second harmonic imaging microscopy. In *Methods in enzymology*, volume 361, pages 47–69. Elsevier, 2003.

[114] Patrick Stoller, Karen M Reiser, Peter M Celliers, and Alexander M Rubenchik. Polarization-modulated second harmonic generation in collagen. *Biophysical journal*, 82(6):3330–3342, 2002.

[115] Paul J Campagnola, Aaron Lewis, Leslie M Loew, et al. High-resolution nonlinear optical imaging of live cells by second harmonic generation. *Biophysical journal*, 77(6):3341–3349, 1999.

[116] Paul J Campagnola and Leslie M Loew. Second-harmonic imaging microscopy for visualizing biomolecular arrays in cells, tissues and organisms. *Nature biotechnology*, 21(11):1356–1360, 2003.

[117] Warren R Zipfel, Rebecca M Williams, Richard Christie, Alexander Yu Nikitin, Bradley T Hyman, and Watt W Webb. Live tissue intrinsic emission microscopy using multiphoton-excited native fluorescence and second harmonic generation. *Proceedings of the National Academy of Sciences*, 100(12):7075–7080, 2003.

[118] Aaron Lewis, Artium Khatchatouriants, Millet Treinin, Zhongping Chen, Gadi Peleg, Noga Friedman, Oleg Bouevitch, Zvi Rothman, Leslie Loew, and Mordechai Sheres. Second-harmonic generation of biological interfaces: probing the membrane protein bacteriorhodopsin and imaging membrane potential around gfp molecules at specific sites in neuronal cells of c. elegans. *Chemical Physics*, 245(1-3):133–144, 1999.

[119] Mutsuo Nuriya, Jiang Jiang, Boaz Nemet, Kenneth B Eisenthal, and Rafael Yuste. Imaging membrane potential in dendritic spines. *Proceedings of the National Academy of Sciences*, 103(3):786–790, 2006.

[120] Daniel A Dombeck, Mireille Blanchard-Desce, and Watt W Webb. Optical recording of action potentials with second-harmonic generation microscopy. *Journal of Neuroscience*, 24(4):999–1003, 2004.

[121] Daniel Axelrod. Carbocyanine dye orientation in red cell membrane studied by microscopic fluorescence polarization. *Biophysical journal*, 26(3):557–573, 1979.

[122] Sophie Brasselet. Polarization-resolved nonlinear microscopy: application to structural molecular and biological imaging. *Advances in Optics and Photonics*, 3(3):205, 2011.

[123] Naveen Kumar Balla, Carolina Rendón-Barraza, Luong Mai Hoang, Pawel Karpinski, Esteban Bermúdez-Ureña, and Sophie

Brasselet. Polarized nonlinear nanoscopy of metal nanostructures. *ACS photonics*, 4(2):292–301, 2017.

[124] Ivan Gusachenko, Gaël Latour, and Marie-Claire Schanne-Klein. Polarization-resolved second harmonic microscopy in anisotropic thick tissues. *Optics Express*, 18(18):19339–19352, 2010.

[125] Minghao Sun, Honghui He, Nan Zeng, E Du, Yihong Guo, Shaoxiong Liu, Jian Wu, Yonghong He, and Hui Ma. Characterizing the microstructures of biological tissues using mueller matrix and transformed polarization parameters. *Biomedical optics express*, 5(12):4223–4234, 2014.

[126] Evgeniy A Mamonov, Anton I Maydykovskiy, Irina A Kolmychek, Sergey A Magnitskiy, and Tatiana V Murzina. Polarization-resolved second harmonic generation microscopy of chiral g-shaped metamaterials. *Physical Review B*, 96(7):075408, 2017.

[127] Sascha Trippe. Polarization and polarimetry: A review. *arXiv preprint arXiv:1401.1911*, 2014.

[128] Nirmal Mazumder, Jianjun Qiu, Matthew R Foreman, Carlos Macías Romero, Chih-Wei Hu, Han-Ruei Tsai, Peter Török, and Fu-Jen Kao. Polarization-resolved second harmonic generation microscopy with a four-channel stokes-polarimeter. *Optics express*, 20(13):14090–14099, 2012.

[129] RMA Azzam. Stokes-vector and mueller-matrix polarimetry. *JOSA A*, 33(7):1396–1408, 2016.

[130] Beth Schaefer, Edward Collett, Robert Smyth, Daniel Barrett, and Beth Fraher. Measuring the stokes polarization parameters. *American Journal of Physics*, 75(2):163–168, 2007.

[131] Nicolò Accanto, Lukasz Piatkowski, Jan Renger, and Niek F. Van Hulst. Capturing the optical phase response of nanoantennas by coherent second-harmonic microscopy. *Nano Letters*, 14(7):4078–4082, 2014.

[132] Alexandria Anderson, Kseniya S. Deryckx, Xiaoji G. Xu, Günter Steinmeyer, and Markus B. Raschke. Few-femtosecond plasmon dephasing of a single metallic nanostructure from optical response function reconstruction by interferometric frequency resolved optical gating. *Nano Letters*, 10(7):2519–2524, 2010.

[133] Tian Zhao, Jeremy W. Jarrett, Jeffrey S. Johnson, Kyoungweon Park, Richard A. Vaia, and Kenneth L. Knappenberger. Plasmon Dephasing in Gold Nanorods Studied Using Single-Nanoparticle Interferometric Nonlinear Optical Microscopy. *Journal of Physical Chemistry C*, 120(7):4071–4079, 2016.

[134] M.I. Stockman, S.V. Faleev, and D.J. Bergman. Coherent control of femtosecond energy localization in nanosystems. *Physical Review Letters*, 88(6):067402/1–067402/4, 2002.

[135] Mark I. Stockman, David J. Bergman, and Takayoshi Kobayashi. Coherent control of nanoscale localization of ultrafast optical excitation in nanosystems. *Physical Review B - Condensed Matter and Materials Physics*, 69(5):054202, 2004.

[136] Martin Aeschlimann, Michael Bauer, Daniela Bayer, Tobias Brixner, F. Javier García De Abajo, Walter Pfeiffer, Martin Rohmer, Christian Spindler, and Felix Steeb. Adaptive subwavelength control of nano-optical fields. *Nature*, 446(7133):301–304, 2007.

[137] Sergio G. Rodrigo, Hayk Harutyunyan, and Lukas Novotny. Coherent control of light scattering from nanostructured materials by second-harmonic generation. *Physical Review Letters*, 110(17):1–5, 2013.

[138] Maxim Sukharev and Tamar Seideman. Phase and polarization control as a route to plasmonic nanodevices. *Nano Letters*, 6(4):715–719, 2006.

[139] Francesco Papoff, Duncan McArthur, and Ben Hourahine. Coherent control of radiation patterns of nonlinear multiphoton processes in nanoparticles. *Scientific Reports*, 5:1–9, 2015.

[140] Tae Woo Lee and Stephen K. Gray. Controlled spatiotemporal excitation of metal nanoparticles with picosecond optical pulses. *Physical Review B - Condensed Matter and Materials Physics*, 71(3):1–9, 2005.

[141] Lina Cao, Rene A. Nome, Jason M. Montgomery, Stephen K. Gray, and Norbert F. Scherer. Controlling plasmonic wave packets in silver nanowires. *Nano Letters*, 10(9):3389–3394, 2010.

[142] J. S. Huang, D. V. Voronine, P. Tuchscherer, T. Brixner, and B. Hecht. Deterministic spatiotemporal control of optical fields in nanoantennas and plasmonic circuits. *Physical Review B - Condensed Matter and Materials Physics*, 79(19):1–5, 2009.

[143] Hrvoje Petek, Vahit Sametoglu, Niko Pontius, and Atsushi Kubo. Imaging of surface plasmon dynamics in nanostructured silver films. *IQEC, International Quantum Electronics Conference Proceedings*, 2005:112, 2005.

[144] J. Lehmann, M. Merschdorf, W. Pfeiffer, A. Thon, S. Voll, and G. Gerber. Surface plasmon dynamics in silver nanoparticles studied by femtosecond time-resolved photoemission. *Physical Review Letters*, 85(14):2921–2924, oct 2000.

[145] Erik Mårsell, Arthur Losquin, Robin Svärd, Miguel Miranda, Chen Guo, Anne Harth, Eleonora Lorek, Johan Mauritsson, Cord L. Arnold, Hongxing Xu, Anne L'Huillier, and Anders

Mikkelsen. Nanoscale Imaging of Local Few-Femtosecond Near-Field Dynamics within a Single Plasmonic Nanoantenna. *Nano Letters*, 15(10):6601–6608, oct 2015.

[146] Quan Sun, Han Yu, Kosei Ueno, Atsushi Kubo, Yasutaka Matsuo, and Hiroaki Misawa. Dissecting the Few-Femtosecond Dephasing Time of Dipole and Quadrupole Modes in Gold Nanoparticles Using Polarized Photoemission Electron Microscopy. *ACS Nano*, 10(3):3835–3842, 2016.

[147] Franziska Zeuner, Mulda Muldarisnur, Andre Hildebrandt, Jens Förstner, and Thomas Zentgraf. Coupling Mediated Coherent Control of Localized Surface Plasmon Polaritons. *Nano Letters*, 15(6):4189–4193, 2015.

[148] Jue Min Yi, Dongchao Hou, Heiko Kollmann, Vladimir Smirnov, Zsuzsanna Pápa, Péter Dombi, Martin Silies, and Christoph Lienau. Probing Coherent Surface Plasmon Polariton Propagation Using Ultrabroadband Spectral Interferometry. *ACS Photonics*, 4(2):347–354, feb 2017.

[149] Keisuke Imaeda and Kohei Imura. Optical control of plasmonic fields by phase-modulated pulse excitations. *Optics Express*, 21(22):27481, 2013.

[150] Kohei Imura, Tetsuhiko Nagahara, and Hiromi Okamoto. Near-field two-photon-induced photoluminescence from single gold nanorods and imaging of plasmon modes. *Journal of Physical Chemistry B*, 109(27):13214–13220, 2005.

[151] Nicolò Accanto, Lukasz Piatkowski, Jan Renger, and Niek F van Hulst. Capturing the optical phase response of nanoantennas by coherent second-harmonic microscopy. *Nano letters*, 14(7):4078–4082, 2014.

[152] P. Biagioni, M. Celebrano, M. Savoini, G. Grancini, D. Brida, S. Mátéfi-Tempfli, M. Mátéfi-Tempfli, L. Duò, B. Hecht, G. Cerullo, and M. Finazzi. Dependence of the two-photon photoluminescence yield of gold nanostructures on the laser pulse duration. *Physical Review B - Condensed Matter and Materials Physics*, 80(4):1–5, 2009.

[153] Paolo Biagioni, Daniele Brida, Jer Shing Huang, Johannes Kern, Lamberto Duò, Bert Hecht, Marco Finazzi, and Giulio Cerullo. Dynamics of four-photon photoluminescence in gold nanoantennas. *Nano Letters*, 12(6):2941–2947, 2012.

[154] Vadim V. Lozovoy, Igor Pastirk, Katherine A. Walowicz, and Marcos Dantus. Multiphoton intrapulse interference. II. Control of two- and three-photon laser induced fluorescence with shaped pulses. *Journal of Chemical Physics*, 118(7):3187–3196, 2003.

[155] Arseniy I Kuznetsov, Andrey E Miroshnichenko, Mark L Brongersma, Yuri S Kivshar, and Boris Luk'yanchuk. Optically resonant dielectric nanostructures. *Science*, 354(6314):aag2472, 2016.

[156] Alexander E Krasnok, Andrey E Miroshnichenko, Pavel A Belov, and Yuri S Kivshar. All-dielectric optical nanoantennas. *Optics Express*, 20(18):20599–20604, 2012.

[157] Manuel Decker and Isabelle Staude. Resonant dielectric nanostructures: a low-loss platform for functional nanophotonics. *Journal of Optics*, 18(10):103001, 2016.

[158] Isabelle Staude, Andrey E Miroshnichenko, Manuel Decker, Nche T Fofang, Sheng Liu, Edward Gonzales, Jason Dominguez, Ting Shan Luk, Dragomir N Neshev, Igal Brener, et al. Tailoring directional scattering through magnetic and

electric resonances in subwavelength silicon nanodisks. *ACS nano*, 7(9):7824–7832, 2013.

[159] Luca Carletti, Giuseppe Marino, Lavinia Ghirardini, Valerio F. Gili, Davide Rocco, Ivan Favero, Andrea Locatelli, Anatoly V. Zayats, Michele Celebrano, Marco Finazzi, Giuseppe Leo, Costantino De Angelis, and Dragomir N. Neshev. Nonlinear goniometry by second-harmonic generation in algaas nanoantennas. *ACS Photonics*, 5(11):4386–4392, 2018.

[160] Raju Regmi, Johann Berthelot, Pamina M Winkler, Mathieu Mivelle, Julien Proust, Frédéric Bedu, Igor Ozerov, Thomas Begou, Julien Lumeau, Hervé Rigneault, et al. All-dielectric silicon nanogap antennas to enhance the fluorescence of single molecules. *Nano letters*, 16(8):5143–5151, 2016.

[161] VF Gili, L Carletti, A Locatelli, D Rocco, Marco Finazzi, Lavinia Ghirardini, I Favero, C Gomez, A Lemaître, Michele Celebrano, et al. Monolithic algaas second-harmonic nanoantennas. *Optics express*, 24(14):15965–15971, 2016.

[162] Arseniy I Kuznetsov, Andrey E Miroshnichenko, Yuan Hsing Fu, JingBo Zhang, and Boris Luk'Yanchuk. Magnetic light. *Scientific reports*, 2:492, 2012.

[163] Maxim R Shcherbakov, Dragomir N Neshev, Ben Hopkins, Alexander S Shorokhov, Isabelle Staude, Elizaveta V Melik-Gaykazyan, Manuel Decker, Alexander A Ezhov, Andrey E Miroshnichenko, Igal Brener, et al. Enhanced third-harmonic generation in silicon nanoparticles driven by magnetic response. *Nano letters*, 14(11):6488–6492, 2014.

[164] Maxim R Shcherbakov, Polina P Vabishchevich, Alexander S Shorokhov, Katie E Chong, Duk-Yong Choi, Isabelle Staude, Andrey E Miroshnichenko, Dragomir N Neshev, Andrey A

Fedyanin, and Yuri S Kivshar. Ultrafast all-optical switching with magnetic resonances in nonlinear dielectric nanostructures. *Nano Letters*, 15(10):6985–6990, 2015.

[165] L Carletti, A Locatelli, O Stepanenko, G Leo, and C De Angelis. Enhanced second-harmonic generation from magnetic resonance in algaas nanoantennas. *Optics express*, 23(20):26544–26550, 2015.

[166] Daria A Smirnova, Alexander B Khanikaev, Lev A Smirnov, and Yuri S Kivshar. Multipolar third-harmonic generation driven by optically induced magnetic resonances. *ACS Photonics*, 3(8):1468–1476, 2016.

[167] Zhongyi Guo, Zixiang Li, and Kai Guo. The enhanced second-harmonic generation based on magnetic-lorentz-force effect. *Annalen der Physik*, 531(4):1800470, 2019.

[168] Elizaveta Vladimirovna Melik-Gaykazyan, Kirill Leonidovich Koshelev, J-H Choi, Sergey S Kruk, H-G Park, Andrey A Fedyanin, and Yurii Semenovich Kivshar. Enhanced second-harmonic generation with structured light in algaas nanoparticles governed by magnetic response. *JETP Letters*, pages 1–5, 2019.

[169] Gustavo Grinblat, Yi Li, Michael P Nielsen, Rupert F Oulton, and Stefan A Maier. Enhanced third harmonic generation in single germanium nanodisks excited at the anapole mode. *Nano letters*, 16(7):4635–4640, 2016.

[170] Javier Cambiasso, Gustavo Grinblat, Yi Li, Aliaksandra Rakovich, Emiliano Cortés, and Stefan A Maier. Bridging the gap between dielectric nanophotonics and the visible regime with effectively lossless gallium phosphide antennas. *Nano letters*, 17(2):1219–1225, 2017.

[171] Sheng Liu, Polina P Vabishchevich, Aleksandr Vaskin, John L Reno, Gordon A Keeler, Michael B Sinclair, Isabelle Staude, and Igal Brener. An all-dielectric metasurface as a broadband optical frequency mixer. *Nature communications*, 9(1):2507, 2018.

[172] Amr M Shaltout, Vladimir M Shalaev, and Mark L Brongersma. Spatiotemporal light control with active metasurfaces. *Science*, 364(6441):eaat3100, 2019.

[173] Chengjun Zou, Jürgen Sautter, Frank Setzpfandt, and Isabelle Staude. Resonant dielectric metasurfaces: active tuning and nonlinear effects. *Journal of Physics D: Applied Physics*, 52(37):373002, 2019.

[174] Baoshan Guo, Lan Jiang, Yanhong Hua, Ningwei Zhan, Jingang Jia, Kunpeng Chu, and YongFeng Lu. Beam manipulation mechanisms of dielectric metasurfaces. *ACS Omega*, 4(4):7467–7473, 2019.

[175] Dalziel J Wilson, Katharina Schneider, Simon Hoenl, Miles Anderson, Tobias J Kippenberg, and Paul Seidler. Gallium phosphide nonlinear photonics. *arXiv preprint arXiv:1808.03554*, 2018.

[176] Amrit De and Craig E Pryor. Predicted band structures of iii-v semiconductors in the wurtzite phase. *Physical Review B*, 81(15):155210, 2010.

[177] David E Aspnes and AA Studna. Dielectric functions and optical parameters of si, ge, gap, gaas, gasb, inp, inas, and insb from 1.5 to 6.0 ev. *Physical review B*, 27(2):985, 1983.

[178] Warren O Groves and Arnold S Epstein. Gallium phosphide light-emitting diodes, January 6 1976. US Patent 3,931,631.

[179] Arpad A Bergh and Paul Jeremy Dean. Light-emitting diodes. *Oxford, Clarendon Press, 1976. 598 p*, 1976.

[180] Edward D Palik. *Handbook of optical constants of solids*, volume 3. Academic press, 1998.

[181] Maxim R Shcherbakov, Alexander S Shorokhov, Dragomir N Neshev, Ben Hopkins, Isabelle Staude, Elizaveta V Melik-Gaykazyan, Alexander A Ezhov, Andrey E Miroshnichenko, Igal Brener, Andrey A Fedyanin, et al. Nonlinear interference and tailorable third-harmonic generation from dielectric oligomers. *Acs Photonics*, 2(5):578–582, 2015.

[182] Yuanmu Yang, Wenyi Wang, Abdelaziz Boulesbaa, Ivan I Kravchenko, Dayrl P Briggs, Alexander Puretzky, David Geohegan, and Jason Valentine. Nonlinear fano-resonant dielectric metasurfaces. *Nano letters*, 15(11):7388–7393, 2015.

[183] Alexander S Shorokhov, Elizaveta V Melik-Gaykazyan, Daria A Smirnova, Ben Hopkins, Katie E Chong, Duk-Yong Choi, Maxim R Shcherbakov, Andrey E Miroshnichenko, Dragomir N Neshev, Andrey A Fedyanin, et al. Multifold enhancement of third-harmonic generation in dielectric nanoparticles driven by magnetic fano resonances. *Nano letters*, 16(8):4857–4861, 2016.

[184] Polina P Vabishchevich, Sheng Liu, Michael B Sinclair, Gordon A Keeler, Gregory M Peake, and Igal Brener. Enhanced second-harmonic generation using broken symmetry iii–v semiconductor fano metasurfaces. *ACS Photonics*, 5(5):1685–1690, 2018.

[185] Lei Xu, Mohsen Rahmani, Khosro Zangeneh Kamali, Aristeidis Lamprianidis, Lavinia Ghirardini, Jürgen Sautter, Rocio Camacho-Morales, Haitao Chen, Matthew Parry, Isabelle

Staude, et al. Boosting third-harmonic generation by a mirror-enhanced anapole resonator. *Light, science & applications*, 7, 2018.

[186] Maria Timofeeva, Lukas Lang, Flavia Timpu, Claude Renaut, Alexei Bouravleuv, Igor Shtrom, George Cirlin, and Rachel Grange. Anapoles in free-standing iii–v nanodisks enhancing second-harmonic generation. *Nano letters*, 18(6):3695–3702, 2018.

[187] Sheng Liu, Michael B Sinclair, Sina Saravi, Gordon A Keeler, Yuanmu Yang, John Reno, Gregory M Peake, Frank Setzpfandt, Isabelle Staude, Thomas Pertsch, et al. Resonantly enhanced second-harmonic generation using iii–v semiconductor all-dielectric metasurfaces. *Nano letters*, 16(9):5426–5432, 2016.

[188] Peter R Wiecha, Arnaud Arbouet, Christian Girard, Thierry Baron, and Vincent Paillard. Origin of second-harmonic generation from individual silicon nanowires. *Physical Review B*, 93(12):125421, 2016.

[189] Sergey V Makarov, Mihail I Petrov, Urs Zywietz, Valentin Milichko, Dmitry Zuev, Natalia Lopanitsyna, Alexey Kuksin, Ivan Mukhin, George Zograf, Evgeniy Ubyivovk, et al. Efficient second-harmonic generation in nanocrystalline silicon nanoparticles. *Nano letters*, 17(5):3047–3053, 2017.

[190] C Huang, Alexandre Bouhelier, G Colas des Francs, Aurélien Bruyant, A Guenot, Eric Finot, J-C Weeber, and Alain Dereux. Gain, detuning, and radiation patterns of nanoparticle optical antennas. *Physical Review B*, 78(15):155407, 2008.

[191] M Andreas Lieb, James M Zavislan, and Lukas Novotny. Single-molecule orientations determined by direct emission pattern imaging. *JOSA B*, 21(6):1210–1215, 2004.

[192] TH Taminiau, FD Stefani, Franciscus B Segerink, and NF Van Hulst. Optical antennas direct single-molecule emission. *Nature Photonics*, 2(4):234, 2008.

[193] Ion M Hancu, Alberto G Curto, Marta Castro-López, Martin Kuttge, and Niek F van Hulst. Multipolar interference for directed light emission. *Nano letters*, 14(1):166–171, 2013.

[194] Luca Carletti, Andrea Locatelli, Dragomir Neshev, and Costantino De Angelis. Shaping the radiation pattern of second-harmonic generation from algaas dielectric nanoantennas. *ACS Photonics*, 3(8):1500–1507, 2016.

[195] Reza Sanatinia, Srinivasan Anand, and Marcin Swillo. Experimental quantification of surface optical nonlinearity in gap nanopillar waveguides. *Optics express*, 23(2):756–764, 2015.

[196] Luca Carletti, Giuseppe Marino, Lavinia Ghirardini, Valerio F Gili, Davide Rocco, Ivan Favero, Andrea Locatelli, Anatoly V Zayats, Michele Celebrano, Marco Finazzi, et al. Nonlinear goniometry by second-harmonic generation in algaas nanoantennas. *ACS Photonics*, 5(11):4386–4392, 2018.

[197] W Lukosz and RE Kunz. Light emission by magnetic and electric dipoles close to a plane dielectric interface. ii. radiation patterns of perpendicular oriented dipoles. *JOSA*, 67(12):1615–1619, 1977.

[198] Sergey S Kruk, Rocio Camacho-Morales, Lei Xu, Mohsen Rahmani, Daria A Smirnova, Lei Wang, Hark Hoe Tan, Chennupati Jagadish, Dragomir N Neshev, and Yuri S Kivshar. Nonlinear optical magnetism revealed by second-harmonic generation in nanoantennas. *Nano letters*, 17(6):3914–3918, 2017.

[199] Andrey B Evlyukhin, Sergey M Novikov, Urs Zywietz, Rene Lynge Eriksen, Carsten Reinhardt, Sergey I Bozhevolnyi, and Boris N Chichkov. Demonstration of magnetic dipole

resonances of dielectric nanospheres in the visible region. *Nano letters*, 12(7):3749–3755, 2012.

[200] Lei Shi, Justin T Harris, Roberto Fenollosa, Isabelle Rodriguez, Xiaotang Lu, Brian A Korgel, and Francisco Meseguer. Monodisperse silicon nanocavities and photonic crystals with magnetic response in the optical region. *Nature communications*, 4:1904, 2013.

[201] Paweł Woźniak, Peter Banzer, and Gerd Leuchs. Selective switching of individual multipole resonances in single dielectric nanoparticles. *Laser & Photonics Reviews*, 9(2):231–240, 2015.

[202] A De Martino, S Ben Hatit, and M Foldyna. Mueller polarimetry in the back focal plane. In *Metrology, Inspection, and Process Control for Microlithography XXI*, volume 6518, page 65180X. International Society for Optics and Photonics, 2007.

[203] Clara I Osorio, Abbas Mohtashami, and A Femius Koenderink. K-space polarimetry of bullseye plasmon antennas. *Scientific reports*, 5:9966, 2015.

[204] Abbas Mohtashami, Clara I Osorio, and A Femius Koenderink. Angle-resolved polarimetry of antenna-mediated fluorescence. *Physical Review Applied*, 4(5):054014, 2015.

[205] Anders Pors, Michael G Nielsen, and Sergey I Bozhevolnyi. Plasmonic metagratings for simultaneous determination of stokes parameters. *Optica*, 2(8):716–723, 2015.

[206] Ruslan Röhrich, Chris Hoekmeijer, Clara I Osorio, and A Femius Koenderink. Quantifying single plasmonic nanostructure far-fields with interferometric and polarimetric k-space microscopy. *Light: Science & Applications*, 7(1):65, 2018.

[207] Rocio Camacho-Morales, Mohsen Rahmani, Sergey Kruk, Lei Wang, Lei Xu, Daria A Smirnova, Alexander S Solntsev, Andrey Miroshnichenko, Hark Hoe Tan, Fouad Karouta, et al. Nonlinear generation of vector beams from algaas nanoantennas. *Nano letters*, 16(11):7191–7197, 2016.

[208] Juergen Sautter, Lei Xu, Andrey E Miroshnichenko, Mykhaylo Lysevych, Irina Volkovskaya, Daria A Smirnova, Rocio Camacho-Morales, Khosro Zangeneh Kamali, Fouad Karouta, Kaushal Vora, et al. Tailoring second-harmonic emission from (111)-gaas nanoantennas. *Nano letters*, 2019.

[209] Junxiong Wei, S Chaitanya Kumar, Hanyu Ye, Kavita Devi, Peter G Schunemann, and M Ebrahim-Zadeh. Nanosecond difference-frequency generation in orientation-patterned gallium phosphide. *Optics letters*, 42(11):2193–2196, 2017.

[210] Andrey B Evlyukhin, Tim Fischer, Carsten Reinhardt, and Boris N Chichkov. Optical theorem and multipole scattering of light by arbitrarily shaped nanoparticles. *Physical Review B*, 94(20):205434, 2016.

[211] Patrick Grahn, Andriy Shevchenko, and Matti Kaivola. Electromagnetic multipole theory for optical nanomaterials. *New Journal of Physics*, 14(9):093033, 2012.

[212] Tetsuya Inoue and Hirokazu Hori. Theoretical treatment of electric and magnetic multipole radiation near a planar dielectric surface based on angular spectrum representation of vector field. *Optical review*, 5(5):295–302, 1998.

[213] Viktor Myroshnychenko, Jessica Rodríguez-Fernández, Isabel Pastoriza-Santos, Alison M Funston, Carolina Novo, Paul Mulvaney, Luis M Liz-Marzán, and F Javier García de Abajo. Modelling the optical response of gold nanoparticles. *Chemical Society Reviews*, 37(9):1792–1805, 2008.

[214] Alexander E Krasnok, Constantin R Simovski, Pavel A Belov, and Yuri S Kivshar. Superdirective dielectric nanoantennas. *Nanoscale*, 6(13):7354–7361, 2014.

[215] Yuan Hsing Fu, Arseniy I Kuznetsov, Andrey E Miroshnichenko, Ye Feng Yu, and Boris Luk'yanchuk. Directional visible light scattering by silicon nanoparticles. *Nature communications*, 4:1527, 2013.

[216] Timur Shegai, Peter Johansson, Christoph Langhammer, and Mikael Kall. Directional scattering and hydrogen sensing by bimetallic pd–au nanoantennas. *Nano letters*, 12(5):2464–2469, 2012.

[217] M. Kerker, D.-S. Wang, and C. L. Giles. Electromagnetic scattering by magnetic spheres. *J. Opt. Soc. Am.*, 73(6):765–767, Jun 1983.

[218] Steven Person, Manish Jain, Zachary Lapin, Juan Jose Sáenz, Gary Wicks, and Lukas Novotny. Demonstration of zero optical backscattering from single nanoparticles. *Nano letters*, 13(4):1806–1809, 2013.

[219] Ankan Bag, Martin Neugebauer, Paweł Woźniak, Gerd Leuchs, and Peter Banzer. Transverse kerker scattering for angstrom localization of nanoparticles. *Physical review letters*, 121(19):193902, 2018.

[220] Kan Yao and Yongmin Liu. Controlling electric and magnetic resonances for ultracompact nanoantennas with tunable directionality. *ACS Photonics*, 3(6):953–963, 2016.

[221] Brice Rolly, Brian Stout, and Nicolas Bonod. Boosting the directivity of optical antennas with magnetic and electric dipolar resonant particles. *Optics express*, 20(18):20376–20386, 2012.

[222] SRK Rodriguez, F Bernal Arango, TP Steinbusch, MA Verschuuren, AF Koenderink, and J Gómez Rivas. Breaking the symmetry of forward-backward light emission with localized and collective magnetoelectric resonances in arrays of pyramid-shaped aluminum nanoparticles. *Physical review letters*, 113(24):247401, 2014.

[223] Rasoul Alaee, Mohammad Albooyeh, Aso Rahimzadegan, Mohammad S Mirmoosa, Yuri S Kivshar, and Carsten Rockstuhl. All-dielectric reciprocal bianisotropic nanoparticles. *Physical Review B*, 92(24):245130, 2015.

[224] R Alaee, R Filter, D Lehr, F Lederer, and C Rockstuhl. A generalized kerker condition for highly directive nanoantennas. *Optics letters*, 40(11):2645–2648, 2015.

[225] Sylvain D Gennaro, Mohsen Rahmani, Vincenzo Giannini, Heykel Aouani, Themistoklis PH Sidiropoulos, Miguel Navarro-Cía, Stefan A Maier, and Rupert F Oulton. The interplay of symmetry and scattering phase in second harmonic generation from gold nanoantennas. *Nano letters*, 16(8):5278–5285, 2016.

[226] Jérémy Butet, TV Raziman, Kuang-Yu Yang, Gabriel D Bernasconi, and Olivier JF Martin. Controlling the nonlinear optical properties of plasmonic nanoparticles with the phase of their linear response. *Optics express*, 24(15):17138–17148, 2016.

[227] Matthew Comstock, Vadim V Lozovoy, Igor Pastirk, and Marcos Dantus. Multiphoton intrapulse interference 6; binary phase shaping. *Optics express*, 12(6):1061–1066, 2004.